

Perturbative and Non Perturbative Aspects of Lattice Quantum Chromodynamics

By

ABHISHEK CHOWDHURY

PHYS05200904007

Saha Institute of Nuclear Physics

A thesis submitted to the

Board of Studies in Physical Sciences

In partial fulfillment of requirements

For the Degree of

DOCTOR OF PHILOSOPHY

of

HOMI BHABHA NATIONAL INSTITUTE



September, 2014

Homi Bhabha National Institute

Recommendations of the Viva Voce Board

As members of the Viva Voce Board, we certify that we have read the dissertation prepared by **ABHISHEK CHOWDHURY** entitled **Perturbative and Non Perturbative Aspects of Lattice Quantum Chromodynamics** and recommend that it may be accepted as fulfilling the dissertation requirement for the Degree of Doctor of Philosophy.

Munshi

28/11/2014

Chairman - Prof. Munshi Golam Mustafa, SINP, Kolkata

Date

Avaroth Harindranath

28/11/2014

Guide/Convener - Prof. Avaroth Harindranath, SINP, Kolkata

Date

Amit Ghosh

28/11/2014

Member 1 - Prof. Amit Ghosh, SINP, Kolkata

Date

Prakash Mathews

28/11/14

Member 2 - Prof. Prakash Mathews, SINP, Kolkata

Date

External Examiner - Prof. Dipankar Chakrabarti, IIT, Kanpur

Dipankar Chakrabarti

Date 28/11/2014

Final approval and acceptance of this dissertation is contingent upon the candidate's submission of the final copies of the dissertation to HBNI.

I hereby certify that I have read this dissertation prepared under my direction and recommend that it may be accepted as fulfilling the dissertation requirement.

Date: 28/11/2014

Place: Kolkata

Avaroth Harindranath

Guide

STATEMENT BY AUTHOR

This dissertation has been submitted in partial fulfillment of requirements for an advanced degree at Homi Bhabha National Institute (HBNI) and is deposited in the Library to be made available to borrowers under rules of the HBNI.

Brief quotations from this dissertation are allowable without special permission, provided that accurate acknowledgement of source is made. Requests for permission for extended quotation from or reproduction of this manuscript in whole or in part may be granted by the Competent Authority of HBNI when in his or her judgement the proposed use of the material is in the interests of scholarship. In all other instances, however, permission must be obtained from the author.



Abhishek Chowdhury

DECLARATION

I, hereby declare that the investigation presented in the thesis has been carried out by me. The work is original and has not been submitted earlier as a whole or in part for a degree/diploma at this or any other Institution/University.

Abhishek Chowdhury

Abhishek Chowdhury

DEDICATIONS

Dedicated to my mother.

ACKNOWLEDGEMENTS

Looking back through my journey at Saha Institute, I am indebted to a great many people for teaching, guidance, help and encouragement throughout in carrying out the work presented in this dissertation and as well as in the preparation of this document. This work could not have been completed without their support.

First and foremost among them is my advisor Prof. A. Harindranath with his vast wisdom and knowledge, his cheerful demeanor, his willingness to be accessible at all times, and his penchant for being tough when required all make him as close to a perfect advisor as there can be. I have learned something from each and every conversation with him, be it about mathematics, physics, politics, literature or even most interesting spirituality - I wish to thank Harindranath for the treasure trove of memorable moments.

During my thesis, I had the chance to collaborate with a number of people. First of all, I am also thankful to Prof. Asit Kumar De and Prof. Pushan Majumder for their active collaboration with me and for their valuable suggestions in different time of my research works.

I have to mention a name Santanuda (Dr. Santanu Mondal) who not only collaborated with me but also spent a valuable moment in my life. I still remember all those days, where I had several valuable discussions with him that often forced me to think more carefully about physics part of the problems. I have to admit that those discussions helped me to understand the subject of LQCD in a better way.

I would like to thank to one of my active collaborators, Jyotirmoyda (Prof. Jyotirmoy Maiti) for his constant support and guidance. The thing I admire most in Jyotirmoyda is his attention to detail and I learned from him that the style of writing numerical codes, is as important as understanding the theory part of the codes itself. If I ever get any compliments about my technical code writing skills, then it should go to Jyotirmoyda. Jyotirmoyda is one of the nicest people I ever met and he has helped me with my personal problems as my elder brother. Again, I have to admit that without his mentoring, I would not have finished this thesis.

In the thesis, all the numerical calculations are carried out on the Cray XT5 and Cray XE6 systems supported by the 11th-12th Five Year Plan Projects of the Theory Division, SINP under the DAE, Govt. of India. For the prompt maintenance of the systems and the help in data management, I want to thank Mr. Richard Chang.

On a personal level, I would like to thank my family and my parents for their love and for their encouragement. They had a strong belief and confidence in me, for that, I shall forever be grateful to them. Most importantly, I was so fortunate to enjoy the social environment, support and love from my family in all these years. I am deeply indebted to them. During my stay at Saha Institute I had the opportunity of sharing my way with many a people whose company made the life most enjoyable. Special thanks to Prof. Munshi Golam Mustafa (he has helped me quite a lot in many situations), Susnatadi (Susnata Seth) and Susmitadi (Susmita Kundu), and Santanuda (Santanu Mondal). I would like to thank all my contemporary boarders of Meghnad Saha Hostel for providing me a memorable phase of life. It is a mammoth task to individually mention the names of my numerous friends (especially Ujjal Gayen, Subir Biswas and Mahatsab Mondal) whose friendship I cherish. I will also never forget the hospitality I enjoyed here in the hostel. My hearty thanks to all the hostel staffs such as Sureshda, Saktida and Somnathda.

Last, but definitely not the least, I want to convey my sincere thanks to all the members of theory division with special mention to Avirup Ghosh, Atanu Kumar, Satyajit Seth, Najmul Haque and also teaching section, library section, computer section and post M.Sc. friends for their kind help and cooperation.

Contents

Contents	vii
Synopsis	xi
List of Publications	xviii
List of Figures	xxi
1 Introduction	1
2 Quantum Chromodynamics on the lattice	9
2.1 The fields: quark and gluon	9
2.2 The QCD action in the continuum	10
2.3 Path integral quantization	11
2.4 Lattice regularization	12
2.5 The Wilson gauge action	13
2.6 Naive fermions and the doubling problem	14
2.7 Removing doublers	15
2.8 Wilson fermion and gauge actions	16
3 Wilson fermions: a perturbative analysis	17
3.1 Introduction	17
3.2 Different branches of Wilson fermions	18
3.3 Making a particular branch physical one	19

3.4	Enhanced symmetry	20
3.5	Additive renormalization in fermion self energy	21
3.6	Chiral anomaly	26
3.7	Discussion and conclusions	28
4	Topological charge density correlator with Wilson fermions	32
4.1	Introduction	32
4.2	Topological charge density correlator $C(r)$	34
4.3	Negativity of $C(r)$ due to reflection positivity	34
4.4	Divergences in $C(r)$	35
4.5	Simulation Details	37
4.6	Results	39
4.6.1	Effect of smearing	39
4.6.2	Volume dependence	40
4.6.3	Dependence on quark mass	41
4.6.4	Non-integrability of divergences and lattice spacing dependence	43
4.7	Discussion and conclusions	47
5	Autocorrelations study with Wilson fermions	49
5.1	Introduction	49
5.2	Background	50
5.3	Detail about autocorrelations and error analysis	51
5.4	Observables	53
5.5	Measurements detail	54
5.6	Results	56
5.6.1	Scaling properties with the gaps	56
5.6.2	Autocorrelations for topological susceptibility (Q_{20}^2)	57
5.6.3	Autocorrelations for $C_3(r)$, Q_3 and Q_3^2	59
5.6.4	Quark mass dependence	61
5.6.5	Effect of size and smearing	61

5.6.6	Autocorrelations for pion and nucleon propagators	62
5.7	Improved estimation of τ_{int}	63
5.8	Conclusion	65
6	Wilson flow	66
6.1	Gradient flow and smoothing operation	67
6.2	Wilson flow in continuum QCD	69
6.3	Wilson flow on lattice	70
6.4	Concluding remarks	72
7	Topological susceptibility in lattice Yang-Mills theory with open boundary condition	73
7.1	Open boundary conditions	74
7.2	Simulation details	75
7.3	Numerical results	76
7.3.1	Trajectory history of the topological charge	76
7.3.2	Distribution of Q	78
7.3.3	Distribution of $Q(x_0)$	79
7.3.4	Subvolume susceptibility	80
7.3.5	Stability of the topological susceptibility	81
7.3.6	Extraction of the topological susceptibility and its lattice spacings dependence	82
7.4	Conclusions	83
8	The scalar glueball mass	84
8.1	Introduction	84
8.2	Calculation of the lowest scalar glueball mass	85
8.3	Simulation details	86
8.4	Numerical results	87
8.4.1	Effects of boundary conditions on $\langle \bar{E}(x_0) \rangle$	87
8.4.2	Behaviour of $\langle \bar{E}(x_0) \rangle$	88

8.4.3	Choice of operators	88
8.4.4	Glueball effective mass using periodic boundary condition with Wilson flow	90
8.4.5	Glueball effective mass using periodic boundary condition with HYP smearing	91
8.4.6	Comparison of the lowest glueball mass using open and periodic boundary conditions	92
8.4.7	Extraction of the lowest glueball mass and its lattice spacings dependence	93
8.5	Conclusions and discussions	94
9	Summary	96
	Bibliography	99

Synopsis

The journey of lattice quantum chromodynamics (LQCD) was started by K.G. Wilson through his fundamental papers [1, 2] in order to explore the non-perturbative structure of Quantum field theories. In lattice, space-time is discretized through a lattice spacing a which acts as a regulator. To extract the physics for a particular theory, one has to take $a \rightarrow 0$ limit which is known as the continuum limit of the theory. We get a naive lattice action of QCD introducing lattice structure on continuum QCD action. A theory without regulator, usually, is ill-defined. Lattice is a such kind of regulator which can maintain both chiral and gauge symmetry except Lorentz symmetry. One can restore Lorentz symmetry by taking the continuum limit of the theory.

The naive lattice action of QCD has a problem called fermion doubling. Naive discretization of the Dirac action on lattice leads to 16 solutions (called doublers) which are unphysical in nature. In continuum, we always get only one solution. To remove 15 unwanted doublers, Wilson added a dimension five term (Wilson term) to the naive lattice QCD action but this Wilson term breaks chiral symmetry. Because of the explicit violation of chiral symmetry by a dimension five operator (Wilson term), Wilson formulation of lattice QCD [1] has been known to be difficult to simulate at light quark masses. Lack of chiral symmetry means that the physical quark mass is no longer proportional to the bare quark mass (the quark mass renormalization is no longer only multiplicative) and Wilson Dirac operator is not protected from arbitrarily small eigenvalues and may lead to zero or near zero modes for individual configurations. This is the infamous problem of exceptional

configurations. This leads to convergence difficulties for fermion matrix inversion. This poses difficulties for lattice simulations with Wilson fermions in the chiral region. In the past, simulations with unimproved Wilson action has shown large scaling violations in the observables [3, 4]. However, one should keep in mind that most of these were quenched simulations done at large pion masses, not small enough lattice spacings and smaller volumes. Further, the demonstration of the suppression of topological susceptibility with decreasing quark mass was inconclusive [5]. The chiral behaviour of pion mass and decay constant with respect to quark mass (specifically, the presence of chiral logarithms) as dictated by chiral perturbation theory was also not convincingly demonstrable in the past with unimproved Wilson fermions [6]. These issues raise the question whether dynamical simulations with unimproved Wilson fermions with small enough quark masses produce the continuum answers.

For the past few years, the chiral properties (chiral anomaly and chiral condensate) of unimproved Wilson lattice QCD have been studied [7, 8]. Another important quantity is the chiral behaviour of topological susceptibility. Earlier attempt [5] with naive Wilson fermions and HMC algorithm to verify the suppression of topological susceptibility with decreasing quark mass, expected from chiral Ward identity and chiral perturbation theory, was unable to unambiguously confirm the suppression.

To understand this issue, we have generated configurations by means of Domain Decomposed Hybrid Monte Carlo (DDHMC) algorithm at two different lattice spacings ($\beta = 5.6$ and $\beta = 5.8$) using two degenerate flavours of unimproved Wilson fermions and unimproved Wilson gauge actions. In our work [9], we have addressed this issue and unambiguously demonstrated the suppression of the topological susceptibility with decreasing quark mass, expected from chiral Ward identity and chiral perturbation theory. The effects of quark mass, lattice volume and the lattice spacing on the spanning of different topological sectors are presented in this work.

Next, we consider the reflection positivity feature of the naive Wilson fermions action

in Euclidean space because it assures the hermiticity property of the Hamiltonian in the Minkowski space. In papers [10, 11], authors have pointed out that the topological charge density correlator (TCDC) in lattice QCD is an important observable which should be negative to show the reflection positivity feature of the lattice action. Not only reflection positivity issue, one can understand the mechanism of decreasing susceptibility with quark mass through TCDC in lattice. It is interesting to investigate on the lattice the properties of TCDC inferred from the continuum theory. However the signal of TCDC on lattice is noisy and one has to resort to some smearing procedure like Wilson flow (see for examples [12–14]) which allows to study TCDC measured at different lattice spacings at a given energy scale. TCDC changes with energy scale and at infinitely large energy scale one hopes to recover continuum properties.

In our paper [15], we have shown that (1) the TCDC is negative beyond a positive core and radius of the core shrinks as lattice spacing decreases, (2) as the volume decreases, the magnitude of the contact term and the radius of the positive core decrease and the magnitude of the negative peak increases resulting in the suppression of the topological susceptibility as the volume decreases [16, 17], (3) the contact term and radius of the positive core decrease with decreasing quark mass at a given lattice spacing and the negative peak increases with decreasing quark mass resulting in the suppression of the topological susceptibility with decreasing quark mass, (4) increasing levels of smearing suppresses the contact term and the negative peak keeping the susceptibility intact and (5) both the contact term and the negative peak diverge in nonintegrable fashion as lattice spacing decreases.

When we generate configurations in LQCD through Markov chain Monte Carlo algorithm, the generated configurations are not independent of each other and they are correlated with each other. The autocorrelation of an observable is an important estimation to understand how many configurations are correlated with each other. We have to study autocorrelation because the error analysis of LQCD data has to deal with the presence of

autocorrelations.

Apart from [18], there is no systematic study about auto-correlation done so far. In our work [19], we have studied autocorrelation for several observables in two-flavour Wilson lattice QCD using DD-HMC algorithm. We have shown that (1) at a given lattice spacing, autocorrelations of topological susceptibility, unsmeared plaquette and pion and nucleon propagators with wall source show an indication of decrease with decreasing quark mass, (2) autocorrelation of topological susceptibility and autocorrelation of topological charge density correlator increase with decreasing lattice spacing but the effect is milder in the latter case and (3) increasing the size and the smear level increase the autocorrelation of the smeared Wilson loop.

In addition to the demonstration of the suppression of topological susceptibility with decreasing quark mass, in the paper [8], we have calculated pion mass, pion decay constant, PCAC quark mass and nucleon mass in two flavour lattice QCD with unimproved Wilson fermion and gauge actions. Simulations are performed using DD-HMC algorithm at two lattice spacings and two volumes for several values of the quark mass. The cutoff effects in pion mass (figure 6 (left) in Ref. [8]) and nucleon mass (figure 6 (right) in Ref. [8]) for the explored region of parameter space are found to be negligible. We extract the average value of the up-down quark mass in the \overline{MS} scheme at 2 GeV, which is in good agreement with the world data [20]. The chiral behaviours of pion mass, pion decay constant and quark condensate are found to be qualitatively consistent with NLO chiral perturbation theory. The extracted values of the pion decay constant and the chiral condensate are in reasonable agreement with the world data [20].

As we have already mentioned, naive discretization of the Dirac action leads to 16 solutions (called doublers) in the four dimensional theory. The sixteen doublers are classified into five branches. Almost all of the studies so far, both analytical and numerical, have focused on the so-called first (physical) branch. However, very recently, occurrence of an enhanced symmetry has been discovered in the central branch [21–23] when the on-site

terms (mass term and that from the Wilson term) are absent in the action. The enhanced symmetry prohibits additive renormalization through radiative corrections. Since in this case, the central branch yields six massless fermions, as suggested in the paper [22], an alternative way to simulate twelve flavour non-abelian gauge theories emerges. Such theories are of interest in the context of beyond standard model physics (for recent review see [24]).

In our work [25], we have explored different branches of the fermion doublers with Wilson fermion in perturbation theory, in the context of additive mass renormalization and chiral anomaly. We have shown that by appropriately averaging over suitably chosen branches one can reduce cut-off artifacts. The idea of reducing the cut-off artifacts by averaging over positive and negative r (Wilson parameter) for the physical branch has been discussed before in the literature [26–28]. We have however considered the cut-off effects for all the branches [25]. Comparing the central branch with all other branches, we have found that the central branch, among all the avatars of the Wilson fermion, is the most suitable candidate for exploring near conformal lattice field theories.

An open problem in numerical simulation of lattice QCD is that sampling gauge configurations over different topological sectors becomes more and more difficult as the continuum limit is approached. Autocorrelation times of physical quantities grow rapidly making the calculation of expectation values time consuming. To partially overcome this problem, using open boundary conditions (instead of the usual periodic or anti-periodic ones) in the temporal direction of the lattice has been proposed [29]. Lattice gauge theory with such boundary conditions have no barriers between different topological sectors. This has been shown by extensive simulations in SU(3) gauge theory [30]. Even though the open boundary conditions introduce boundary effects and thus complicate the physics analysis, their advantage from the point of view of ergodicity and efficiency have been addressed in simulations of 2+1 flavours of O(a) improved Wilson quarks [31].

In the context of topology of gauge fields, an interesting quantity to study is the topo-

logical susceptibility (χ) in pure Yang-Mills theory which is related to the η' mass by the famous Witten-Veneziano formula [11]. We have generated gauge configurations in SU(3) lattice gauge theory at different lattice volumes and gauge couplings using the openQCD program [32]. Gauge configurations using periodic boundary conditions also have been generated for several of the same lattice parameters (necessary changes to implement periodic boundary condition in temporal direction were made in the openQCD package for pure Yang-Mills case). To smooth the gauge field configurations, we used Wilson flow [12, 13] technique.

In the work [33], we address the question whether an open boundary condition in the temporal direction can yield the expected value of the topological susceptibility in SU(3) Yang-Mills theory. We have shown that the open boundary condition in the temporal direction can yield the expected value of the topological susceptibility in lattice SU(3) Yang-Mills theory. The results agree with numerical simulations employing the periodic boundary condition.

Apart from the topological susceptibility, one may ask whether open boundary condition can reproduce other observables calculated with periodic boundary condition. It is well known in condensed matter systems that under certain circumstances open boundary conditions sometimes give unreliable results (see for example [34]). In our another recent work [35], we continue our exploration of open boundary condition in the context of the extraction of lowest glueball mass from the temporal decay of correlators. In lattice Yang-Mills theory, we have shown that the open boundary condition on the gauge fields in the temporal direction of the lattice can reproduce the lowest scalar glueball mass extracted with periodic boundary condition at reasonably large lattice scales investigated in the range $3 \text{ GeV} \leq \frac{1}{a} \leq 5 \text{ GeV}$. With open boundary condition we are able to overcome, to a large extent, the problem of trapping and performed simulation and extract the glueball mass at even larger lattice scale $\approx 5.7 \text{ GeV}$. Compared to HYP smearing, recently proposed Wilson flow exhibits better systematics as far as the extraction of glueball mass

is concerned. The extracted glueball mass shows remarkable insensitivity to the lattice spacings in the range explored in this work $3 \text{ GeV} \leq \frac{1}{a} \leq 5.7 \text{ GeV}$.

List of Publications

(The thesis will be based on those publications marked with asterisk [*])

a. Published

- *1. Open Boundary Condition, Wilson Flow and the Scalar Glueball Mass

Abhishek Chowdhury, A. Harindranath, Jyotirmoy Maiti

JHEP 1406, 067 (2014).

- *2. Topological susceptibility in lattice Yang-Mills theory with open boundary condition

Abhishek Chowdhury, A. Harindranath, Jyotirmoy Maiti, Pushan Majumdar

JHEP 1402, 045 (2014).

- *3. Many avatars of the Wilson fermion: A perturbative analysis

Abhishek Chowdhury, A. Harindranath, Jyotirmoy Maiti, Santanu Mondal

JHEP 1302, 037 (2013).

4. Pion and nucleon in two flavour QCD with unimproved Wilson fermions

Abhishek Chowdhury, Asit K. De, Sangita De Sarkar, A. Harindranath, Jyotirmoy Maiti, Santanu Mondal, Anwesa Sarkar

Nucl.Phys. B871, 82-97 (2013).

- *5. Exploring autocorrelations in two-flavour Wilson Lattice QCD using DD-HMC algorithm

Abhishek Chowdhury, Asit K. De, Sangita De Sarkar, A. Harindranath, Jyotirmoy

Maiti, Santanu Mondal, Anwesa Sarkar

Comput.Phys.Commun. 184, 1439-1445 (2013).

- *6. Topological charge density correlator in Lattice QCD with two flavours of unimproved Wilson fermions

Abhishek Chowdhury, Asit K. De, A. Harindranath, Jyotirmoy Maiti, Santanu Mondal

JHEP 1211, 029 (2012).

7. Topological susceptibility in Lattice QCD with unimproved Wilson fermions

Abhishek Chowdhury, Asit K. De, Sangita De Sarkar, A. Harindranath, Santanu Mondal, Anwesa Sarkar, Jyotirmoy Maiti

Phys.Lett. B707, 228-232 (2012).

c. Conference Publications

8. Low lying hadron spectrum and chiral condensate with two flavours of naive Wilson fermions

Abhishek Chowdhury, Asit K. De, Sangita De Sarkar, A. Harindranath, Jyotirmoy Maiti, Santanu Mondal, Anwesa Sarkar

PoS LATTICE2012, 208 (2012)

9. Quark mass, scale and volume dependence of topological charge density correlator in Lattice QCD

Abhishek Chowdhury, Asit K. De, A. Harindranath, Jyotirmoy Maiti, Santanu Mondal

PoS LATTICE2012, 200 (2012)

10. Autocorrelation studies in two-flavour Wilson lattice QCD using DD-HMC algorithm

Abhishek Chowdhury, Asit K. De, Sangita De Sarkar, A. Harindranath, Jyotirmoy

Maiti, Santanu Mondal, Anwesa Sarkar

PoS LATTICE2012, 189 (2012)

11. Spanning of Topological sectors, charge and susceptibility with naive Wilson fermions

Abhishek Chowdhury, Asit K. De, Sangita De Sarkar, A. Harindranath, Santanu Mondal, Anwesa Sarkar, Jyotirmoy Maiti

PoS LATTICE2011, 099 (2011).

List of Figures

3.1	Tadpole diagram	21
3.2	Sunset diagram	23
3.3	The magnitude of the total additive mass shift (tadpole + sunset) plotted versus the branch number.	25
3.4	The function $I(am, r, L)$ for $r = 1.0$ and $L = 100$ as a function of am for the first and fifth branches (left) and for the second and fourth branches (right).	29
3.5	The function $I(am, r, L)$ for the central branch for $r = 1.0$ and $L = 100$ as a function of am	29
4.1	Effect of smearing on $C(r)$ at $\beta = 5.8$, $\kappa = 0.15462$ and lattice volume $32^3 \times 64$	39
4.2	Effect of smearing on the χ at $\beta = 5.8$, $\kappa = 0.15462$ and lattice volume $32^3 \times 64$ (taken from Ref. [36]).	40
4.3	Finite volume dependence of the $C(r)$ at $\beta = 5.6$, $\kappa = 0.158$ and lattice volumes $16^3 \times 32$, $24^3 \times 48$ and $32^3 \times 64$	41
4.4	The quark mass dependence of $C(r)$ with emphasis on the positive region at $\beta = 5.6$ and lattice volume $24^3 \times 48$	42

4.5	The quark mass dependence of $C(r)$ with emphasis on the crossover from positive to the negative region of $C(r)$ and the negative peak region at $\beta = 5.6$ and lattice volume $24^3 \times 48$	43
4.6	Topological susceptibility at $\beta = 5.6$ and lattice volume $24^3 \times 48$ as a function of the quark mass.	44
4.7	The function $\chi(r)$, defined in eq. (4.13) as a function of r at $\beta = 5.6$ and 5.8 at comparable pion masses.	45
4.8	Comparison of the radius of the positive core of $C(r)$ at two different lattice spacings for comparable pion mass. Lattice volume is $32^3 \times 64$. . .	47
5.1	Autocorrelation functions for the unsmeared plaquette measured with 250, 1000 and 5620 thermalized configurations respectively at $\beta = 5.6$ for the ensemble B_{5b}	56
5.2	Normalized autocorrelation functions (left) and integrated autocorrelation times (right) for unsmeared plaquette with three different gaps (4, 8, 32) between measurements for the ensemble C_5 at $\beta = 5.6$	57
5.3	Normalized autocorrelation functions (left) and integrated autocorrelation times (right) for Q_{20}^2 at $\beta = 5.8$ for the ensembles D_1 and D_5	58
5.4	Trajectory histories of Q_3 (left) and $C_3(r = r_0)$ (right) for the ensembles B_{3b} and D_1	59
5.5	Normalized autocorrelation functions for $C_3(r = r_0)$ and Q_3^2 at $\beta = 5.6$ for the ensemble B_{3b}	60
5.6	Normalized autocorrelation functions and integrated autocorrelation times for $C_3(r = r_0)$ (left) and Q_3^2 (right) at $\beta = 5.8$ for the ensemble D_1	60

5.7	Normalized autocorrelation functions (left) and integrated autocorrelation times (right) for P_0 at $\beta = 5.6$ for the ensembles B_{1b} and B_{5b}	61
5.8	Normalized autocorrelation function and effective autocorrelation time for P_0 (left) Q_{20}^2 (right) for the ensemble B_{3b} at $\beta = 5.6$	63
5.9	Integrated autocorrelation times and their upper bounds (τ_{int}^u) for Q_{20}^2 at $\beta = 5.6$ for the ensembles B_{3b}, B_{4b} (left) and at $\beta = 5.8$ for the ensembles D_1, D_5 (right).	64
7.1	Trajectory history of topological charge (Q) versus simulation time at $\beta = 6.59$ and lattice volume $48^3 \times 96$ for open boundary condition (top) and periodic boundary condition (bottom). The data shown is at Wilson flow time $t/a^2 = 2$	77
7.2	Distribution of Q versus N_{cnfg} . Top one (blue) is open boundary condition and bottom (red) is periodic boundary condition at $\beta = 6.42$ and lattice volume is $32^3 \times 64$	78
7.3	Distribution of $Q(x_0)$ versus N_{cnfg} for the ensemble O_2 where $x_0 = 0, 1, 2, 3, 4$ and 24 from top to bottom respectively at $\beta = 6.42$ and lattice volume $32^3 \times 64$	79
7.4	Subvolume susceptibility ($\bar{\chi}$) versus temporal length (Δx_0) for the ensembles O_1, O_2 and O_3	80
7.5	Behaviour of topological susceptibility for both open and periodic boundary condition under Wilson flow plotted versus the flow time for different lattice spacings and lattice volumes.	81

7.6	$\chi^{1/4}$ in dimensionful unit plotted versus a^2 for both open and periodic boundary condition for different lattice spacings and lattice volumes. For comparison, data from Ref. [37] for periodic boundary condition is also plotted. Also shown are the linear fits to the data Ref. [37] (green lines) and the data for open boundary condition (blue lines).	82
8.1	Plot of $\langle \bar{E}(x_0) \rangle$ versus x_0 at flow time $t = t_0$ at $\beta = 6.21$ and lattice volume $24^3 \times 48$ for ensemble O_1 (filled circle) and ensemble P_1 (filled square). . .	87
8.2	Plot of $\langle \bar{E}(x_0) \rangle$ versus x_0 at various flow times t at $\beta = 6.21$ and lattice volume $24^3 \times 48$ for ensemble O_1 (left) and for ensemble P_1 (right). . . .	88
8.3	Plot of glueball effective mass $am_{eff}(0^{++})$ versus the temporal difference x_0 at Wilson flow times $\sqrt{8t} = 0.28$ fm, $\beta = 6.42$ and lattice volume $32^3 \times 64$ for ensemble P_2 for improved and unimproved choices of operators. The lower panel shows the detail of the plateau region of the upper panel.	89
8.4	Plot of lowest glueball effective mass $am_{eff}(0^{++})$ versus x_0 at four different Wilson flow times t , $\beta = 6.42$ and lattice volume $32^3 \times 64$ for ensemble P_2 . Also shown is the fit to the plateau region of the data for $\sqrt{8t} = 0.35$ fm.	90
8.5	Plot of lowest glueball effective mass $am_{eff}(0^{++})$ versus x_0 at five HYP smearing levels at $\beta = 6.42$ and lattice volume $32^3 \times 64$ for ensemble P_2 . Also shown is the fit to the plateau region of the data for smear level 18. . .	91
8.6	Comparison of lowest glueball mass $am_{eff}(0^{++})$ versus x_0 at Wilson flow time ($\sqrt{8t} = 0.35$ fm), $\beta = 6.42$ and lattice volume $32^3 \times 64$ for ensembles O_2 and P_2	92

8.7 Plot of the lowest glueball mass $m(0^{++})$ in MeV versus a^2 for both open and periodic boundary condition for different lattice spacings and lattice volumes. Also shown is the fit to the combined data. 94

CHAPTER 1

Introduction

Quantum Chromodynamics (QCD) is the quantum field theory of strong interactions, a non-abelian gauge theory with symmetry group $SU(3)$, formulated in terms of quarks and gluons. From the early age of quantum field theory, studied with the aid of perturbation theory, infinities and consequently the necessity for renormalization have been with us. Perturbative methods have been very successful in predicting phenomena at small distances, where the coupling constant of QCD is small. These perturbative methods start from a free theory and treat the coupling as a small perturbation to this. Therefore they can only work at small coupling. At the scale of the hadronic world (about 1 fm), the coupling constant of QCD is too large for such perturbative expansions to work.

Lattice QCD (LQCD) was introduced by Wilson who in a seminal paper in 1974 [1] showed us that using the techniques of non-perturbative space-time lattice regularization, field theoretic calculations can be done from first principles (also see [38]). It has been mentioned later by Wilson himself that J. Smit also formulated lattice gauge theory independently [39, 40]. LQCD is the nonperturbative technique with the least number of free parameters to probe the low energy regime of QCD. LQCD is QCD formulated on a four-dimensional Euclidean space-time lattice. It provides a non-perturbative regularization scheme of QCD: On the finite grid the infinities, which occur in the contin-

uum, are removed. Furthermore, dimensionless ratios of measurable quantities appear to have a finite, well behaved limit when the lattice spacing is taken to 0, the continuum limit. Until today it is the only known gauge invariant and chiral invariant regularization method which allows non perturbative approaches to QCD. All other known regularization schemes are tied closely to the perturbative expansions mentioned above. Various features of lattice quantum field theories are discussed in many excellent books (see for example [41–45]).

Apart from regularizing QCD the lattice also provides a way of putting the theory on a computer and simulating it. However, such simulations turned out to be computationally very demanding. Therefore in the last thirty five years a lot of effort has been invested into improvements of simulation algorithms and the way QCD is discretized.

Whether a lattice discretization is good or bad depends crucially on the way it deals with the symmetries of QCD. The breaking of symmetries when discretizing is unavoidable in many cases. This can be readily seen if one considers continuous rotations, which simply cannot exist on a discrete grid. Breaking of symmetries is acceptable, as long as the symmetries are restored in the continuum limit. In this case the breaking can be seen as a discretization error which can be controlled by making the lattice fine enough. How fine it has to be depends on the discretization. From a pragmatic point of view we could say that one discretization is better than another one, if it allows for coarser lattices.

Putting fermion on a lattice, however, has turned out to be highly non-trivial because of the notorious doubling problem. Naive discretization of the Dirac action leads to 16 solutions (called doublers) in the four dimensional theory. Of course it is clearly unacceptable if one wants to describe nature. Among the various solutions suggested to cure this problem, Wilson fermions [1,2] are conceptually the simplest and straightforward to implement. In the Wilson approach a dimension five operator is added to the action thereby sending the masses of the extra fifteen fermions to the order of the cutoff. Thus the extra fermions decouple in the continuum limit. This discretization preserves gauge invariance. On the

other hand, the Wilson term breaks the chiral symmetry of lattice QCD and it gives rise to additive mass renormalization for the fermion mass and one has to fine tune the mass parameter in the action to achieve the chiral limit of the theory. Chiral symmetry is an approximate symmetry of the light quark flavours of QCD. It would be exact for massless quarks. The Wilson term in the action, which is introduced to remove the doublers, breaks chiral symmetry in accordance with the well-known Nielsen-Ninomiya no-go theorem [46–48]. In their famous no-go theorem they proved that it is impossible to have exact chiral symmetry in a formulation of QCD on a finite lattice that is local and which has the correct number of flavours. Nevertheless, Wilson term reproduces the correct axial anomaly [49–51] even though it leads to additive renormalization for the fermion mass.

The sixteen doublers are classified into five branches. Almost all of the studies so far, both analytical and numerical, have focused on the so-called first (physical) branch. However, very recently, occurrence of an enhanced symmetry has been discovered in the central branch (third branch) [21–23] when the on-site terms (mass term and that from the Wilson term) are absent in the action. The enhanced symmetry prohibits additive renormalization through radiative corrections. Since in this case, the central branch yields six massless fermions, as suggested by ref. [22], an alternative way to simulate twelve flavour non-abelian gauge theories emerges. Such theories are of interest in the context of beyond standard model physics (for recent reviews, see [24, 52–54]). In our work [25], by introducing a generalized Wilson term containing a branch selector index, we investigate the additive fermion mass shift and chiral anomaly to $\mathcal{O}(g^2)$ in lattice perturbation theory for all the branches of the fermion doublers and we have concluded that by appropriately averaging over suitably chosen branches one can reduce cut-off artifacts. Comparing the central branch with all other branches, we find that the central branch, among all the branches of the Wilson fermion, is the most suitable candidate for exploring near conformal lattice field theories.

It can be easily shown that with unimproved Wilson fermions the leading lattice artifact

is in $\mathcal{O}(a)$ and chiral symmetry is explicitly broken in this formulation. There are other lattice formulations which maintain lattice chiral symmetry and/or free from $\mathcal{O}(a)$ lattice artifacts. But these chirally improved fermions are computationally expensive. On the other hand, Wilson formulation is still attractive due to its conceptual simplicity (such as the construction of lattice operators that correspond to the observables in the continuum theory) and it is computationally cheap. However, due to lack of chiral symmetry, there have been persistent concerns about the Wilson formulation with unimproved actions in reproducing the chiral properties of continuum QCD [3, 4].

For the past few years, the chiral properties (chiral anomaly and chiral condensate) [7, 8, 55] of Wilson lattice QCD have been studied. Another important quantity is the chiral behaviour of topological susceptibility. Earlier attempt [5] with naive Wilson fermions and HMC algorithm to verify the suppression of topological susceptibility with decreasing quark mass, expected from chiral Ward identity and chiral perturbation theory, was unable to unambiguously confirm the suppression. In our paper [9], we have addressed this issue and unambiguously demonstrated the suppression of the topological susceptibility with decreasing quark mass and the effects of quark mass, lattice volume and the lattice spacing on the spanning of different topological sectors are presented in this work. Next, we concern about the reflection positivity feature of the naive Wilson fermions action in Euclidean space because it assures the hermiticity property of the Hamiltonian in the Minkowski space. In papers [10, 11], authors have pointed out that the topological charge density correlator (TCDC) in lattice QCD is an important observable which should be negative to show the reflection positivity feature of the lattice action. In the continuum theory, close to the origin the two-point TCDC is negative and singular. From power counting, the singularity $\sim -|x|^{-8}$ up to possible logarithms and hence is non-integrable. As the authors of Ref. [10, 11] pointed out long time ago, divergent behaviour of TCDC has non-trivial consequences for the derivation and interpretation of the Witten-Veneziano (WV) expression [56, 57] for the η' mass. The negativity of the TCDC also has non-trivial consequences related to the nature of topological charge structure in QCD vacuum [58].

Not only reflection positivity issue, one can understand the mechanism of decreasing susceptibility with quark mass through TCDC in lattice. In order to obtain a positive and finite space-time integral (susceptibility), the TCDC should have a positive non-integrable singularity at the origin [10, 11, 59]. Flavour singlet axial Ward-Takahashi identity relates the topological susceptibility χ , which is the four-volume integral of TCDC, to the chiral condensate in the chiral limit [16, 60]. Furthermore, at a given value of the quark mass, χ is suppressed as volume decreases [16, 17]. Recently in our work [9, 36], we have demonstrated the suppression of topological susceptibility with decreasing quark mass and the suppression of χ with decreasing volume was also shown in the case of unimproved Wilson fermion and gauge action. In order to shed light on the mechanisms leading to these suppressions and all these divergences behaviour, in our work [15], we carry out a detailed study of the two-point TCDC.

The most popular algorithm to simulate lattice QCD with Dynamical fermions is the Hybrid Monte Carlo (HMC) [61] and one of its improved variations, namely, Domain Decomposed Hybrid Monte Carlo (DD-HMC) [62–64] aims to achieve significant acceleration of the numerical simulation. Dynamical Wilson fermion simulations at smaller quark masses, smaller lattice spacings and larger lattice volumes on currently available computers have become feasible with recent developments such as DD-HMC algorithm. However, approach to the continuum and chiral limits may still be hampered by the phenomenon of critical slowing down. One of the manifestation of critical slowing down is the increase in autocorrelation times associated with the measurements of various observables. Thus measurements of autocorrelation times help us to evaluate the performance of an algorithm in terms of critical slowing down. In addition, an accurate determination of the uncertainty associated with the measurement of an observable requires a realistic estimation of the autocorrelation of the observable which in turn depends on the various parameters associated with the particular algorithm used. An extensive study of autocorrelation mainly in pure $SU(3)$ gauge theory (Wilson gauge action and Iwasaki gauge action) using DD-HMC algorithm has been carried out by ALPHA collaboration [18].

They have shown that the autocorrelation of some observables depend on the gauge action. They have further shown that the autocorrelation of squared topological charge increases dramatically with decreasing lattice spacing while Wilson loops decouple from the modes which slow down the topological charge as lattice spacing decreases. In the simulations with dynamical fermions, the study becomes more difficult, because the autocorrelation may now depend on number of quark flavours (n_f), the quark masses and the fermion action used [29]. In fact ALPHA collaboration [18] has shown, in the case of $n_f = 2$ QCD with Clover action for a given value of quark mass and lattice volume, that squared topological charge decorrelates faster compared with pure gauge at approximately same lattice spacing. These dependencies and the one on the lattice spacing remain to be studied in detail. In our work [19], we have studied the autocorrelations of a variety of observables measured with DD-HMC algorithm in the case of unimproved Wilson gauge action [1] and unimproved Wilson fermions [2]. Here, we have to say that the measurement of autocorrelation is notoriously difficult, since accurate determination of it may require considerably larger accumulated statistics (total molecular dynamics time). So, in our work, we mainly focus on various trends of autocorrelations we can observe rather than the precise measurement of the integrated autocorrelation times for different observables.

Even though lattice QCD continues to make remarkable progress in confronting experimental data, certain problems have persisted. For example, the spanning of the gauge configurations over different topological sectors become progressively difficult as the continuum limit is approached. This is partly intimately related to the use of periodic boundary condition on the gauge field in the temporal direction of the lattice. As a consequence, in the continuum limit, different topological sectors are disconnected from each other. Thus at smaller and smaller lattice spacings the generated gauge configurations tend to get trapped in a particular topological sector for a very long computer simulation time thus resulting in very large autocorrelations. This may sometime even invalidate the results of the simulation. To partially overcome this problem, using open boundary

conditions (instead of the usual periodic or anti-periodic ones) in the temporal direction of the lattice has been proposed [29]. Lattice gauge theory with such boundary conditions have no barriers between different topological sectors. This has been shown by extensive simulations in SU(3) gauge theory [30]. Even though the open boundary conditions introduce boundary effects and thus complicate the physics analysis, their advantage from the point of view of ergodicity and efficiency have been addressed in simulations of 2+1 flavours of $O(a)$ improved Wilson quarks [31]. Advantages of using open boundary conditions have also been studied in the investigation of SU(2) lattice gauge theory at weak coupling [65]. The spanning of different topological sectors can be studied through topological susceptibility (χ) which is related to the η' mass by the Witten-Veneziano formula [10, 56, 57] in pure Yang-Mills lattice theory. For example, some high precision calculations of χ on periodic lattices are provided in Refs. [37, 66, 67]. We have performed simulations with open boundary conditions as well periodic boundary conditions with same set of lattice parameters. It is well known in condensed matter systems that under certain circumstances open boundary conditions sometimes give unreliable results (see for example [34]). In our work [33], we have addressed the question whether open boundary condition in the temporal direction can yield the expected value of χ . We have shown that with the open boundary it is possible to get the expected value of χ and the result agrees with our own numerical simulation employing periodic boundary condition. Apart from topological susceptibility, one may ask also whether open boundary condition can reproduce any other observables calculated with periodic boundary condition. In our work [35], we have found that the extracted scalar glueball mass using open and periodic boundary conditions at the same lattice volume and lattice spacing agree for the range of lattice scales explored in the range $3 \text{ GeV} \leq \frac{1}{a} \leq 5 \text{ GeV}$. The problem of trapping is overcome to a large extent with open boundary and we are able to extract the glueball mass at even larger lattice scale $\approx 5.7 \text{ GeV}$. To smoothen the gauge fields we have used recently proposed Wilson flow which, compared to HYP smearing, exhibits better systematics in the extraction of glueball mass. The extracted glueball mass shows remarkable insensi-

tivity to the lattice spacings in the range explored in our work, $3 \text{ GeV} \leq \frac{1}{a} \leq 5.7 \text{ GeV}$.

The thesis is organized as follows. The next chapter is supposed to be a short recapitulation of the QCD basics in the continuum, including the introduction of the lattice as a regularization scheme and the discretization of the gauge part and the fermion part of the QCD actions are defined. When discretizing the fermion part a problem, called the fermion doubling problem, occurs. Then we have discussed how to cure this problem. Being familiar with the doubling problem and its removal, in chapter 3, light is shed on the different branches of the doubler. To investigate the effect of radiative corrections, in this chapter, we have calculated the additive mass renormalization in fermion self-energy and the chiral anomaly to $O(g^2)$ in perturbation theory for all the branches. Thereafter attention is given to calculation of different observables and about the precise measurements of errors of the different observables. In chapter 4, we have discussed the topological charge density correlator and its different properties. Then in chapter 5, to estimate the precise measurements of errors, we have studied the autocorrelations of a variety of observables measured with DD-HMC algorithm in the case of unimproved Wilson fermions. After that in chapter 6, we have talked about a mathematically well defined smearing technique known as Wilson flow (proposed by Martin Lüscher) to reduce the effect of the fluctuations of the gauge fields in order to improve the accessibility of the signals. As we discussed previously, trapping of topological charge is an important issue as one try to go near continuum limit. At last, in chapter 7 and 8, we have discussed about the implementation of open boundary condition to avoid the trapping problem and calculated the topological susceptibility and the scalar glueball mass using open and periodic boundary conditions lattice.

CHAPTER 2

Quantum Chromodynamics on the lattice

In this chapter, we review some basics of the lattice discretization of Quantum Chromodynamics (QCD). QCD, a non-abelian gauge field theory with symmetry group $SU(3)$, is believed to be the right description of strong interactions on the level of quarks and gluons. First, we take a short look about the fundamental fields of QCD and its continuum formulation. After a brief description of continuum QCD we discuss the construction of lattice QCD formulation. Then we discuss construction of Wilson gauge action, naive discretization of the fermionic part of QCD action and doubling problem followed by Wilson fermion action.

2.1 The fields: quark and gluon

In this description quarks and antiquarks are massive spin- $\frac{1}{2}$ fermionic fields that have spatial, Dirac, flavor and color structure. We can denote them by

$$\psi_{\alpha c}^f(x), \bar{\psi}_{\alpha c}^f(x) \tag{2.1}$$

where x is the space-time position of the field, $\alpha = 1, \dots, 4$ gives the Dirac index, $c = 1, 2, 3$ the color index and $f = 1, \dots, N_f$ the flavor of the quark in consideration. Each field $\psi^f(x)$

thus has 12 independent components. In addition the quarks come in six flavours called up, down, strange, charm, bottom and top, which is indicated by flavour index $f = 1, 2, \dots, 6$. In many calculations it is sufficient to include only the lightest two or three flavours of quarks. For our lattice simulations, we will restrict ourselves to two mass-degenerate flavours of quarks.

In addition to the quarks, QCD contains gauge fields describing the gluons,

$$A_\mu(x)_{cd} \quad (2.2)$$

where

$$A_\mu(x) = \sum_{i=1}^8 A_\mu^{(i)}(x) T_i. \quad (2.3)$$

The components $A_\mu^{(i)}(x)$, $i=1, 2, \dots, 8$, are real-valued fields, the so called color components, and the T_i are a basis for traceless hermitian 3×3 matrices. As for the quark fields, the gauge field $A_\mu(x)_{cd}$ has a space-time argument denoted by x and represents a vector field by carrying a Lorentz index μ which labels the direction of the different components in space-time, c, d denote color index and it has no flavour content.

2.2 The QCD action in the continuum

In a 4-dimensional Euclidean space, the action of QCD can be written as

$$\begin{aligned} S^{QCD}[\psi, \bar{\psi}, A] &= S_F^{QCD}[\psi, \bar{\psi}, A] + S_G^{QCD}[A] \\ &= \int d^4x \left(\sum_{f=1}^{N_f} \bar{\psi}^f(x) (\gamma_\mu D_\mu + m^f) \psi^f(x) \right. \\ &\quad \left. + \frac{1}{2} \text{tr}(F_{\mu\nu}(x) F_{\mu\nu}(x)) \right) \end{aligned} \quad (2.4)$$

with the field-strength tensor $F_{\mu\nu}$ given by

$$F_{\mu\nu}(x) = \partial_\mu A_\nu(x) - \partial_\nu A_\mu(x) + ig[A_\mu(x), A_\nu(x)] .$$

S_F stands for the fermionic part of the action, while S_G denotes the purely gluonic part. ψ , $\bar{\psi}$ are Dirac spinors representing the quark and anti quark fields (α and c are suppressed in eq. 2.4), A_μ is the gauge field and g is the coupling constant. D_μ is called a covariant derivative and is given by

$$D_\mu = \partial_\mu + igA_\mu . \tag{2.5}$$

The field strength tensor $F_{\mu\nu}$ and the covariant derivative D_μ are defined such that the total action is invariant under local SU(3) gauge transformations. Notice that A_μ is a non-abelian field and that the resulting self-interactions of the gluon fields give rise to the complex nonlinear behavior which leads to confinement.

2.3 Path integral quantization

Up to this point, we only dealt with continuum formulation of the theory. There are many ways to quantize a theory, all of them having advantages and disadvantages making them especially suitable for different classes of theories. To quantize the theory, we use the path integral formulation developed by Feynman [68]. The generating functional for QCD is

$$Z = \int \mathcal{D}\psi \mathcal{D}\bar{\psi} \mathcal{D}A e^{-S_{QCD}[\psi, \bar{\psi}, A]} \tag{2.6}$$

where we integrate over all possible values of the fields ψ , $\bar{\psi}$ and A . Note, that in the usual Minkowski metric we would have an additional imaginary unit in front of the action, which would cause rapid oscillations, but in Euclidean space the imaginary unit is absent.

Now, the expectation value of an observable $F[\psi, \bar{\psi}, A]$ is given by

$$\langle F \rangle = \frac{1}{Z} \int \mathcal{D}\psi \mathcal{D}\bar{\psi} \mathcal{D}A F[\psi, \bar{\psi}, A] e^{-S_{QCD}[\psi, \bar{\psi}, A]}. \quad (2.7)$$

2.4 Lattice regularization

Quantizing a theory like QCD confronts us with a lot of mathematical challenges. For example, we need a way to compute all possible paths of propagation between two space-time points. One way to alter the theory such that it is mathematically well-defined is to replace continuous space-time with a space-time lattice. For this purpose we discretize space-time through a lattice spacing a on a four dimensional hypercubic lattice Λ , which serves as an ultraviolet regulator. Now we need to find a way to define the elements appearing in the QCD action.

In the following, we present the simplest formulation of a lattice action for QCD, which has been suggested by K. G. Wilson in 1974 [1]. Wilson's approach is to define a lattice theory with an action that is explicitly gauge invariant at any lattice spacing a . The other important demand is, that the lattice action approaches the continuum form in the limit $a \rightarrow 0$. In a naive discretization of the Dirac field, terms involving fermion fields at different space-time points arise. As an example, terms of the type $\bar{\psi}(n)\psi(n+\mu)$, where $n+\mu$ is the neighbor of site n in the positive μ -direction, occur. These terms are not gauge invariant. To obtain gauge invariant expressions, we will need objects that take the role of the gauge-transporter $G(x,y)$ from the continuum theory. In the continuum, it is defined as

$$G(x,y) = P \exp \left(\int_C ig A ds \right) \quad (2.8)$$

where P stands for the path ordered expression, the fields A are the usual gauge fields from the continuum theory and the integral is along a curve C connecting the space-time

points x and y . To construct such an object on the lattice, it is sufficient if we recover the continuum expression in the limit $a \rightarrow 0$. We therefore define link variables U_μ which live on the links between adjacent lattice sites n and $n + \mu$ and are the elements of the gauge group $SU(3)$. U_μ takes the form

$$U_\mu(n) \rightarrow \exp\left(igaA_\mu\left(n + \frac{\mu}{2}\right)\right) \quad (2.9)$$

in $a \rightarrow 0$ limit. It is straight-forward to show, that this construction approximates the continuum gauge transporter up to terms of order a :

$$U_\mu(n) = G(n, n + \mu) + O(a) . \quad (2.10)$$

Therefore, the quark fields ψ and $\bar{\psi}$ live on the lattice sites and, in analogy to the gauge transporter of the continuum quantum field theory, the link variables live on the links between two adjacent lattice sites.

2.5 The Wilson gauge action

It is now straight forward to discretize the gauge part of the action, as the trace over closed loops of link variables. Any such trace over closed loops is a gauge invariant quantity as required for Wilson's construction. Counting each loop only once, the gauge part of the action S_G [1] can then be written as

$$S_G = \frac{\beta}{3} a^4 \sum_{n \in \Lambda} \sum_{\mu < \nu} \text{Re tr}(\mathbf{1} - U_{\mu\nu}(n)) \quad (2.11)$$

where $U_{\mu\nu}(n)$ is the so called plaquette and the quantity β is related to the coupling

$$\beta = \frac{2N_c}{g^2} .$$

N_c is the number of colors.

The plaquette is the smallest possible loop given by the product of four link variables

$$U_{\mu\nu}(n) = U_\mu(n)U_\nu(n+\mu)U_{-\mu}(n+\mu+\nu)U_{-\nu}(n+\nu) \quad (2.12)$$

and $U_{-\mu}(n) = U_\mu^\dagger(n-\mu)$.

2.6 Naive fermions and the doubling problem

A naive discretization of the fermionic part of the action using central differences for the derivatives is given by [2]

$$S_F[\psi, \bar{\psi}, A] = a^4 \sum_{f=1}^{N_f} \sum_{n \in \Lambda} \left(\bar{\psi}^f(n) \sum_{\mu=1}^4 \gamma_\mu \frac{U_\mu(n)\psi^f(n+\mu) - U_\mu^\dagger(n-\mu)\psi^f(n-\mu)}{2a} + m^f \bar{\psi}^f(n)\psi^f(n) \right). \quad (2.13)$$

Taking a look at the free theory (this corresponds to setting all link variables to 1 : $U_\mu(n) \equiv 1 \forall n$) with massless fermions, one can obtain an analytic expression for the Dirac operator and for its inverse, the quark propagator. In momentum space we obtain

$$D(p) = \frac{i}{a} \sum_{\mu=1}^4 \gamma_\mu \sin(ap_\mu),$$

$$(D(p))^{-1} = \frac{-ia}{\sum_{\mu=1}^4 \gamma_\mu \sin(ap_\mu)}. \quad (2.14)$$

At any finite lattice spacing, this expression has a pole not only at $p = (0, 0, 0, 0)$, but also whenever $p_\mu = \frac{\pi}{a}, 0$, which is also the case for a whole set of points

$$\left\{ \left(\frac{\pi}{a}, 0, 0, 0 \right), \left(\frac{\pi}{a}, \frac{\pi}{a}, 0, 0 \right), \dots, \left(\frac{\pi}{a}, \frac{\pi}{a}, \frac{\pi}{a}, \frac{\pi}{a} \right) \right\}.$$

These fifteen unwanted poles are called *doublers*. Thus in the continuum limit ($a \rightarrow 0$), there are 16 mass degenerate fermions in the theory. In reality we should get only one fermion.

2.7 Removing doublers

To solve this problem, an irrelevant term so-called Wilson term, which vanishes in the continuum limit, can be added to the lattice Dirac operator [2]. In momentum space this additional term reads

$$W(p) = \mathbf{1} \frac{r}{a} \sum_{\mu=1}^4 (1 - \cos(ap_{\mu})) \quad (2.15)$$

where r is called the Wilson parameter. and the whole momentum space Dirac operator including the Wilson term is given by

$$\begin{aligned} D_W &= D + W \\ &= \mathbf{1}m + \frac{i}{a} \sum_{\mu=1}^4 \gamma_{\mu} \sin(ap_{\mu}) + \mathbf{1} \frac{r}{a} \sum_{\mu=1}^4 (1 - \cos(ap_{\mu})) . \end{aligned} \quad (2.16)$$

Due to Wilson term, the pole $p_{\mu} = (0, 0, 0, 0)$ is the physical one where the mass of the fermion is m . Other fifteen unwanted poles have the effective mass $m + 2n\frac{r}{a}$ (where $n = 1, 2, 3, 4$ for the respective poles) and in the continuum limit ($a \rightarrow 0$) they become infinitely heavy and get decoupled from the spectrum. Notice that, just like a quark mass term, such a term also breaks chiral symmetry explicitly.

2.8 Wilson fermion and gauge actions

The standard Wilson fermion action [2] for QCD is given by (suppressing flavour index)

$$\begin{aligned} S_F[\psi, \bar{\psi}, U] &= a^4 \sum_{m,n} \bar{\psi}_m [\gamma_\mu D_\mu + W + m]_{mn} \psi_n \\ &= a^4 \sum_{m,n} \bar{\psi}_m M_{mn} \psi_n \end{aligned} \quad (2.17)$$

where

$$\begin{aligned} [D_\mu]_{mn} &= \frac{1}{2a} \left[U_{m,\mu} \delta_{m+\mu,n} - U_{m-\mu,\mu}^\dagger \delta_{m-\mu,n} \right] \longrightarrow \text{discretized Dirac operator,} \\ W_{mn} &= \frac{r}{2a} \sum_{\mu} \left[2\delta_{m,n} - U_{m,\mu} \delta_{m+\mu,n} - U_{m-\mu,\mu}^\dagger \delta_{m-\mu,n} \right] \longrightarrow \text{Wilson term.} \end{aligned}$$

Here, one can write the action (eq. 2.17) in other parameterization also where the matrix M takes form

$$M_{mn} = \delta_{mn} - \kappa \left[(r - \gamma_\mu) U_{m,\mu} \delta_{n,n+\mu} + (r + \gamma_\mu) U_{m-\mu,\mu}^\dagger \delta_{n,n-\mu} \right] \quad (2.18)$$

where $\kappa = \frac{1}{2(m+4r)}$ is the Wilson's hopping parameter. This also amounts to different normalization of ψ , namely $\psi \rightarrow \sqrt{2\kappa}\psi$. The common choice is to take $r = 1$ which is also used in our numerical simulation.

It can be easily shown that in naive continuum limit i.e. $a \rightarrow 0$ in the lattice action

$$S_F \longrightarrow S_F^{QCD} + \mathcal{O}(a), \quad (2.19)$$

$$S_G \longrightarrow S_G^{QCD} + \mathcal{O}(a^2). \quad (2.20)$$

Thus the leading lattice artifact in unimproved Wilson formulation is in $\mathcal{O}(a)$ and chiral symmetry is explicitly broken in this formulation.

CHAPTER 3

Wilson fermions: a perturbative analysis

3.1 Introduction

As we have discussed in the previous chapter, fermion on a lattice has turned out to be highly non-trivial because of the doubling problem. Naive discretization of the Dirac action leads to 16 solutions (called doublers) in the four dimensional theory. The sixteen doublers are classified into five branches. Almost all of the studies so far, both analytical and numerical, have focused on the so-called first (physical) branch. However, very recently, occurrence of an enhanced symmetry has been discovered in the central branch [21–23] when the on-site terms (mass term and that from the Wilson term) are absent in the action. The enhanced symmetry prohibits additive renormalization through radiative corrections. Since in this case, the central branch yields six massless fermions, as suggested by ref. [22], an alternative way to simulate twelve flavour non-abelian gauge theories emerges. In gauge theory with fermions for a certain numbers of flavours, there exists a possibility that the beta function vanishes and the theory becomes conformally invariant (for example, in one-loop perturbation theory beta function changes sign between $n_f = 16$ and $n_f = 17$). Such theories are of interest in the context of beyond standard model physics; for example, dynamical electroweak symmetry breaking and technicolor

theories (for recent reviews, see [24, 52–54]).

In this chapter, by introducing a generalized Wilson term containing a branch selector index, we investigate the additive fermion mass shift and chiral anomaly to $\mathcal{O}(g^2)$ in lattice perturbation theory for all the branches of the fermion doublers.

3.2 Different branches of Wilson fermions

In the previous chapter, we have already briefly discussed the fermions doubling problem and its solution proposed by Wilson. In this chapter we begin with a detail discussion of this subject. For the sake of completeness and ease of presentation, we repeat some of the steps already presented in the previous chapter. Consider the free massless lattice fermion action,

$$S = a^4 \sum_x \left[\sum_{\mu} \bar{\psi}(x) \gamma_{\mu} \frac{\psi(x+\mu) - \psi(x-\mu)}{2a} \right]. \quad (3.1)$$

Free fermion propagator in momentum space, the inverse of the Dirac operator,

$$G(p) = \frac{1}{\sum_{\mu=1}^4 \frac{i}{a} \gamma_{\mu} \sin(ap_{\mu})}. \quad (3.2)$$

At any finite lattice spacing, this expression has a pole not only at $p_{\mu} = (0, 0, 0, 0)$, but also whenever $p_{\mu} = \{(\frac{\pi}{a}, 0, 0, 0), (\frac{\pi}{a}, \frac{\pi}{a}, 0, 0), \dots, (\frac{\pi}{a}, \frac{\pi}{a}, \frac{\pi}{a}, \frac{\pi}{a})\}$. These fifteen unwanted poles are called doublers. Let us now look at its behaviour at some regions where the momentum components are near zero or close to their maximum value $\frac{\pi}{a}$. Let us write $p_{\mu} = k_{\mu} + p_{\mu}^D$, with $D = 0$ to 15 where $p_{\mu}^D = (0, 0, 0, 0), (\frac{\pi}{a}, 0, 0, 0), \dots, (\frac{\pi}{a}, \frac{\pi}{a}, \frac{\pi}{a}, \frac{\pi}{a})$, so that $\sin(ap_{\mu}) = \cos(ap_{\mu}^D) \sin(ak_{\mu}) = \pm \sin(ak_{\mu})$.

Branch	P_μ^D	No. of such types	New set of γ 's	γ_5
First	(0,0,0,0)	1	$(\gamma_1, \gamma_2, \gamma_3, \gamma_4)$	$+\gamma_5$
Second	$(\frac{\pi}{a}, 0, 0, 0)$ $(0, \frac{\pi}{a}, 0, 0)$ $(0, 0, \frac{\pi}{a}, 0)$ $(0, 0, 0, \frac{\pi}{a})$	4	$(-\gamma_1, \gamma_2, \gamma_3, \gamma_4)$ $(\gamma_1, -\gamma_2, \gamma_3, \gamma_4)$ $(\gamma_1, \gamma_2, -\gamma_3, \gamma_4)$ $(\gamma_1, \gamma_2, \gamma_3, -\gamma_4)$	$-\gamma_5$
Third (Central)	$(\frac{\pi}{a}, \frac{\pi}{a}, 0, 0)$ $(\frac{\pi}{a}, 0, \frac{\pi}{a}, 0)$ $(\frac{\pi}{a}, 0, 0, \frac{\pi}{a})$ $(0, \frac{\pi}{a}, \frac{\pi}{a}, 0)$ $(0, \frac{\pi}{a}, 0, \frac{\pi}{a})$ $(0, 0, \frac{\pi}{a}, \frac{\pi}{a})$	6	$(-\gamma_1, -\gamma_2, \gamma_3, \gamma_4)$ $(-\gamma_1, \gamma_2, -\gamma_3, \gamma_4)$ $(-\gamma_1, \gamma_2, \gamma_3, -\gamma_4)$ $(\gamma_1, -\gamma_2, -\gamma_3, \gamma_4)$ $(\gamma_1, -\gamma_2, \gamma_3, -\gamma_4)$ $(\gamma_1, \gamma_2, -\gamma_3, -\gamma_4)$	$+\gamma_5$
Fourth	$(\frac{\pi}{a}, \frac{\pi}{a}, \frac{\pi}{a}, 0)$ $(\frac{\pi}{a}, \frac{\pi}{a}, 0, \frac{\pi}{a})$ $(\frac{\pi}{a}, 0, \frac{\pi}{a}, \frac{\pi}{a})$ $(0, \frac{\pi}{a}, \frac{\pi}{a}, \frac{\pi}{a})$	4	$(-\gamma_1, -\gamma_2, -\gamma_3, \gamma_4)$ $(-\gamma_1, -\gamma_2, \gamma_3, -\gamma_4)$ $(-\gamma_1, \gamma_2, -\gamma_3, -\gamma_4)$ $(\gamma_1, -\gamma_2, -\gamma_3, -\gamma_4)$	$-\gamma_5$
Fifth	$(\frac{\pi}{a}, \frac{\pi}{a}, \frac{\pi}{a}, \frac{\pi}{a})$	1	$(-\gamma_1, -\gamma_2, -\gamma_3, -\gamma_4)$	$+\gamma_5$

Table 3.1: Different branches of the Wilson fermions.

In $a \rightarrow 0$ limit the propagator takes the usual form

$$\left[i \sum_{\mu} \gamma_{\mu}^D k_{\mu} \right]^{-1} \quad (3.3)$$

with $\gamma_{\mu}^D = \cos(ap_{\mu}^D) \gamma_{\mu} = \pm \gamma_{\mu}$.

In table 3.1, we have shown that according to the distributions of poles, we can divide them into five branches. Then we know that doublers are removed by adding dimension five Wilson term in the action. Thus in that way, the first branch is the physical one and all other branches (second, third, fourth and fifth), get decoupled from the spectrum when one takes the continuum limit of the theory.

3.3 Making a particular branch physical one

Now, we can make a particular branch physical one through a branch selector index (i_B).

We denote the generalized Wilson fermion action by

$$\begin{aligned}
 S_F[\psi, \bar{\psi}, U](i_B) &= a^4 \sum_{x,y} \bar{\psi}_x M_{xy}(i_B) \psi_y = a^4 \sum_{x,y} \bar{\psi}_x [\gamma_\mu D_\mu + W(i_B) + m]_{xy} \psi_y \quad \text{with} \\
 [D_\mu]_{xy} &= \frac{1}{2a} \left[U_{x,\mu} \delta_{x+\mu,y} - U_{x-\mu,\mu}^\dagger \delta_{x-\mu,y} \right] \quad \text{and} \\
 W_{xy}(i_B) &= \frac{r}{2a} \sum_\mu \left[2\left(1 - \frac{1}{2}i_B\right) \delta_{x,y} - U_{x,\mu} \delta_{x+\mu,y} - U_{x-\mu,\mu}^\dagger \delta_{x-\mu,y} \right]. \quad (3.4)
 \end{aligned}$$

The factor i_B is the branch selector index which takes the values 0, 1, 2, 3, and 4 for first, second, third (central), fourth and fifth branch of the doubler respectively. Different values of i_B give different values to the Wilson mass. Particularly interesting the value of $i_B = 2$ which makes the Wilson mass term vanish.

Hence the free fermion propagator for the action will be

$$aG(p) = \frac{1}{i \sum_\mu \gamma_\mu \frac{\sin ap_\mu}{a} + m + \frac{r}{a} \sum_\mu \left(\left(1 - \frac{1}{2}i_B\right) - \cos ap_\mu \right)}. \quad (3.5)$$

From the eq. 3.5, we can conclude that for a particular branch index (i_B), corresponding branch will be physical one and at that time other branches will be decoupled from the spectrum.

3.4 Enhanced symmetry

In continuum we know that if the original action (massless theory) is chirally symmetric then we can not generate mass term through perturbative calculation provided the regulator respects the symmetry. But this is not the case for Wilson fermion. The Wilson term in the action, which is introduced to remove doublers, breaks chiral symmetry and leads to additive renormalization for the fermion mass. To prevent additive mass renormalization, an enhanced symmetry is required in the action. This enhanced symmetry transformation

is introduced in [22], on the fermion field,

$$\psi_x \rightarrow \psi'_x = e^{i\theta(-1)^{x_1+x_2+x_3+x_4}} \psi_x, \quad \bar{\psi}_x \rightarrow \bar{\psi}'_x = \bar{\psi}_x e^{i\theta(-1)^{x_1+x_2+x_3+x_4}}$$

where x_1, x_2, x_3, x_4 are the site index of a site.

The action is invariant under these transformation but for the local terms. For $m = 0$ and $i_B = 2$ (massless limit of the central branch), the action thus possesses this additional symmetry which prevents additive renormalization of the fermion mass through radiative corrections.

3.5 Additive renormalization in fermion self energy

In this section we calculate the additive shift to $\mathcal{O}(g^2)$ in the fermion mass (for $am = 0$) using lattice perturbation theory [69, 70].

The additive shift in fermion mass due to the tadpole diagram (figure 3.1) is

$$\delta m = -\frac{r}{a} \frac{1}{2} g^2 C_F \sum_{\mu} \cos(ap_{\mu}) Z_0 \quad (3.6)$$

with $Z_0 = \int \frac{d^4 k}{(2\pi)^4} \left(4 \sum_{\lambda} \sin^2 \left(\frac{ak_{\lambda}}{2} \right) \right)^{-1}$ and $C_F = \frac{N^2-1}{2N}$ for SU(N).

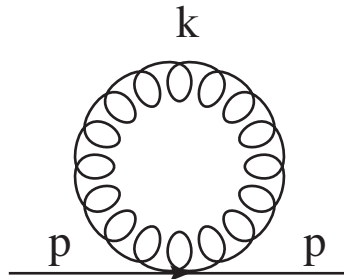


Figure 3.1: Tadpole diagram

Results for different branches are as follows.

First branch: $ap_\mu = (0, 0, 0, 0) \rightarrow \delta m = -2\frac{r}{a}g^2 C_F Z_0$.

Second branch: $ap_\mu = (\pi, 0, 0, 0)$ or any of the other three permutations $\rightarrow \delta m = -1\frac{r}{a}g^2 C_F Z_0$.

Third (central) branch: $ap_\mu = (\pi, \pi, 0, 0)$ or any of the other five permutations $\rightarrow \delta m = 0$.

Fourth branch: $ap_\mu = (\pi, \pi, \pi, 0)$ or any of the other three permutations $\rightarrow \delta m = +1\frac{r}{a}g^2 C_F Z_0$.

Fifth branch: $ap_\mu = (\pi, \pi, \pi, \pi) \rightarrow \delta m = +2\frac{r}{a}g^2 C_F Z_0$.

Next consider the additive mass shift in fermion mass due to sunset diagram. The gauge boson propagator in Feynman gauge is given by

$$G_{\mu\nu}^{ab} = \delta_{\mu\nu} \delta^{ab} \left\{ \frac{4}{a^2} \sum_{\lambda} \sin^2 \frac{a(p-k)_\lambda}{2} \right\}^{-1} = \delta_{\mu\nu} \delta^{ab} \left\{ (1/a^2) \mathcal{W}_{p,k} \right\}^{-1}, \quad (3.7)$$

whereas the fermion propagator has the form

$$S^{lm}(k, i_B) = \delta^{lm} \left\{ \sum_{\mu} i\gamma_{\mu} \frac{\sin(k_{\mu}a)}{a} + \frac{r}{a} \mathcal{M}_k(i_B) \right\}^{-1} \quad (3.8)$$

with

$$\mathcal{M}_k(i_B) = \sum_{\mu} \left[\left(1 - \frac{1}{2} i_B \right) - \cos(k_{\mu}a) \right] \quad (3.9)$$

and the fermion-gauge boson vertex is

$$(V^a)_{\rho}^{mn}(k, p) = -g(T^a)^{mn} \left\{ i\gamma_{\rho} \cos \frac{a(k+p)_{\rho}}{2} + r \sin \frac{a(k+p)_{\rho}}{2} \right\}. \quad (3.10)$$

Then the fermion self energy from sunset diagram can be evaluated as

$$\Sigma = \int \frac{d^4k}{(2\pi)^4} \sum_{\rho} G_{\rho\rho}^{ab}(p-k)(V^b)_{\rho}^{lm}(k,p)S^{mn}(k)(V^a)_{\rho}^{nl}(p,k). \quad (3.11)$$

The additive mass shift arising from the fermion self energy (sunset) can be written as

$$\delta m = \frac{r}{a} g^2 C_F \int \frac{d^4k}{(2\pi)^4} \frac{N_r}{D_r} \quad (3.12)$$

where $D_r = \mathcal{W}_{p,k}(\Gamma^2 + r^2 \mathcal{M}_k^2(i_B))$ with $\Gamma^2 = \sum_{\lambda} \sin^2(ak_{\lambda})$. We introduce $\Gamma_{\lambda} = \sin(ak_{\lambda})$, $S_{\rho} = \sin(\frac{ak_{\rho}}{2})$ and $C_{\rho} = \cos(\frac{ak_{\rho}}{2})$. The expressions for N_r and D_r for different branches are given below.

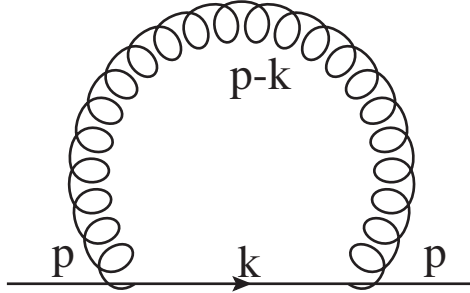


Figure 3.2: Sunset diagram

First branch: $ap_{\mu} = (0, 0, 0, 0)$.

$$N_r = \sum_{\rho=1}^4 \left[\mathcal{M}_k(i_B=0)(r^2 S_{\rho}^2 - C_{\rho}^2) + \Gamma_{\rho}^2 \right],$$

$$D_r = \mathcal{W}_{p,k} \left[\Gamma^2 + r^2 \mathcal{M}_k^2(i_B=0) \right].$$

Second branch: $ap_{\mu} = (\pi, 0, 0, 0)$ or three other permutations.

Explicitly for $ap_\mu = (\pi, 0, 0, 0)$

$$N_r = - \left[\mathcal{M}_k(i_B = 1)(S_\rho^2 - r^2 C_\rho^2) + \Gamma_\rho^2 \right]_{\rho=1} + \sum_{\rho=2}^4 \left[\mathcal{M}_k(i_B = 1)(r^2 S_\rho^2 - C_\rho^2) + \Gamma_\rho^2 \right],$$

$$D_r = \mathcal{W}_{p,k} \left[\Gamma^2 + r^2 \mathcal{M}_k^2(i_B = 1) \right].$$

Third (central) branch: $ap_\mu = (\pi, \pi, 0, 0)$ or five other permutations.

Explicitly for $ap_\mu = (\pi, \pi, 0, 0)$

$$N_r = - \sum_{\rho=1}^2 \left[\mathcal{M}_k(i_B = 2)(S_\rho^2 - r^2 C_\rho^2) + \Gamma_\rho^2 \right] + \sum_{\rho=3}^4 \left[\mathcal{M}_k(i_B = 2)(r^2 S_\rho^2 - C_\rho^2) + \Gamma_\rho^2 \right],$$

$$D_r = \mathcal{W}_{p,k} \left[\Gamma^2 + r^2 \mathcal{M}_k^2(i_B = 2) \right].$$

Fourth branch: $ap_\mu = (\pi, \pi, \pi, 0)$ or three other permutations.

Explicitly for $ap_\mu = (\pi, \pi, \pi, 0)$

$$N_r = - \sum_{\rho=1}^3 \left[\mathcal{M}_k(i_B = 3)(S_\rho^2 - r^2 C_\rho^2) + \Gamma_\rho^2 \right] + \left[\mathcal{M}_k(i_B = 3)(r^2 S_\rho^2 - C_\rho^2) + \Gamma_\rho^2 \right]_{\rho=4},$$

$$D_r = \mathcal{W}_{p,k} \left[\Gamma^2 + r^2 \mathcal{M}_k^2(i_B = 3) \right].$$

Fifth branch: $ap_\mu = (\pi, \pi, \pi, \pi)$.

$$N_r = - \sum_{\rho=1}^4 \left[\mathcal{M}_k(i_B = 4)(S_\rho^2 - r^2 C_\rho^2) + \Gamma_\rho^2 \right],$$

$$D_r = \mathcal{W}_{p,k} \left[\Gamma^2 + r^2 \mathcal{M}_k^2(i_B = 4) \right].$$

In table 3.2 we present the numerical values of the additive mass shift separately from sunset and tadpole contributions for the fermion at different branches. In figure 3.3 we plot the magnitude of the total additive mass shift (tadpole + sunset) versus the branch number. Note that the shift is maximum for the first and the fifth branches and is minimum (zero) for the third (central) branch. The absence of additive renormalization in fermion self energy for the central branch to $\mathcal{O}(g^2)$ is explicitly shown also in ref. [23].

Branch	$\delta m / (g^2 C_F)$	
	Sunset	Tadpole
First	-0.0158	-0.3099
Second	+0.0148	-0.1549
Third	0.0000	0.0000
Fourth	-0.0148	+0.1549
Fifth	+0.0158	+0.3099

Table 3.2: Numerical values of the additive mass shift for fermion at different branches for $r = 1$ and $L = 200$.

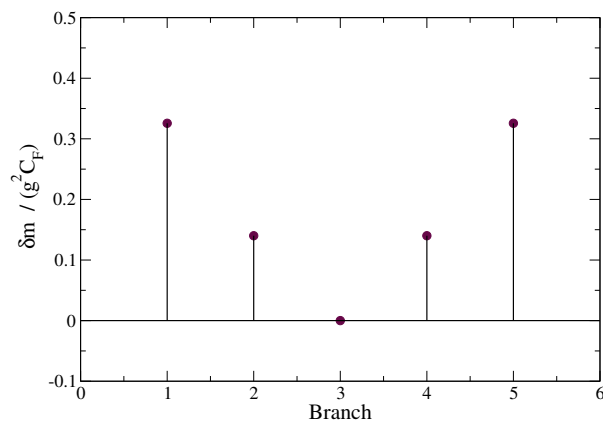


Figure 3.3: The magnitude of the total additive mass shift (tadpole + sunset) plotted versus the branch number.

3.6 Chiral anomaly

We know that with the conventional Wilson term ($i_B = 0$) in the continuum limit, apart from the first branch, species corresponding to all other branches become infinitely massive and decouple from the theory thereby reproducing the correct chiral anomaly. In order to explore all branches, we introduced a generalized Wilson term containing a branch selector index (i_B). By choosing i_B , one can make the fermions belonging to a particular branch physical. Now one can ask a natural question : in the continuum limit, can all the branches reproduce correct chiral anomaly.

The following discussion is based on the Refs. [49, 50] which studied the physical branch. Consider the flavour singlet axial transformation

$$\psi_x \rightarrow \psi'_x = [1 - i\gamma_5 \alpha_x] \psi_x, \quad \bar{\psi}_x \rightarrow \bar{\psi}'_x = \bar{\psi}_x [1 - i\gamma_5 \alpha_x]$$

Then the Ward identity can be obtained from the fact that the partition function remains invariant under this transformation. So, the flavor singlet axial Ward Identity is

$$\langle \Delta_\mu^b J_{5\mu}(x) \rangle = 2m \langle \bar{\psi}_x \gamma_5 \psi_x \rangle + \langle \chi_x \rangle \quad (3.13)$$

where $\langle \mathcal{O} \rangle$ denotes the functional average of \mathcal{O} . Explanation of other terms are as follows:

$$\Delta_\mu^b f(x) = \frac{1}{a} [f(x) - f(x - \mu)] \text{ , the backward derivative,} \quad (3.14)$$

$$J_{5\mu}(x) = \frac{1}{2} \left[\bar{\psi}_x \gamma_\mu \gamma_5 U_{x,\mu} \psi_{x+\mu} + \bar{\psi}_{x+\mu} \gamma_\mu \gamma_5 U_{x\mu}^\dagger \psi_x \right] \text{ , the axial vector current} \quad (3.15)$$

$$\begin{aligned} \text{and } \langle \chi_x \rangle &= 2 g^2 \varepsilon_{\mu\nu\rho\lambda} \text{tr}_C \left(F_{\mu\nu}(x) F_{\rho\lambda}(x) \right) \frac{1}{(2\pi)^4} \sum_p \cos(p_\mu a) \cos(p_\nu a) \cos(p_\rho a) \\ &\quad \times r \mathcal{M}_p(i_B) \left[\cos(p_\lambda a) [am + r \mathcal{M}_p(i_B)] - 4r \sin^2(p_\lambda a) \right] (\mathcal{G}_p(i_B))^3, \\ &= -\frac{g^2}{16\pi^2} \varepsilon_{\mu\nu\rho\lambda} \text{tr}_C \left(F_{\mu\nu}(x) F_{\rho\lambda}(x) \right) I(am, r, L). \end{aligned} \quad (3.16)$$

Here

$$\mathcal{G}_p(i_B) = \left(\sum_{\mu} \sin^2(ap_{\mu}) + [am + r\mathcal{M}_p(i_B)]^2 \right)^{-1} \quad (3.17)$$

and tr_C denotes the trace over the colour space and L denotes the dimensionless length of the hypercubic box of space-time lattice. $\sum_p \equiv \sum_{p_1, p_2, p_3, p_4}$ where $p_{\mu} = 2\pi n_{\mu}/L$, $n_{\mu} = 0, 1, \dots, L-1$ for periodic boundary condition and $n_{\mu} = -L/2 + 1, -L/2 + 2, \dots, L/2$ for anti periodic boundary condition. In all our plots it is the anomaly integral denoted by the function $I(am, r, L)$ which we have plotted.

Following Karsten and Smit [49], the limits on the momentum sum are changed from $(-\pi, +\pi)$ to $(-\pi/2, 3\pi/2)$ and further the momentum sum hypercube is divided into 16 smaller hypercubes corresponding to $(-\pi/2, +\pi/2)$ and $(+\pi/2, +3\pi/2)$ for each $ap_{\mu}, \mu = 1, 2, 3, 4$. Thus the total anomaly contribution is decomposed into the contributions from five different types of species and the anomaly integral takes the form $I = I_0 - 4I_1 + 6I_2 - 4I_3 + I_4$. In I_0 all the four momentum integrations range from $(-\pi/2, +\pi/2)$ and in I_4 they range from $(+\pi/2, +3\pi/2)$. In I_1 one of the momentum integrations ranges from $(+\pi/2, +3\pi/2)$, the rest from $(-\pi/2, +\pi/2)$ and vice-versa for I_3 . In the third (central) branch I_2 two momentum integrations range from $(+\pi/2, +3\pi/2)$ and the rest from $(-\pi/2, +\pi/2)$.

First, to perform the integration analytically, we set the bare mass $am = 0$, use the identity [49]

$$\begin{aligned} [\mathcal{M}_p(i_B)]^2 \cos(ap_{\beta}) - 4r \mathcal{M}_p(i_B) \sin^2(ap_{\beta}) &= \left[[\mathcal{M}_p(i_B)]^2 + \sum_{\sigma} \sin^2(ap_{\sigma}) \right]^3 \\ &\times \frac{\partial}{\partial(ap_{\beta})} \left[\sin(ap_{\beta}) \left\{ [\mathcal{M}_p(i_B)]^2 + \sum_{\sigma} \sin^2(ap_{\sigma}) \right\} \right]^{-2} \end{aligned} \quad (3.18)$$

and do a partial integration. In the infinite volume continuum limit, the results for the

integrals are as follows.

First branch: $I_0 \rightarrow 1, I_1, I_2, I_3, I_4 \rightarrow 0$.

Second branch: $I_1 \rightarrow 1, I_0, I_2, I_3, I_4 \rightarrow 0$.

Third (central) branch: $I_2 \rightarrow 1, I_0, I_1, I_3, I_4 \rightarrow 0$.

Fourth branch: $I_3 \rightarrow 1, I_0, I_1, I_2, I_4 \rightarrow 0$.

Fifth branch: $I_4 \rightarrow 1, I_0, I_1, I_2, I_3 \rightarrow 0$.

Since numerical simulations are performed at finite volume and finite lattice spacing, it is of interest to study the effect of symmetry violation on the anomaly integral as a function of the lattice fermion mass at finite volume [7, 55]. In order to avoid the zero mode problem we have used antiperiodic boundary condition in all four directions. In figure 3.4 we plot the function $I(am, r, L)$ for $r = 1.0$ and $L = 100$ as a function of am for the first and fifth branches (left) and for the second and fourth branches (right). In figure 3.5, we plot the function $I(am, r, L)$ for $r = 1.0$ and $L = 100$ as a function of am for the central branch. From figure 3.4 (left), we observe that the cut-off effects are almost equal and opposite for first and fifth branches. Similar observation can be made regarding second and fourth branches from figure 3.4 (right). Comparing figures 3.4 and 3.5, we conclude that cut-off effects are minimal for the central branch. In a previous study [7], the finite volume effects were studied in detail (figure 4). It was found that for the range of quark masses studied here, $L= 100$ is enough to avoid finite volume effects. We have picked $L = 100$ for our plots as we have reconfirmed that finite volume effects are negligible at this volume for the range of am shown in the figures.

3.7 Discussion and conclusions

It is well known that the naive discretization of the fermionic action gives rise to sixteen degenerate species including the desired physical one. These sixteen species are grouped into five branches with degeneracy (chirality) given by 1(1), 4(-1), 6(1), 4(-1) and 1(1), rendering the theory free of chiral anomaly. With the conventional Wilson term in the

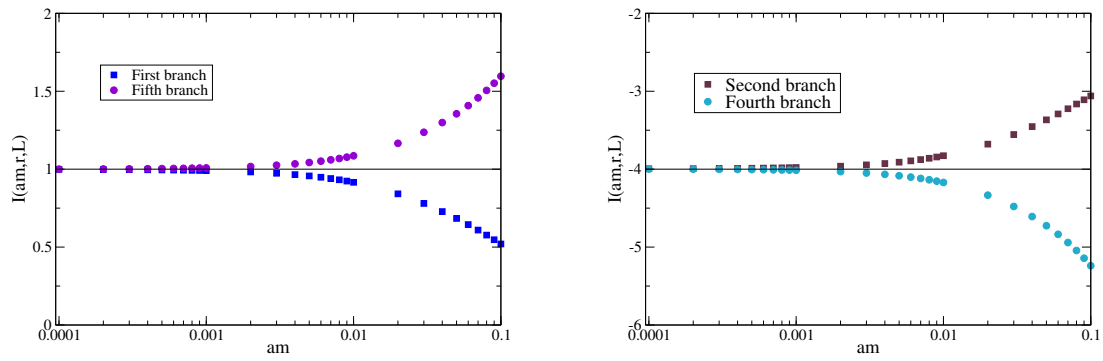


Figure 3.4: The function $I(am, r, L)$ for $r = 1.0$ and $L = 100$ as a function of am for the first and fifth branches (left) and for the second and fourth branches (right).

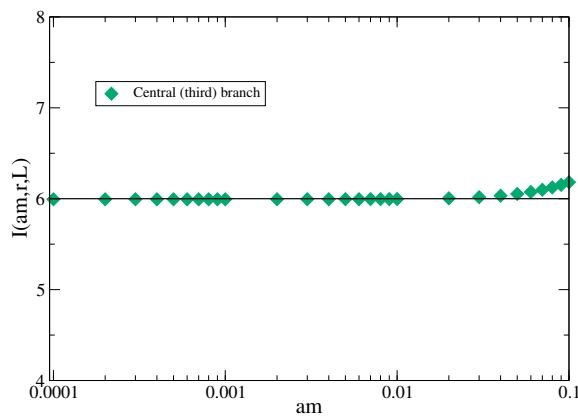


Figure 3.5: The function $I(am, r, L)$ for the central branch for $r = 1.0$ and $L = 100$ as a function of am .

continuum limit, apart from the first branch, species corresponding to all other branches become infinitely massive and decouple from the theory thereby reproducing the correct chiral anomaly. The branches other than the first one are rarely explored. However, recently the existence of an additional symmetry in the central branch which prohibits additive renormalization of fermion mass has been discovered in the ref. [22].

In this work, in order to explore all branches we introduce a generalized Wilson term containing a branch selector index (i_B). By choosing i_B one can make the fermions belonging to a particular branch physical. The fermions belonging to the rest of the branches become infinitely massive and decouple from the theory in the continuum limit. The conventional Wilson term corresponds to $i_B = 0$. To investigate the effect of radiative corrections, we calculate the additive mass renormalization in fermion self-energy and the chiral anomaly to $\mathcal{O}(g^2)$ in perturbation theory for all the branches.

First we summarize the results of additive mass shift from tadpole and sunset contributions. The tadpole contributions for the first and fifth branches are equal in magnitude but opposite in sign. Same is true for the sunset contributions also. Thus δm vanishes if we average over the first and fifth branches. Similar observations hold for the second and the fourth branches also. Coming to the central branch the additive mass shifts from tadpole and sunset contributions separately vanish. This leads to the absence of additive mass renormalization in accordance with theoretical expectation. In the calculation of chiral anomaly first we perform an analytical calculation setting $am = 0$ and using the Karsten-Smit identity. We find the correct value of the anomaly for different branches with corresponding degeneracy factors and signs dictated by the chiral charges in the continuum limit. Since numerical simulations are performed at finite volume, finite lattice spacing and finite fermion mass, we have studied the effect of symmetry violation (given in eq. 3.6) on the anomaly integral as a function of the lattice fermion mass. The cut-off effects are almost equal in magnitude but opposite in sign for the first and the fifth branches. Same holds for the second and the fourth branches also. The cut-off effect is

minimal for the central branch.

In conclusion, our exploration of the different branches of the fermion doublers in perturbation theory, in the context of additive mass renormalization and chiral anomaly, has shown that by appropriately averaging over suitably chosen branches one can reduce cut-off artifacts. Comparing the central branch with all other branches, we find that the central branch, among all the avatars of the Wilson fermion, is the most suitable candidate for exploring near conformal lattice field theories [24, 52–54].

CHAPTER 4

Topological charge density correlator with Wilson fermions

4.1 Introduction

We concern about the reflection positivity feature of the lattice action in Euclidean space because it assures the hermiticity property of the Hamiltonian in the Minkowski space. As a consequence of the reflection positivity and the pseudoscalar nature of the relevant local operator in Euclidean quantum field theory, the two-point Topological Charge Density Correlator (TCDC) is negative at arbitrary non-zero distances [10, 11]. As the authors of Ref. [10, 11] pointed out long time ago, divergent behaviour of TCDC has non-trivial consequences for the derivation and interpretation of the Witten-Veneziano (WV) expression [56, 57] for the η' mass. In order to obtain a positive and finite space-time integral (susceptibility), the TCDC should have a positive non-integrable singularity at the origin [10, 11, 59]. However, it is possible to give a rigorous definition of topological susceptibility in Lattice QCD without power divergences using Ginsparg-Wilson fermion [71–73].

The lattice operator for the topological charge density $q(x)$ may extend over several lattice

spacings, and thus for sufficiently small x , the continuum like behaviors are not expected. Nevertheless, continuum properties are expected to emerge as lattice spacings become smaller and smaller. Specifically, on a lattice with lattice spacing a , TCDC remains positive within a radius r_c , which is expected to shrink to zero as $a \rightarrow 0$. The first investigation of lattice spacing dependence of the radius of the positive core and the negativity beyond the positive core of TCDC in lattice QCD was carried out in Ref. [74] in the context of overlap based topological charge density in quenched QCD. Later, similar study was carried out [75] for a variety of lattice QCD actions with and without quarks where discretization errors appear only at $\mathcal{O}(a^2)$.

The issues related to two-point TCDC are best studied in the theory rigorously formulated on a Euclidean lattice. However, the lattice theory defined by a particular action may not be reflection positive. Fortunately, this is not a concern for the Wilson fermion. However, the breaking of chiral symmetry by Wilson term may lead to uncanceled divergences in topological susceptibility. Thus it is important to calculate topological susceptibility with Wilson fermion to check whether the cancellation indeed happens.

Flavour singlet axial Ward-Takahashi identity relates the topological susceptibility χ , which is the four-volume integral of TCDC, to the chiral condensate in the chiral limit [16, 60]. As a consequence, χ vanishes linearly in the quark mass in the chiral limit. Furthermore, at a given value of the quark mass, χ is suppressed as volume decreases [16, 17]. Recently in our work [9, 36], we have demonstrated the suppression of topological susceptibility with decreasing quark mass and the suppression of χ with decreasing volume was also shown in the case of unimproved Wilson fermion and gauge action.

In this chapter, in order to shed light on the mechanisms leading to these suppressions and all these divergent behaviour, we discuss a detailed study of the two-point TCDC.

4.2 Topological charge density correlator $C(r)$

The topological susceptibility (χ) is the volume integral of topological charge density correlator (TCDC)

$$\chi = \int d^4x C(r) \quad (4.1)$$

with the TCDC,

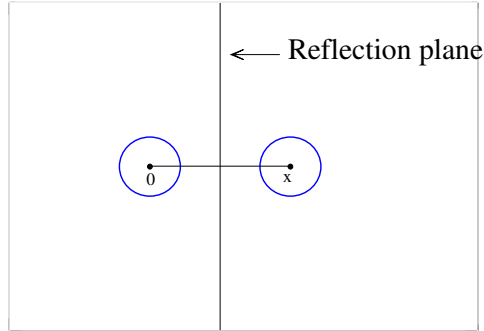
$$C(r) = \langle q(x)q(0) \rangle, \quad r = |x| \quad (4.2)$$

where $q(x) = \frac{g^2}{32\pi^2} \epsilon_{\mu\nu\rho\lambda} \text{tr}_c(F_{\mu\nu}(x)F_{\rho\lambda}(x))$ is the topological charge density and topological charge is defined as $Q = \int d^4x q(x)$.

4.3 Negativity of $C(r)$ due to reflection positivity

The following discussion is based on Ref. [74]. Reflection positivity of an Euclidean theory is equivalent to the hermiticity of the Hamiltonian in the corresponding Minkowski theory. If θ is an operator consisting of Euclidean time reflection and complex conjugation and F is an arbitrary function of the gauge fields at non negative Euclidean time, then the general statement of the reflection positivity is $\langle (\theta F)F \rangle \geq 0$. Since $C(r)$ is a function of only the distance between source and sink point θ can be taken to be reflection of any coordinate. Let us take our new coordinate along the line joining 0 and x with the origin at the midpoint between 0 and x and consider a reflection θ with respect to the axis connecting these points. Due to the pseudoscalar nature of $q(x)$, we have

$$q(x) = -\theta q(0), \quad \text{if } |x| = r > 0.$$



Then

$$\begin{aligned}
 C(r) &= \langle q(x)q(0) \rangle \\
 &= -\langle \theta(q(0))q(0) \rangle \leq 0 \text{ for } x \neq 0.
 \end{aligned}
 \tag{4.3}$$

4.4 Divergences in $C(r)$

$C(r)$ has negative singularity close to the origin as can be shown by operator product expansion (OPE) which is introduced by K.G. Wilson in 1969 [76]. The OPE can be written for products of q as

$$q(x)q(y) \underset{x \rightarrow y}{=} \sum_n c_n(x-y)O_n(y)
 \tag{4.4}$$

where $O_n(y)$'s are the set of local fields and c_n 's are the Wilson coefficients.

Using scale transformation (see sec. III in Ref. [76]) on eq. (4.4), we get

$$U(s)^\dagger q(x)U(s)U(s)^\dagger q(y)U(s) = \sum_n c_n(x-y)U(s)^\dagger O_n(y)U(s). \quad (4.5)$$

Now $U(s)^\dagger q(x)U(s) = s^4 q(sx)$ and $U(s)^\dagger O_n(x)U(s) = s^{d_n} O_n(sx)$. Here d_n is the dimension of the local operators O_n .

Then from eq. (4.5), we get

$$q(sx) q(sy) = \sum_n c_n(x-y)s^{(d_n-8)} O_n(sy). \quad (4.6)$$

By variable redefinition from eq. (4.4) we get

$$q(sx) q(sy) = \sum_n c_n(sx-sy)O_n(sy). \quad (4.7)$$

From eqs. (4.6) and (4.7),

$$c_n(sx-sy) = s^{(d_n-8)} c_n(x-y) \quad (4.8)$$

which implies that

$$c_n(x-y) \xrightarrow{x \rightarrow y} (x-y)^{(d_n-8)}. \quad (4.9)$$

Since $q(x)q(y)$ is a scalar, $O_0 = 1$ and $d_0 = 0$. Then

$$c_0(x-y) \xrightarrow{x \rightarrow y} (x-y)^{-8}. \quad (4.10)$$

Thus $C(r)$ has negative singularity ($\sim \frac{1}{r^8}$) close to the origin and it is also non-integrable in nature.

On the other hand

$$\begin{aligned}\chi &= \int d^4x C(r) \\ &= \frac{\langle Q^2 \rangle}{V}\end{aligned}\tag{4.11}$$

which is positive and finite in nature. Then $C(r)$ has to be non-integrable positive divergent at $x = 0$.

4.5 Simulation Details

$\beta = 5.6$						
<i>tag</i>	<i>lattice</i>	κ	<i>block</i>	N_2	N_{trj}	τ
A_{2b}	$16^3 \times 32$	0.158	8^4	10	6816	0.5
B_{1b}	,,	0.1575	$12^2 \times 6^2$	18	13128	0.5
B_{3b}	,,	0.158	$12^2 \times 6^2$	18	13646	0.5
B_{4b}	,,	0.158125	$12^2 \times 6^2$	18	11328	0.5
B_{5b}	,,	0.15825	$12^2 \times 6^2$	18	12820	0.5
C_2	$32^3 \times 64$	0.158	$8^3 \times 16$	8	7576	0.5
C_5	,,	0.1583	$8^3 \times 16$	8	11200	0.5
$\beta = 5.8$						
<i>tag</i>	<i>lattice</i>	κ	<i>block</i>	N_2	N_{trj}	τ
D_1	$32^3 \times 64$	0.1543	$8^3 \times 16$	8	9600	0.5
D_3	,,	0.15462	$8^3 \times 16$	24	7776	0.5

Table 4.1: Lattice parameters and simulation statistics. Here *block*, N_2 , N_{trj} and τ refer to HMC block, step number for the force F_2 , number of HMC trajectories and the Molecular Dynamics trajectory length respectively.

The simulation details discussed in this section are based on the Ref. [15]. We have generated ensembles of gauge configurations by means of DDHMC algorithm [62–64] using unimproved Wilson fermion and gauge actions with $n_f = 2$ mass degenerate quark flavours. At $\beta = 5.6$ the lattice volumes are $16^3 \times 32$, $24^3 \times 48$ and $32^3 \times 64$ and the renormalized quark mass ranges between 25 to 125 MeV ($\overline{\text{MS}}$ scheme at 2 GeV). At $\beta = 5.8$ the lattice volume is $32^3 \times 64$ and the renormalized physical quark mass ranges

from 15 to 75 MeV. The lattice spacings are determined using nucleon mass to pion mass ratio and Sommer method. These determinations agree for the value of Sommer parameter $r_0 = 0.44$ fm. The lattice spacings at $\beta = 5.6$ and 5.8 are 0.069 and 0.053 fm respectively. The number of thermalized configurations ranges from 7000 to 14000 and the number of measured configurations ranges from 200 to 500. Parameters for a subset of our runs that are used in this paper are given in Table 4.1. For $q(x)$, we use the lattice approximation developed for $SU(2)$ by DeGrand, Hasenfratz and Kovacs [77], modified for $SU(3)$ by Hasenfratz and Neiter [78] and implemented in the MILC code [79]. It uses ten link paths described by unit lattice vector displacements in the sequence $\{x, y, z, -y, -x, t, x, -t, -x, -z\}$ and $\{x, y, z, -x, t, -z, x, -t, -x, -y\}$ plus rotations and cyclic permutations. Lattice gauge fields generated by numerical algorithms are very rough in general and are far from the smooth gauge fields in the continuum. The situation can be improved using the technique namely smearing of gauge links. We used HYP smearing with optimized smearing coefficients $\alpha = 0.75$, $\alpha_2 = 0.6$ and $\alpha_3 = 0.3$ [80]. Unless otherwise stated we have used 3 smearing steps in all our calculations.

One should keep in mind that a fixed HYP smearing level at different lattice spacings does not correspond to a common energy scale (see subsec. 4.1 in Ref. [81]). This is to be contrasted with Wilson flow (see chapter 6) case, which facilitates the use of a common energy scale (Ref. [13]) to study TCDC [81].

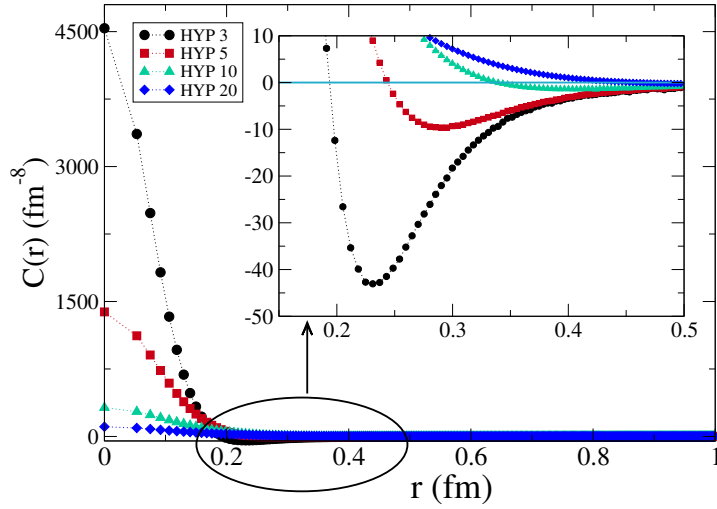


Figure 4.1: Effect of smearing on $C(r)$ at $\beta = 5.8$, $\kappa = 0.15462$ and lattice volume $32^3 \times 64$.

4.6 Results

4.6.1 Effect of smearing

In order to extract the topological charge density reliably on the lattice, using the algebraic definition, smearing of link field is essential. Smearing however smoothens out short distance singularities. Excessive smearing may in fact wipe out the fine details of the singularity structure. Both the positive and negative contributions to χ are affected in this manner. This is illustrated in Fig. 4.1 where we show the effect of 3, 5, 10 and 20 HYP smearing steps on $C(r)$ at $\beta = 5.8$, $\kappa = 0.15462$ and lattice volume $32^3 \times 64$. However the susceptibility is remarkably stable under smearing after three smearing steps as illustrated in Fig. 4.2 (taken from Ref. [36]).

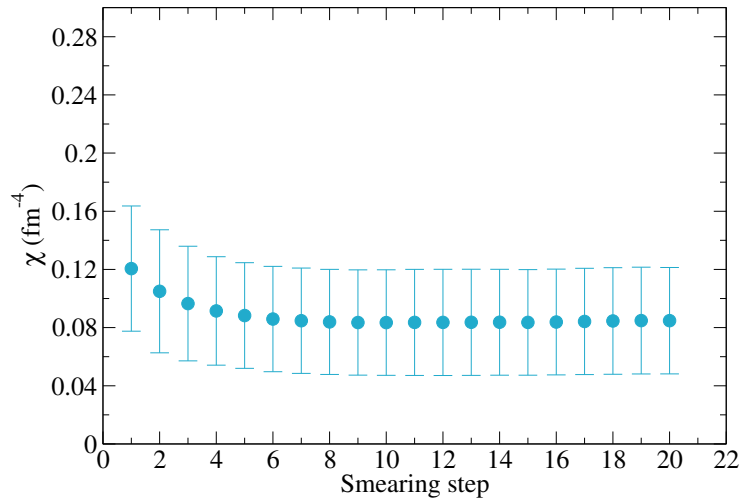


Figure 4.2: Effect of smearing on the χ at $\beta = 5.8$, $\kappa = 0.15462$ and lattice volume $32^3 \times 64$ (taken from Ref. [36]).

4.6.2 Volume dependence

The leading order chiral perturbation theory dictates [16]

$$\langle Q^2 \rangle = V \Sigma m \quad (4.12)$$

where Σ is the chiral condensate and m is the quark mass. If $V \Sigma m \ll 1$, non-trivial topologies are suppressed [16] leading to the suppression of χ at finite volume. In Fig. 4.3 we present the finite volume dependence of the $C(r)$ at $\beta = 5.6$ and $\kappa = 0.158$ at lattice volumes $16^3 \times 32$, $24^3 \times 48$ and $32^3 \times 64$. We find that as volume decreases, the magnitude of the contact term and radius of the positive core decrease and the magnitude of the negative peak increases resulting in the suppression of topological susceptibility at finite volume as volume decreases.

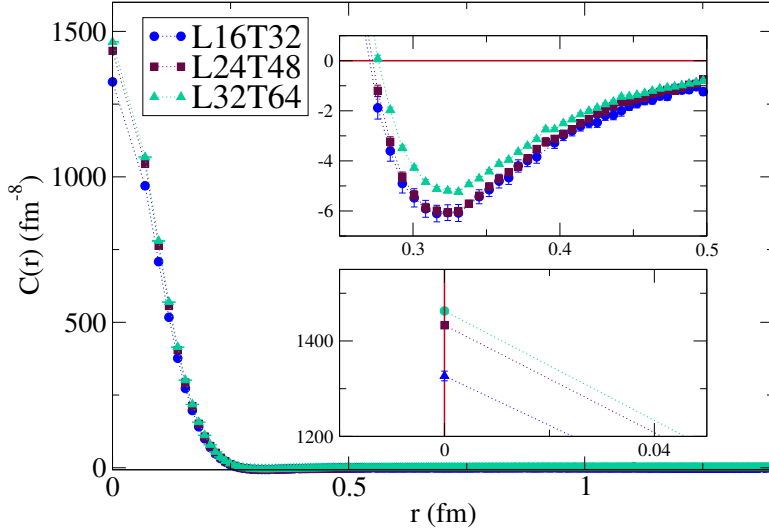


Figure 4.3: Finite volume dependence of the $C(r)$ at $\beta = 5.6$, $\kappa = 0.158$ and lattice volumes $16^3 \times 32$, $24^3 \times 48$ and $32^3 \times 64$.

4.6.3 Dependence on quark mass

In order to understand the detailed mechanism behind the suppression of topological susceptibility with decreasing quark mass, we need to investigate the quark mass dependence of the various features of the $C(r)$. In Fig. 4.4 we present the quark mass dependence of $C(r)$ with emphasis on the positive region at $\beta = 5.6$ and lattice volume $24^3 \times 48$. The magnitude of the contact term $C(0)$ is seen to decrease with decreasing quark mass.

In Fig. 4.5 we present the quark mass dependence of $C(r)$ with emphasis on the crossover from positive to the negative region of $C(r)$ and the negative peak region at $\beta = 5.6$ and lattice volume $24^3 \times 48$. The radius of the positive core and the magnitude of the negative peak of $C(r)$ are seen to decrease and increase respectively with decreasing quark mass.

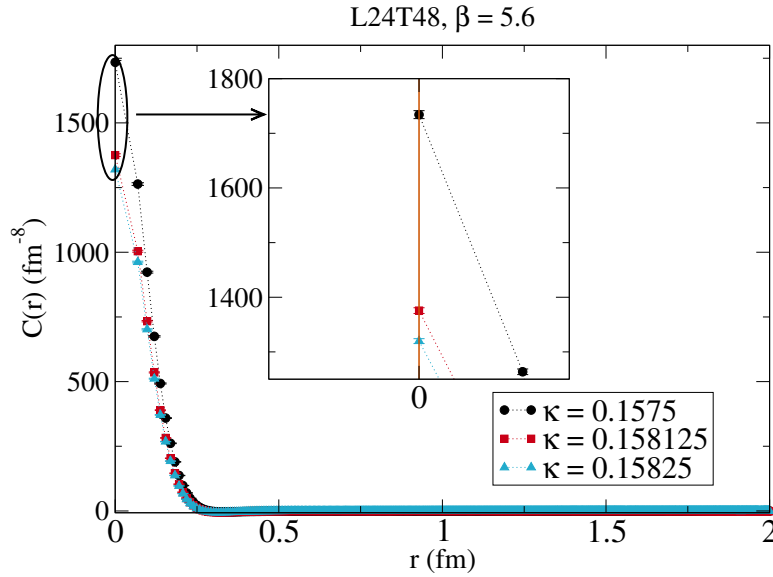


Figure 4.4: The quark mass dependence of $C(r)$ with emphasis on the positive region at $\beta = 5.6$ and lattice volume $24^3 \times 48$.

The features presented in Figs. 4.4 and 4.5 result in the suppression of the topological susceptibility with decreasing quark mass. MILC collaboration [82] has made a similar observation regarding the dependence of the negative peak on quark mass. In Fig. 4.6 we present the corresponding topological susceptibilities ($\beta = 5.6$, lattice volume $24^3 \times 48$ and smearing step 20) as a function of the quark mass which clearly shows the suppression as quark mass decreases. This figure includes $\kappa = 0.158$ in addition to the κ 's presented in Figs. 4.4 and 4.5.

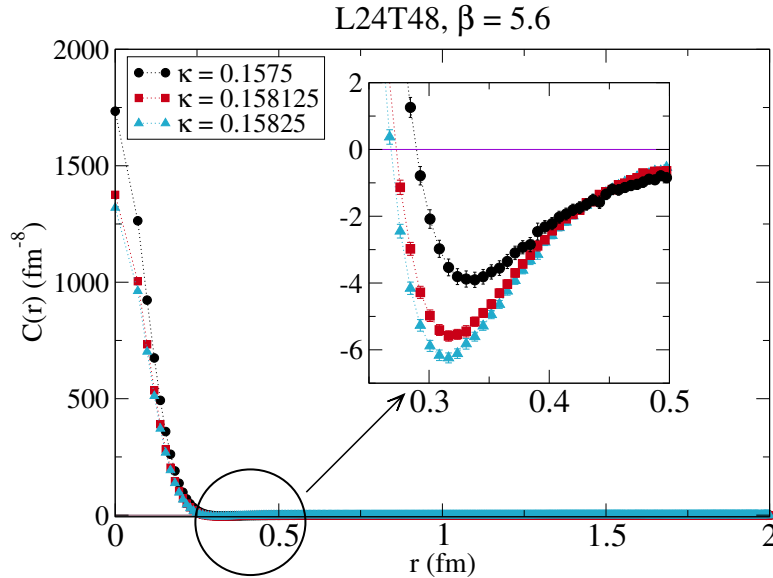


Figure 4.5: The quark mass dependence of $C(r)$ with emphasis on the crossover from positive to the negative region of $C(r)$ and the negative peak region at $\beta = 5.6$ and lattice volume $24^3 \times 48$.

4.6.4 Non-integrability of divergences and lattice spacing dependence

In Ref. [82], the MILC collaboration has carried out a detailed investigation of TCDC using improved staggered fermions and HYP smearing. In this subsection, our main motivation is to repeat the analysis done by MILC in case unimproved Wilson fermions. The shortcomings of smearing techniques such as HYP smearing compared to Wilson flow which is based on solid mathematical footing have become evident only very recently [83]. Due to lack of statistics and the shortcomings of HYP smearing, we attempt only a qualitative study.

From the definition of the topological susceptibility

$$\chi = \int d^4x C(r) = \int 2\pi^2(r^3)dr C(r),$$

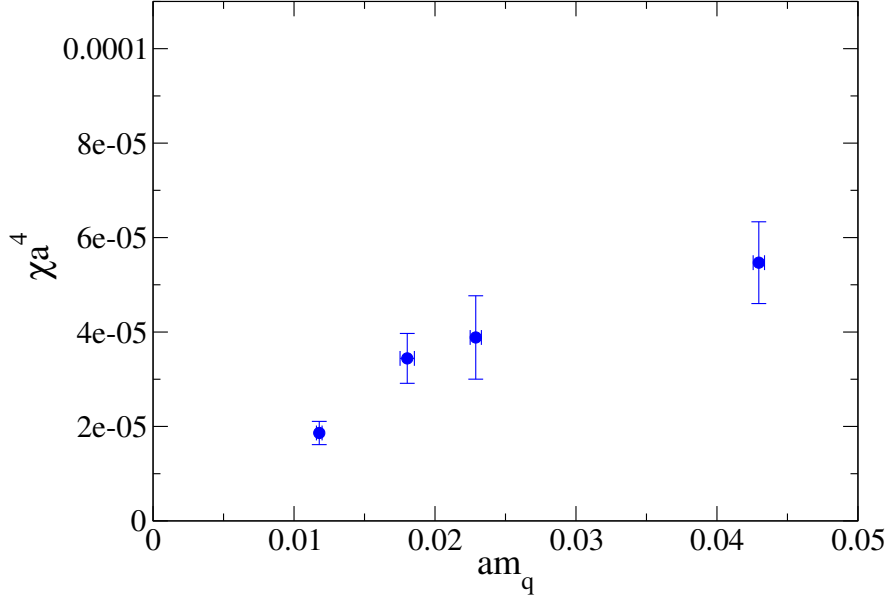


Figure 4.6: Topological susceptibility at $\beta = 5.6$ and lattice volume $24^3 \times 48$ as a function of the quark mass mass.

it is useful to define [82] a *local susceptibility*

$$\chi(r) = \int_0^r 2\pi^2(r'^3)dr' C(r'), \quad (4.13)$$

in order to exhibit the lattice spacing dependence more clearly. It is also useful to define the contributions to the susceptibility from the positive and negative parts of $C(r)$ as [74]

$$\chi_P = \int_0^{r_c} 2\pi^2(r'^3)dr' C(r') \quad (4.14)$$

and

$$\chi_N = \int_{r_c}^{\infty} 2\pi^2(r'^3)dr' C(r') \quad (4.15)$$

respectively.

tag	a (fm)	$\frac{r_c}{a}$	$C(0)$ (fm ⁻⁸)	$ C^{min} $ (fm ⁻⁸)
C_5	0.069	3.93	1336(3)	5.8(1)
D_3	0.053	3.65	4537(7)	43.0(3)

Table 4.2: Lattice spacing dependence of $\frac{r_c}{a}$, $C(0)$ and $|C^{min}|$ at comparable pion mass.

In Table 4.2 we show the lattice spacing dependence of the contact term $C(0)$ and the magnitude of the negative peak of $C(r)$ ($|C^{min}|$) at comparable pion mass in physical units for $\beta = 5.6$ and 5.8 and lattice volume $32^3 \times 64$. For comparison, the corresponding quantities for pure gauge lattice theory at $\beta = 6.0983$ ($a = 0.078\text{fm}$) and lattice volume $24^3 \times 48$ are $C(0) = 285(1)(\text{fm}^{-8})$ and $|C^{min}| = 0.69(5)(\text{fm}^{-8})$. Both the contact term and the negative peak of $C(r)$ increase with decreasing lattice spacing, in accordance with the expectation from the continuum theory.

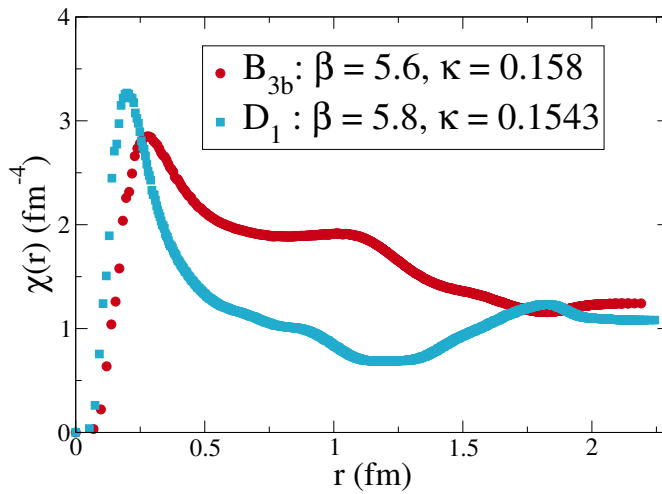


Figure 4.7: The function $\chi(r)$, defined in eq. (4.13) as a function of r at $\beta = 5.6$ and 5.8 at comparable pion masses.

In Fig. 4.7 we plot $\chi(r)$ versus r at two lattice spacings at comparable quark masses. The contribution from the positive part of $C(r)$ results in a peak at short distance. This is followed by a decrease due to the negative part of $C(r)$. As lattice spacing decreases, the contribution from the positive part increases resulting in the increase of the peak of $\chi(r)$.

<i>tag</i>	<i>a</i> (fm)	χ_P (fm ⁻⁴)	χ_N (fm ⁻⁴)	χ (fm ⁻⁴)
B_{3b}	0.069	2.85	-1.61	1.24
D_1	0.053	3.27	-2.19	1.08

Table 4.3: Lattice spacing dependence of χ_P , χ_N and χ at comparable pion mass.

According to the expectations from continuum theory, the negative singularity close to the origin and the positive singularity at the origin are both nonintegrable. Thus the contributions to χ from positive and negative parts of $C(r)$ are expected to diverge, nevertheless resulting in a finite χ due to cancellation. In Table 4.3, we show the contributions to the susceptibility from positive and negative parts of $C(r)$ at $\beta = 5.6$ and 5.8 at comparable pion masses. The data shown in Table 4.3 are in accordance with these expectations.

In Fig. 4.8 (see, however, the discussion in subsec. 4.1 in Ref. [81]), we compare the radius of the positive core of $C(r)$ at $\beta = 5.6$ and 5.8 for comparable pion masses in physical units. The lattice volume is $32^3 \times 64$. The figure clearly exhibits the shrinking of the radius of the positive core of $C(r)$ in physical units as one approaches the continuum.

It is gratifying to note that the various trends regarding lattice spacing dependence shown in Tables 4.2 and 4.3 and Fig. 4.8 have also been observed [74] by using topological charge density operator based on Ginsparg-Wilson fermion [71, 72].

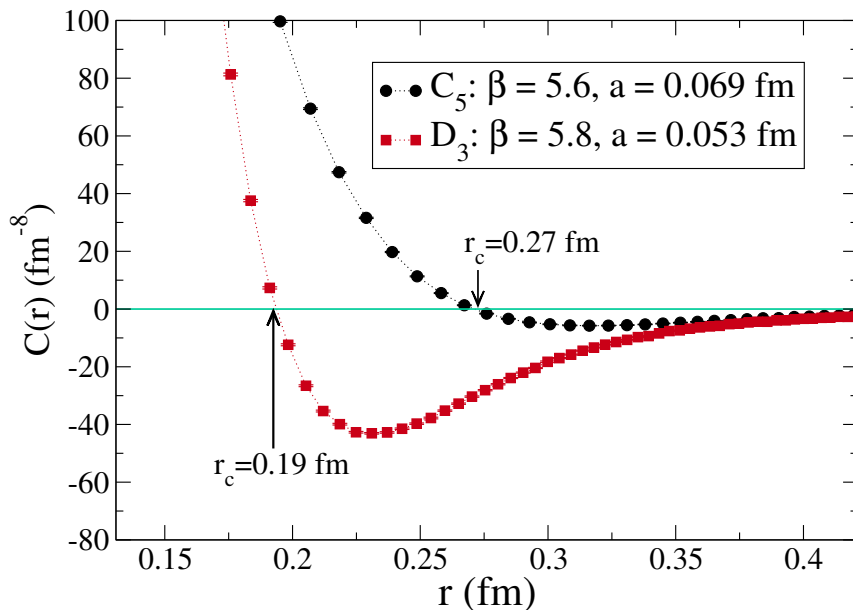


Figure 4.8: Comparison of the radius of the positive core of $C(r)$ at two different lattice spacings for comparable pion mass. Lattice volume is $32^3 \times 64$.

4.7 Discussion and conclusions

It is known that the topological susceptibility decreases with decreasing quark mass and decreasing volume. This has also been demonstrated [9, 36] using Wilson Lattice QCD which has $\mathcal{O}(a)$ lattice artifacts. To understand the mechanisms leading to these suppressions, in this work, we carry out a detailed study of the two-point TCDC. We have shown that, with unimproved Wilson fermions and Wilson gauge action, (1) the two-point TCDC is negative beyond a positive core and radius of the core shrinks as lattice spacing decreases, (2) as volume decreases, the magnitude of the contact term and the radius of the positive core decrease and the magnitude of the negative peak increases resulting in the suppression of topological susceptibility as volume decreases, (3) the contact term and radius of the positive core decrease with decreasing quark mass at a given lattice spacing and the negative peak increases with decreasing quark mass resulting in the suppression of

the topological susceptibility with decreasing quark mass, (4) increasing levels of smearing suppresses the contact term and the negative peak keeping the susceptibility intact and (5) both the contact term and the negative peak diverge in nonintegrable fashion as lattice spacing decreases. Observations similar to 1 and 5 have been made using topological charge density operator based on Ginsparg-Wilson fermion.

CHAPTER 5

Autocorrelations study with Wilson fermions

5.1 Introduction

Reliable estimation of physical quantities in lattice QCD requires that all possible sources of both systematic and statistical error are kept under control. Dynamical Wilson fermion simulations at smaller quark masses, smaller lattice spacings and larger lattice volumes on currently available computers have become feasible with recent developments such as DD-HMC algorithm. However, approach to the continuum and chiral limits may still be hampered by the phenomenon of critical slowing down. One of the manifestation of critical slowing down is the increase in autocorrelation times associated with the measurements of various observables. The autocorrelation times are not universal quantities, they depend upon the discretization of the theory, the algorithms used and the observables. An extensive study of autocorrelation mainly in pure $SU(3)$ gauge theory using DD-HMC algorithm has been carried out by ALPHA collaboration [18]. They have shown that the autocorrelation of squared topological charge increases dramatically with decreasing lattice spacing while Wilson loops decouple from the modes which slow down the topological charge as lattice spacing decreases. In the simulations with dynamical fermions, the study becomes more difficult, because the autocorrelation may now depend on num-

ber of quark flavours (n_f), the quark masses and the fermion action used [29]. In fact ALPHA collaboration [18] has shown, in the case of $n_f = 2$ QCD with Clover action for a given value of quark mass and lattice volume, that squared topological charge decorrelates faster compared with pure gauge at approximately same lattice spacing. These dependencies and the one on the lattice spacing remain to be studied in detail.

In this chapter, we study the autocorrelations of a variety of observables measured with DD-HMC algorithm in the case of unimproved Wilson fermions [1, 2].

5.2 Background

In Markov Chain Monte Carlo simulations, an algorithm is a probabilistic procedure to generate a sequence of field configurations U_i

$$U_1 \rightarrow U_2 \rightarrow U_3 \rightarrow \dots \rightarrow U_N$$

given by transition probability $P(U' \leftarrow U)$. Under certain conditions, in particular stability

$$\pi(U) = \sum_{U'} \pi(U') P(U \leftarrow U'), \quad (5.1)$$

the U_i are then distributed according to a given probability distribution π . Because of this process, the probability distribution of U_{i+1} depends on U_i , which leads to correlations among the subsequent measurements of observables $\mathcal{O}_i = \mathcal{O}(U_i)$. These are described by autocorrelation function

$$C^\mathcal{O}(t) = \langle (\mathcal{O}_i - \langle \mathcal{O} \rangle) (\mathcal{O}_{i+t} - \langle \mathcal{O} \rangle) \rangle \quad (5.2)$$

and integrated autocorrelation time

$$\tau_{\text{int}}^\mathcal{O} = \frac{1}{2} + \sum_{t=1}^{\infty} \frac{C^\mathcal{O}(t)}{C^\mathcal{O}(0)}. \quad (5.3)$$

The error σ^θ for an estimate from N subsequent measurements is then given by

$$\sigma^\theta = \frac{\sqrt{\text{var}(\theta)}}{\sqrt{(N/2\tau_{\text{int}})}}. \quad (5.4)$$

This is the ordinary error formula, which effectively differs from the one without correlation just by the reduction of the number of measurements N by a factor of $2\tau_{\text{int}}$.

5.3 Detail about autocorrelations and error analysis

In this section we follow the discussions and the derivations given in the Refs. [18,84]. Let us assume that $\theta = \{\theta(x)\}_{x \in S}$ be a real-valued function defined on the state space S that is square integrable with respect to π , where π is the stationary Markov chain probability distribution with probability transition matrix P . Now consider that the Markov chain is in equilibrium. Then the unnormalized autocorrelation function,

$$\begin{aligned} C^\theta(t) &= \langle \theta(s)\theta(s+t) \rangle - \mu_\theta^2 \\ &= \sum_{x,y} \theta(x) \left[\pi_x P_{xy}^{(|t|)} - \pi_x \pi_y \right] \theta(y) \end{aligned} \quad (5.5)$$

where $\mu_\theta \equiv \langle \theta(t) \rangle = \sum_x \pi_x \theta(x)$. Now if the algorithm satisfies detailed balance, i.e. $\pi_x P_{xy} = \pi_y P_{yx}$ for all $x, y \in S$ then it is convenient to introduce the symmetric matrix

$$T_{x,y} = \pi_x^{\frac{1}{2}} P_{xy} \pi_y^{-\frac{1}{2}} \quad (5.6)$$

which has real eigenvalues λ_n , $n \geq 0$ with $\lambda_0 = 1$ and $|\lambda_n| < 1$ for $n \geq 1$, assuming an ergodic algorithm. We order the eigenvalues as $|\lambda_n| \leq |\lambda_{n-1}|$. There is a complete set of eigenfunctions $\chi_n(x)$ with $\chi_0(x) = \pi_x^{\frac{1}{2}}$. By using spectral representation of T , eq. (5.5)

can be reduced to

$$C^\theta(t) = \sum_{n \geq 1} (\lambda_n)^t |\eta_n(\theta)|^2 \quad (5.7)$$

where $\eta_n(\theta) = \sum_x \theta(x) \chi_n(x) \pi_x^{\frac{1}{2}}$. Since $|\lambda_n| < 1$ for $n \geq 1$

$$C^\theta(t) = \sum_{n \geq 1} e^{-t/\tau_n} |\eta_n(\theta)|^2 \quad (5.8)$$

where $\tau_n = -\frac{1}{\ln \lambda_n}$, assuming λ_n 's are positive. *Note that the time constants τ_n 's are common to all the observables but different observables couple with different strengths given by $|\eta_n(\theta)|^2$ to these modes.* This results in different τ_{int} 's (eq. 5.10) for different observables.

For any particular observable θ , autocorrelation among the generated configurations are generally determined by the integrated autocorrelation time τ_{int}^θ for that observable. For this purpose, at first, one needs to calculate the unnormalized autocorrelation function of the observable θ measured on a sequence of N equilibrated configurations as

$$\tilde{C}^\theta(t) = \frac{1}{N-t} \sum_{r=1}^{N-t} (\theta_r - \bar{\theta}) (\theta_{r+t} - \bar{\theta}) \quad (5.9)$$

which provides an approximation to the true autocorrelation function given in eq. (5.5) where $\bar{\theta} = \frac{1}{N} \sum_{r=1}^N \theta_r$ is the ensemble average. Following the *windowing* method as recommended by Ref. [84], the integrated autocorrelation time is defined as

$$\tau_{int}^\theta = \frac{1}{2} + \sum_{t=1}^W \Gamma^\theta(t) \quad (5.10)$$

where $\Gamma^\theta(t) = \tilde{C}^\theta(t) / \tilde{C}^\theta(0)$ is the normalized autocorrelation function and W is the summation window. To calculate the errors, we follow the standard techniques available

in the literature [63, 84–87]. The variance of $\Gamma^\theta(t)$ is given by

$$\langle(\delta\Gamma^\theta(t))^2\rangle \approx \frac{1}{N} \sum_{k=1}^{\infty} [\Gamma^\theta(k+t) + \Gamma^\theta(k-t) - 2\Gamma^\theta(t)\Gamma^\theta(k)]^2 \quad (5.11)$$

and the variance of τ_{int}^θ ,

$$\langle(\delta\tau_{int}^\theta)^2\rangle \approx \frac{2(2W+1)}{N} (\tau_{int}^\theta)^2. \quad (5.12)$$

Different strategies have been suggested in the literature [63, 84, 87] for choosing W . We choose W where error of $\Gamma^\theta(t)$ becomes equal to $\Gamma^\theta(t)$ [63]. By using this strategy priority is given to statistical errors over the systematic errors in autocorrelation function and that in turn may result in underestimation of τ_{int} . As stated before, in this work we mainly focus on various trends of autocorrelations that we can observe rather than the precise measurement of τ_{int} . The above expressions are used to calculate the errors unless otherwise stated. In case the total accumulated statistics is extremely large an alternative procedure may be to use binning, with bin sizes much larger than τ_{int} for calculating the error [88].

5.4 Observables

Let us denote plaquette and Wilson loop of size $R \times T$ with smear level s by P_s and $W_s(R, T)$ respectively. Topological susceptibility with smear level s is denoted by Q_s^2 (the normalization factor, inverse of lattice volume, is ignored). We have measured the autocorrelations for the plaquette, Wilson loop, nucleon propagator, pion propagator, topological susceptibility and topological charge density correlator ($C(r) = \langle q(x)q(0) \rangle$) where $q(x)$ is topological charge density and $r = |x|$ for the saved configurations except for the unsmearred plaquette where we have measured for all the configurations, at two values of gauge coupling ($\beta = 5.6$ and 5.8) and several values of the hopping parameter κ . $C(r)$

with smear levels s is denoted by $C_s(r)$. For pion and nucleon we consider the following zero spatial momentum correlation functions

$$C(t) = \sum_{\vec{x}} \langle 0 | \mathcal{O}_1(t, \vec{x}) \mathcal{O}_2(0, \vec{0}) | 0 \rangle \quad (5.13)$$

where t refers to Euclidean time. For the nucleon $\mathcal{O}_1 \mathcal{O}_2 \equiv N \bar{N}$ with $N = (q_d^T C \gamma_5 q_u) q_u$. For the pion $\mathcal{O}_1 \mathcal{O}_2 \equiv P P^\dagger, A A^\dagger, A P^\dagger$ or $P A^\dagger$ where $P = \bar{q}_i \gamma_5 q_j$ (pseudoscalar density) and A corresponds to $A_4 = \bar{q}_i \gamma_4 \gamma_5 q_j$ (fourth component of the axial vector current). Here i and j stand for flavor indices for the u and d quarks and for the charged pion $i \neq j$. For both pion and nucleon we use wall source and point sink. We measure the autocorrelation of the zero spatial momentum correlation functions at an appropriate time slice corresponding to the plateau region of the effective mass. For lattice volume $24^3 \times 48$ and $32^3 \times 64$ we use 12^{th} and 15^{th} time slices respectively. For topological charge density, we use the lattice approximation developed for $SU(2)$ by DeGrand, Hasenfratz and Kovacs [77], modified for $SU(3)$ by Hasenfratz and Nietner [78] and implemented in the MILC code [79]. To suppress the ultraviolet lattice artifacts, smearing of link fields is employed. Unless otherwise stated 20 HYP smear levels with optimized smearing coefficients $\alpha_1 = 0.75$, $\alpha_2 = 0.6$ and $\alpha_3 = 0.3$ [80] are used for the gauge observables. For observables with hadronic operators no gauge field smearing has been used. Our data for topological charge, susceptibility and charge density correlator are presented in [9, 15, 36].

5.5 Measurements detail

We have generated ensembles of gauge configurations by means of DD-HMC [62–64] algorithm using unimproved Wilson fermion and Wilson gauge actions [1, 2] with $n_f = 2$ mass degenerate quark flavors. At $\beta = 5.6$ the lattice volumes are $24^3 \times 48$ and $32^3 \times 64$ and the renormalized physical quark mass (calculated using axial Ward identity) ranges between 25 to 125 MeV ($\overline{\text{MS}}$ scheme at 2 GeV). We used non-perturbative renormaliza-

$\beta = 5.6$							
<i>tag</i>	<i>lattice</i>	κ	<i>block</i>	N_2	N_{cfg}	τ	$r_0 \times m_\pi$
B_{1b}	$24^3 \times 48$	0.1575	$12^2 \times 6^2$	18	13128	0.5	1.7719(38)
B_{3a}	,,	0.158	$6^3 \times 8$	6	7200	0.5	1.2610(59)
B_{3b}	,,	0.158	$12^2 \times 6^2$	18	13646	0.5	1.2542(58)
B_{4a}	,,	0.158125	$6^3 \times 8$	8	9360	0.5	1.1329(57)
B_{4b}	,,	0.158125	$12^2 \times 6^2$	18	11328	0.5	1.0925(58)
B_{5a}	,,	0.15825	$6^3 \times 8$	8	6960	0.5	0.9474(65)
B_{5b}	,,	0.15825	$12^2 \times 6^2$	18	12820	0.5	0.8764(91)
C_1	$32^3 \times 64$	0.15775	$8^3 \times 16$	8	6844	0.5	1.5345(54)
C_2	,,	0.158	$8^3 \times 16$	8	7576	0.5	1.2590(59)
C_3	,,	0.15815	$8^3 \times 16$	8	9556	0.5	1.0697(57)
C_4	,,	0.15825	$8^3 \times 16$	8	4992	0.25	0.9345(64)
C_5	,,	0.1583	$8^3 \times 16$	8	13232	0.25	0.8599(66)
$\beta = 5.8$							
<i>tag</i>	<i>lattice</i>	κ	<i>block</i>	N_2	N_{cfg}	τ	$r_0 \times m_\pi$
D_1	$32^3 \times 64$	0.1543	$8^3 \times 16$	8	9600	0.5	1.3259(76)
D_5	,,	0.15475	$8^3 \times 16$	8	6820	0.25	0.6101(138)

Table 5.1: Lattice parameters, simulation statistics and pion mass (m_π) in the unit of r_0 . Here *block*, N_2 , N_{cfg} , τ refer to DD-HMC block, step number for the force F_2 , number of DD-HMC configurations and the Molecular Dynamics trajectory length respectively.

tion constants (Z_A and Z_P) for unimproved Wilson fermions calculated in [89]. At $\beta = 5.8$ the lattice volume is $32^3 \times 64$ and the renormalized physical quark mass ranges from 15 to 75 MeV. To determine the Sommer parameter (r_0) [90], we plot (figure 9 in Ref. [8]) the ratio of lattice pion mass to lattice nucleon mass versus lattice pion mass in the unit of r_0 . Extrapolation of the ratio to the physical point gives r_0 . Thus the value of r_0 obtained at $\beta = 5.6$ and 5.8 are 0.464 and 0.467 fm respectively. Now using the value of the chiral limit of $\frac{a}{r_0}$ [8], we have computed lattice spacing a . The lattice spacings are 0.072(2) and 0.0568(2) fm at $\beta = 5.6$ and $\beta = 5.8$ respectively. The number of thermalized configurations ranges from 4992 to 13646 with length of the Markov chain ($\tau * N_{cfg}$) 1248 and 6823 respectively. The lattice parameters, simulation statistics and pion mass (m_π) in the unit of r_0 are given in Table 5.1. For all ensembles of configurations the average Metropolis acceptance rates range between 75 – 98%.

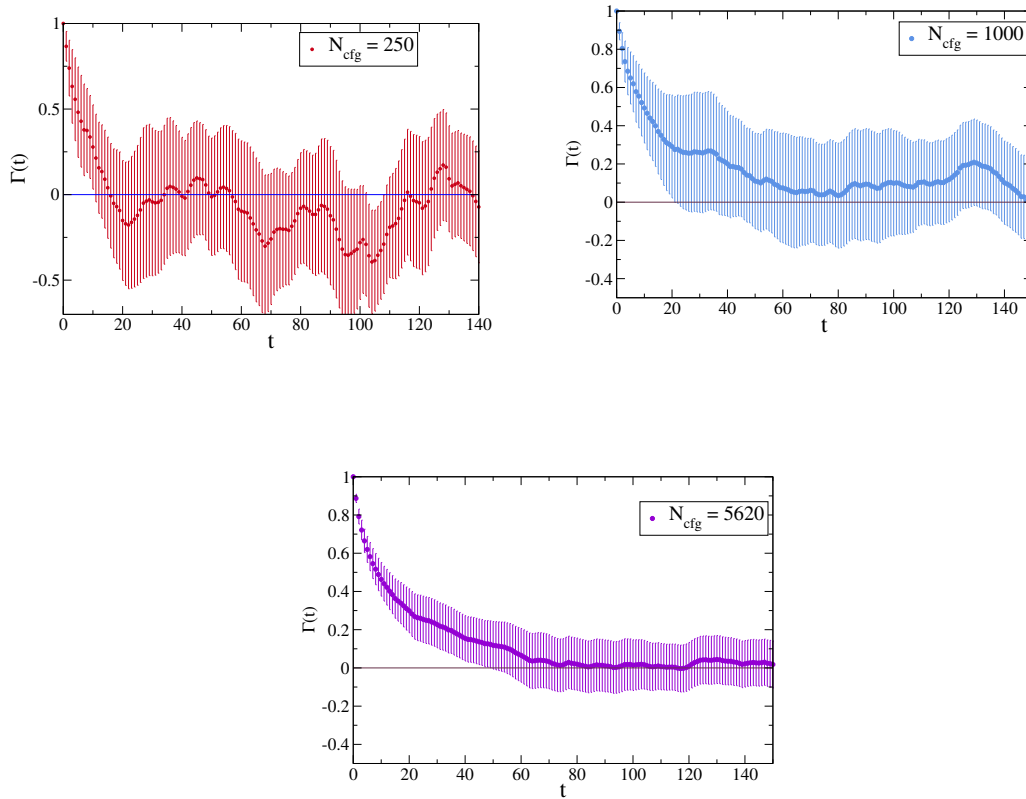


Figure 5.1: Autocorrelation functions for the unsmeared plaquette measured with 250, 1000 and 5620 thermalized configurations respectively at $\beta = 5.6$ for the ensemble B_{5b} .

5.6 Results

5.6.1 Scaling properties with the gaps

Since almost all our runs are with $\tau = 0.5$, the results presented in this thesis are normalized with $\tau = 0.5$. In Fig. 5.1 we show the autocorrelation function for the unsmeared plaquette measured with 250, 1000 and 5620 number of thermalized configurations respectively at $\beta=5.6$, $\kappa = 0.15825$ and lattice volume $24^3 \times 48$. We notice that for smaller statistics, the autocorrelation function touches zero earlier leading to the underestimation of τ_{int} . This happens because of the reduction of central value of autocorrelation function and increase of noise even at smaller t (~ 20) for smaller statistics. Also the positivity of

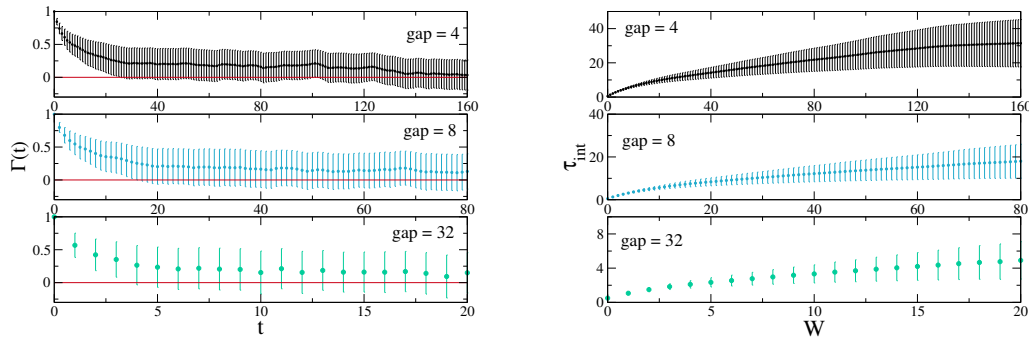


Figure 5.2: Normalized autocorrelation functions (left) and integrated autocorrelation times (right) for unsmeared plaquette with three different gaps (4, 8, 32) between measurements for the ensemble C_5 at $\beta = 5.6$.

the autocorrelation function is violated for $N_{cfg} = 250$ at a few values of t (even though the effect ~ 1 sigma) in contrast to theoretical expectations but the situation improves as statistics increases.

Since it is exorbitant to measure smeared Wilson loops, propagators and smeared topological charge on each and every trajectory, we have measured these observables for the configurations saved with specific gaps. However unsmeared plaquette (P_0) is measured on each trajectory. It is useful to check that the measured autocorrelation scales appropriately with the gaps. The gap of course has to be larger than the autocorrelation length to ensure the correct determination of the autocorrelation. We have carried out such checks and a typical result is presented in Fig. 5.2. Fig. 5.2 shows the normalized autocorrelation functions (left) and integrated autocorrelation times (right) for unsmeared plaquette with three different gaps (4, 8, 32) between measurements for the ensemble C_5 . The data clearly exhibit the scaling properties with the gaps.

5.6.2 Autocorrelations for topological susceptibility (Q_{20}^2)

In Fig. 5.3 we show normalized autocorrelation functions and integrated autocorrelation times for Q_{20}^2 at $\kappa = 0.1543$ and $\kappa = 0.15475$ for $\beta = 5.8$. Windows are chosen as

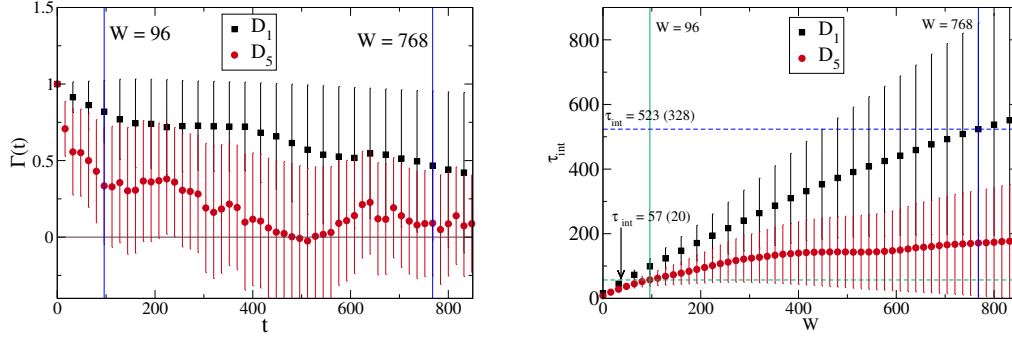


Figure 5.3: Normalized autocorrelation functions (left) and integrated autocorrelation times (right) for Q_{20}^2 at $\beta = 5.8$ for the ensembles D_1 and D_5 .

indicated by the vertical lines. Fig. 5.3 shows that at $\beta = 5.8$ autocorrelations of Q_{20}^2 shows some trend to decrease with decreasing quark mass, even though the deviation is within the error bars. In table 5.2 we present τ_{int} and $R \times \tau_{int}$ where R is the active link ratio (see for example section 3.1 in Ref. [18]) for different κ 's at $\beta = 5.6$ and $\beta = 5.8$. Table 5.2 shows there is also a decreasing trend of autocorrelations of Q_{20}^2 with decreasing quark mass at $\beta = 5.6$, though the effect is more prominent at $\beta = 5.8$. A possible explanation¹ for this suppression of autocorrelation with decreasing quark mass (to be confirmed in future studies with better statistics) is that the algorithm needs to span between lesser number of topological sectors at smaller quark mass since the width of the Gaussian distribution of topological charge decreases with decreasing quark mass.

$\beta = 5.6$		
tag	$\tau_{int}(Q_{20}^2)$	$R \times \tau_{int}(Q_{20}^2)$
B_{3b}	100(28)	36(10)
B_{4b}	86(20)	31(7)
B_{5b}	50(11)	18(4)
$\beta = 5.8$		
tag	$\tau_{int}(Q_{20}^2)$	$R \times \tau_{int}(Q_{20}^2)$
D_1	523(328)	221(138)
D_5	57(20)	24(8)

Table 5.2: τ_{int} and $R \times \tau_{int}$'s for Q_{20}^2 at $\beta = 5.6$ and $\beta = 5.8$.

¹Stefan Schaefer (private communication).

5.6.3 Autocorrelations for $C_3(r)$, Q_3 and Q_3^2

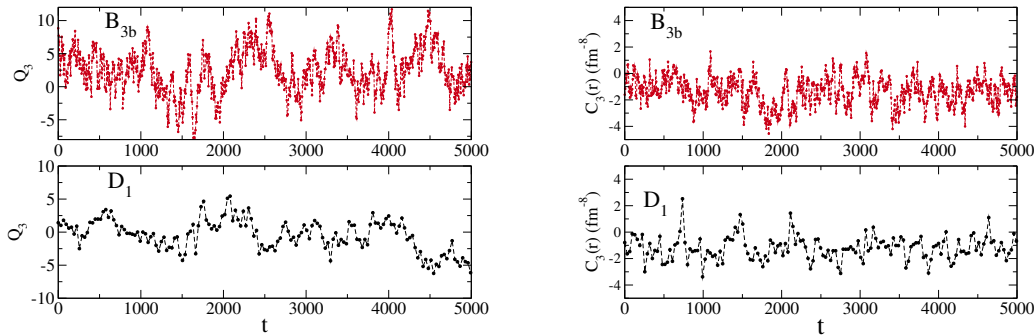


Figure 5.4: Trajectory histories of Q_3 (left) and $C_3(r=r_0)$ (right) for the ensembles B_{3b} and D_1 .

$C(r)$, being a local observable, is very sensitive to short distance fluctuations and in Ref. [15] we have shown that higher levels of smearing drastically change its behaviour with r . We found that smear level 3 is optimum for this observable. In Fig. 5.4 we show the trajectory histories of Q_3 (left) and $C_3(r=r_0)$ (right) for the ensembles B_{3b} and D_1 . Note that pion mass for B_{3b} is comparable with the pion mass for D_1 . Visual inspection indicates that the autocorrelation of Q_3 increases substantially from B_{3b} to D_1 whereas autocorrelation of $C_3(r=r_0)$ shows only mild increase. In Fig. 5.5 we show normalized autocorrelation functions for $C_3(r=r_0)$ and Q_3^2 at $\beta = 5.6$ for the ensemble B_{3b} . Fig. 5.5 shows that at $\beta = 5.6$ the autocorrelations for $C_3(r=r_0)$ and Q_3^2 are very close. The $R \times \tau_{int}$'s for $C_3(r=r_0)$ and Q_3^2 are 26(7) and 36(10) respectively. In Fig. 5.6 we show normalized autocorrelation functions and integrated autocorrelation times for $C_3(r=r_0)$ (left) and Q_3^2 (right) at $\beta = 5.8$ for the ensemble D_1 . Fig. 5.6 shows that at $\beta = 5.8$ the autocorrelation for Q_3^2 is larger than the autocorrelation for $C_3(r=r_0)$. The values of $R \times \tau_{int}$'s for $C_3(r=r_0)$ and Q_3^2 are 32(7) and 300(149) respectively. Figs. 5.5 and 5.6 show that the autocorrelations for Q_3^2 and $C_3(r=r_0)$ increase with decreasing lattice spacing but the effect is milder in latter case.

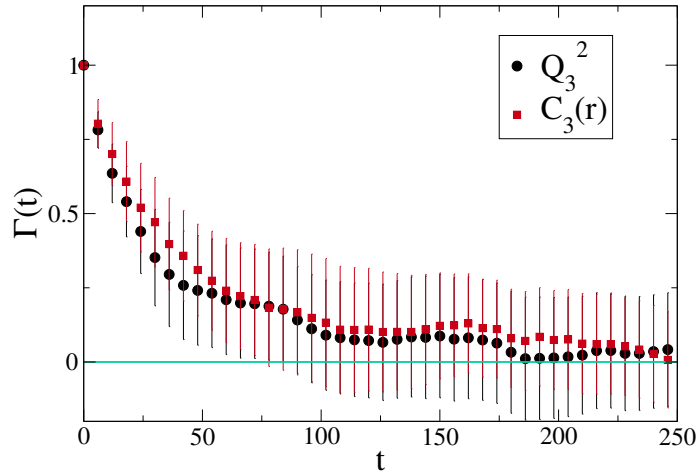


Figure 5.5: Normalized autocorrelation functions for $C_3(r = r_0)$ and Q_3^2 at $\beta = 5.6$ for the ensemble B_{3b} .

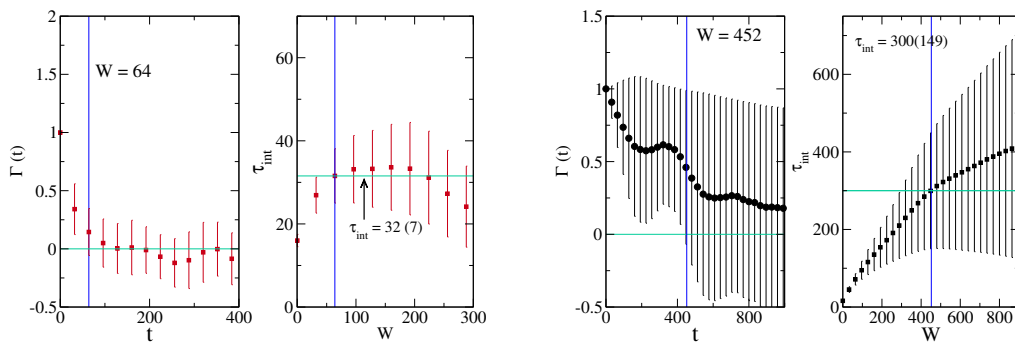


Figure 5.6: Normalized autocorrelation functions and integrated autocorrelation times for $C_3(r = r_0)$ (left) and Q_3^2 (right) at $\beta = 5.8$ for the ensemble D_1 .

5.6.4 Quark mass dependence

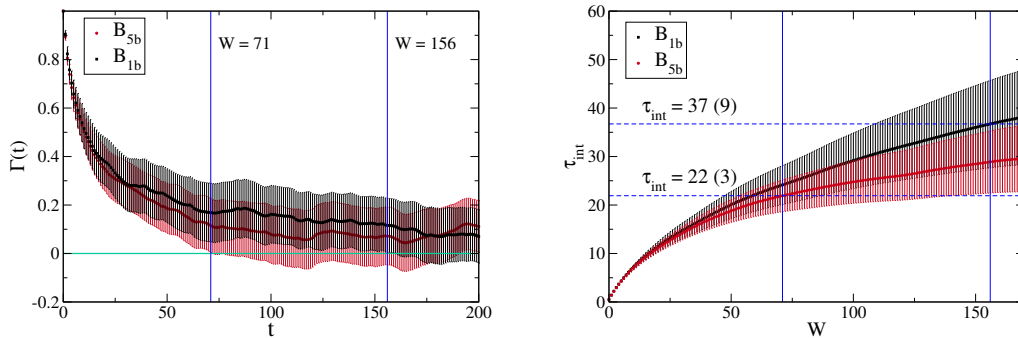


Figure 5.7: Normalized autocorrelation functions (left) and integrated autocorrelation times (right) for P_0 at $\beta = 5.6$ for the ensembles B_{1b} and B_{5b} .

In Fig. 5.7 we present normalized autocorrelation functions (left) and integrated autocorrelation times (right) for P_0 for $\beta = 5.6$ at lattice volume $24^3 \times 48$. From Fig. 5.7, no dependence on quark mass can be deduced for the autocorrelation of P_0 .

In Table 5.3 we present τ_{int} and $R \times \tau_{int}$ for $W_5(4,4)$ for $\beta = 5.6$ at lattice volume $24^3 \times 48$ (tag: B_{1b} and B_{5b}). The autocorrelation of $W_5(4,4)$ does not show any dependence on quark mass.

$\beta = 5.6$			
tag	Wilson loops	τ_{int}	$R \times \tau_{int}$
B_{1b}	$W_5(4,4)$	62(14)	23(5)
B_{5b}	$W_5(4,4)$	62(19)	23(7)

Table 5.3: Dependence of the autocorrelations of Wilson loops on quark mass at $\beta = 5.6$.

5.6.5 Effect of size and smearing

For the measurement of static potential $V(r)$ one needs to measure Wilson loops of various sizes. In the measurement of a Wilson loop, to suppress unwanted fluctuations smearing is needed. Therefore it is interesting to study how autocorrelation of smeared Wilson

$$\beta = 5.6$$

<i>tag</i>	Wilson loops	τ_{int}	$R \times \tau_{int}$
C_2	$W_5(1, 1)$	29(6)	12(3)
C_2	$W_5(4, 4)$	49(12)	21(5)
C_2	$W_5(3, 3)$	44(10)	19(4)
C_2	$W_{20}(3, 3)$	67(20)	28(8)
C_2	$W_{40}(3, 3)$	96(33)	41(14)

Table 5.4: Dependence of the autocorrelations of Wilson loops on size and smear levels at $\beta = 5.6$.

loops changes with sizes of the Wilson loops and smear levels. In Table 5.4 (first two rows) we present τ_{int} and $R \times \tau_{int}$'s for W_5 with different sizes for the ensemble C_2 . In Table 5.4 (third, fourth and fifth rows) we show τ_{int} and $R \times \tau_{int}$'s for $W(3, 3)$ with different levels of HYP smearing for the ensemble C_2 . We observe some increasing trend of autocorrelations of smeared Wilson loops with the increasing size of the Wilson loop and also with the increasing smear level. In the context of Wilson loop and Polyakov loop, SESAM collaboration has observed that geometrically extended observables suffer more from autocorrelation [91] with HMC algorithm.

5.6.6 Autocorrelations for pion and nucleon propagators

$$\beta = 5.6$$

<i>tag</i>	τ_{int}^{Pion}	$R \times \tau_{int}^{Pion}$	$\tau_{int}^{Nucleon}$	$R \times \tau_{int}^{Nucleon}$
B_{3a}	99(19)	27(5)	75(18)	21(5)
B_{4a}	50(9)	14(3)	34(9)	9(3)
B_{5a}	40(10)	11(3)	25(9)	7(3)
C_2	39(13)	17(6)	33(17)	14(7)
C_3	31(15)	13(6)	26(7)	11(3)
C_4	17(6)	7(3)	9(3)	4(1)

Table 5.5: Integrated autocorrelation times for pion (PP) and nucleon propagators with wall sources at $\beta = 5.6$.

For hadronic observables the autocorrelations are quite small and since the number of measurements are not large the errors calculated from Eqs. (5.11) and (5.12) are quite

large and mask the trends of the central values of autocorrelations. Our emphasis is on different trends of autocorrelations. To detect some trend of the central values of the autocorrelations for the hadronic observables we use a rough estimate of errors by single omission jackknife technique. In Table 5.5, τ_{int} and $R \times \tau_{int}$'s for pion (PP) and nucleon propagators with wall sources at a given time slice for $\beta = 5.6$ are presented. Clearly the integrated autocorrelation time decreases with increasing κ (i.e. decreasing quark mass) both for pion and nucleon propagators. Similar observation was made by ALPHA collaboration in the case of Clover fermion [92]. The autocorrelation times of pion and nucleon propagators with point source and sink (not presented here) are smaller than the gap with which configurations are saved.

5.7 Improved estimation of τ_{int}

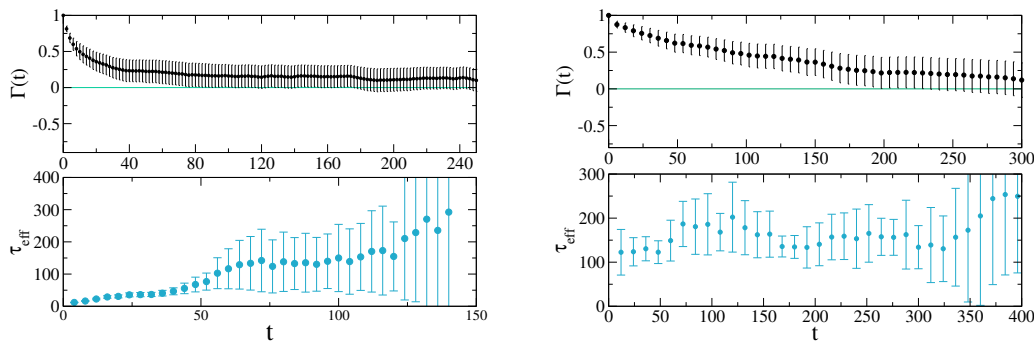


Figure 5.8: Normalized autocorrelation function and effective autocorrelation time for P_0 (left) Q_{20}^2 (right) for the ensemble B_{3b} at $\beta = 5.6$.

We have seen that the autocorrelations of different observables behave differently with the change in lattice spacing. As pointed out in [18], this behaviour is controlled by the coupling of different observables with the slow modes of the transition matrix associated with Monte Carlo Markov chain. In this reference authors have proposed a method to quantify this coupling and estimate τ_{int} more reliably. Following Ref. [18], an improved estimation of τ_{int} can be determined as follows. Let τ^* be the best estimate of the dominant

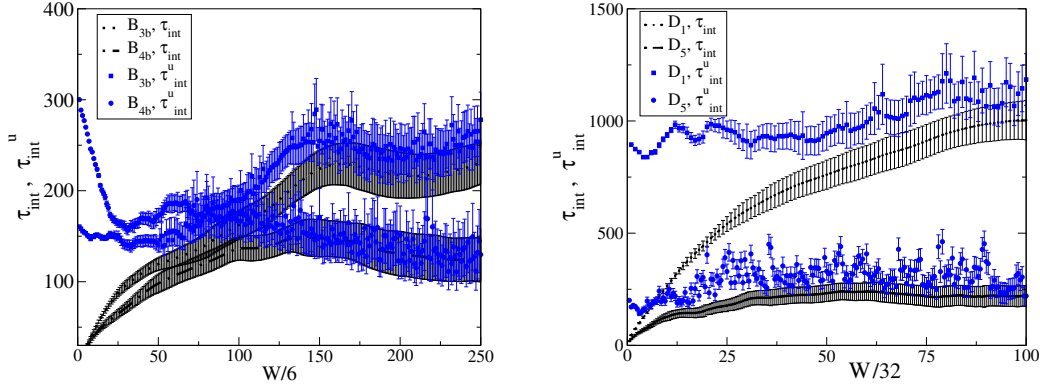


Figure 5.9: Integrated autocorrelation times and their upper bounds (τ_{int}^u) for Q_{20}^2 at $\beta = 5.6$ for the ensembles B_{3b}, B_{4b} (left) and at $\beta = 5.8$ for the ensembles D_1, D_5 (right).

time constant. If for an observable \mathcal{O} all relevant time scales are smaller or of the same order of τ^* then the upper bound of τ_{int}

$$\tau_{int}^u = \frac{1}{2} + \sum_{t=1}^{W_u} \Gamma^{\mathcal{O}}(t) + A_{\mathcal{O}}(W_u) \tau^* \quad (5.14)$$

where $A_{\mathcal{O}} = \max(\Gamma^{\mathcal{O}}(W_u), 2\delta\Gamma^{\mathcal{O}}(W_u))$. W_u is chosen where the autocorrelation is still significant. One possible estimation of τ^* is by measuring effective autocorrelation time, which is introduced in Ref. [18] as described below. Define effective exponential autocorrelation time

$$\tau_{eff}^{exp}(\mathcal{O}) = \frac{t}{2 \ln \frac{\Gamma^{\mathcal{O}}(t/2)}{\Gamma^{\mathcal{O}}(t)}}. \quad (5.15)$$

τ_{eff}^{exp} which can be an estimate of τ^* is defined as,

$$\tau_{eff}^{exp} = \text{Max}_{\mathcal{O}} \left[\frac{t}{2 \ln \frac{\Gamma^{\mathcal{O}}(t/2)}{\Gamma^{\mathcal{O}}(t)}} \right]. \quad (5.16)$$

The estimation of $\tau_{eff}^{exp}(\mathcal{O})$ requires good signal to noise ratio in the asymptotic region in a case by case basis which in turn requires very long Markov chain and is beyond the scope of the present work.

However it is interesting to look at $\tau_{eff}^{exp}(\mathcal{O})$ where reliable data is available and we present such an example in Fig. 5.8 (to detect some trend of the central values of $\tau_{eff}^{exp}(\mathcal{O})$, we use a rough estimate of errors by single omission jackknife technique). In Fig. 5.8 it appears that Q_{20}^2 is coupling dominantly with slow mode, whereas P_0 is coupling with more than one modes. This is reflected in the behaviour of $\tau_{eff}^{exp}(\mathcal{O})$, which shows a single plateau for Q_{20}^2 , but for P_0 , there is more than one plateau and the data is more noisy. Nevertheless the slowest mode appearing in P_0 is approximately the same as in Q_{20}^2 . Similar behaviour is observed in pure gauge theory in Ref. [18]. However since the strengths with which different observables couple to slow mode are different, τ_{int} varies from observable to observable.

In improved estimation given in eq. (5.14) central value of τ_{int} gets modified. To check if this modification preserves the trend of autocorrelation of Q_{20}^2 with respect to quark mass, in Fig. 5.9 we present the integrated autocorrelation times and their upper bounds (τ_{int}^u) with rough errors estimated by jackknife method for topological susceptibilities (Q_{20}^2) at $\beta = 5.6$ for the ensembles B_{3b} , B_{4b} (left) and at $\beta = 5.8$ for the ensembles D_1 , D_5 (right). At both lattice spacings, we find that both $\tau_{int}(Q_{20}^2)$ and $\tau_{int}^u(Q_{20}^2)$ decrease as quark mass decreases.

5.8 Conclusion

In conclusion, we have carried out an extensive study of autocorrelation of several observables in lattice QCD with two degenerate flavours of unimproved Wilson fermions and Wilson gauge action. We find that (1) at a given lattice spacing, autocorrelations of topological susceptibility, pion and nucleon propagators with wall source show indication of decrease with decreasing quark mass, (2) autocorrelation of topological susceptibility and autocorrelation of topological charge density correlator increase with decreasing lattice spacing but the effect is milder in latter case and (3) increasing the size and the smear level increase the autocorrelation of smeared Wilson loop.

CHAPTER 6

Wilson flow

Introduction

Lattice gauge fields generated by numerical simulations are very rough in general and are far from the smooth gauge fields in the continuum. So, an important ingredient in the extraction of physical observables, namely, the smearing (smoothing) of gauge fields is necessary to suppress unwanted fluctuations due to lattice artifacts. In the past, various techniques have been proposed towards smearing the gauge fields [80, 93, 94]. Recently proposed Wilson flow [12–14] puts the technique of smearing on a solid mathematical footing. Similar flow equation in the context of four dimensional smearing has been introduced previously in the literature [93, 95]. The same idea is referred to in the mathematical literature by the name of gradient flow [96–98]. Here, one has to say that this flow is not only confined in gauge fields but for any other fields, one can perform the flow.

In this chapter, we discuss how one can arrive at the flow equation, its smoothing property and its implementation on lattice gauge fields.

6.1 Gradient flow and smoothing operation

Let us consider free scalar field theory action in Euclidean space

$$S_E[\phi] = \int d^4x \left[\frac{1}{2} \partial_\mu \phi \partial_\mu \phi + \frac{1}{2} m^2 \phi^2 \right]. \quad (6.1)$$

Now taking field variation on field ($\phi \rightarrow \phi + \delta\phi$), we get

$$\begin{aligned} S_E[\phi + \delta\phi] &= \int d^4x \left[\frac{1}{2} \partial_\mu (\phi + \delta\phi) \partial_\mu (\phi + \delta\phi) + \frac{1}{2} m^2 (\phi + \delta\phi)^2 \right] \\ &= \int d^4x \left[\frac{1}{2} \partial_\mu \phi \partial_\mu \phi + \frac{1}{2} m^2 \phi^2 + \partial_\mu (\delta\phi) \partial_\mu \phi + m^2 \phi \delta\phi \right] + O((\delta\phi)^2) \\ &\simeq \int d^4x \left[\frac{1}{2} \partial_\mu \phi \partial_\mu \phi + \frac{1}{2} m^2 \phi^2 + \partial_\mu (\delta\phi) \partial_\mu \phi + m^2 \phi \delta\phi \right]. \end{aligned} \quad (6.2)$$

So, the difference between the actions (from eqs. (6.1) and (6.2)) is

$$\begin{aligned} S_E[\phi + \delta\phi] - S_E[\phi] &= \int d^4x \left[\partial_\mu (\delta\phi) \partial_\mu \phi + m^2 \phi \delta\phi \right] \\ &= \int d^4x (\delta\phi) \left[-\partial_\mu \partial_\mu \phi + m^2 \phi \right]. \end{aligned}$$

Then, we can arrive at the flow equation [96–98]

$$\frac{\partial \xi(x, \tau)}{\partial \tau} = \nabla^2 \xi(x, \tau) - m^2 \xi(x, \tau) \quad (6.3)$$

where $\xi(x, \tau) = \phi(x, \tau)$, τ is the gradient flow time and the boundary condition is $\xi(x, \tau = 0) = \phi(x)$. The eq. (6.3) is called gradient flow equation because right hand side of the equation involves the gradient of the action.

Go to momentum space via Fourier transform

$$\xi(x, \tau) = \frac{1}{(2\pi)^4} \int d^4 p e^{ipx} \xi(p, \tau) . \quad (6.4)$$

Now in momentum space, the eq. (6.3) takes the form

$$\frac{\partial \xi(p, \tau)}{\partial \tau} = -(p^2 + m^2) \xi(p, \tau) . \quad (6.5)$$

Integrating the eq. (6.5) and putting the boundary condition ($\xi(p, \tau = 0) = \phi(p)$), we get the solution

$$\xi(p, \tau) = \phi(p) e^{-(p^2 + m^2)\tau} . \quad (6.6)$$

Now, we can go back from momentum space to position space and the solution (6.6) takes the form

$$\xi(x, \tau) = \int d^4 y K_\tau(x - y) \phi(y) \quad (6.7)$$

where

$$\begin{aligned} K_\tau(z) &= \frac{e^{(-z^2/4\tau)}}{(4\pi\tau)^2} e^{-m^2\tau} \\ &= \int \frac{d^4 p}{(2\pi)^4} e^{ipz} e^{-p^2\tau} e^{-m^2\tau} \end{aligned}$$

and $\lim_{\tau \rightarrow 0} K_\tau(z) = \delta^4(z)$.

From the expression of $K_\tau(z)$ (or from the solution (6.6)), one can understand that the high momentum components are suppressed with increasing the flow time (τ). So, the flow is a smoothing operation. More precisely, the scalar field is averaged over a spherical range in space whose root mean-square radius in four dimensions is equal to $\sqrt{8t}$.

6.2 Wilson flow in continuum QCD

The Wilson flow, also known as Yang-Mills gradient flow, is an analytical tool firstly introduced in the context of LQCD by Martin Lüscher in [12, 13]. Using the word of Martin Lüscher: “flows in field space are an interesting tool that may allow new insights to be gained into the physical mechanisms described by highly non-linear QFT such as QCD”.

The Yang-Mills gradient flow $B_\mu(t, x)$, $t \geq 0$, of SU(3) gauge potentials is given by the flow equation (as discussed in the previous section for scalar theory, similarly, taking the variation of the Yang-Mills action w.r.t. the fields, one can arrive at the flow equation.)

$$\partial_t B_\mu = D_\nu G_{\nu\mu}, \quad (6.8)$$

$$G_{\mu\nu} = \partial_\mu B_\nu - \partial_\nu B_\mu + [B_\mu, B_\nu], \quad D_\mu = \partial_\mu + [B_\mu, \cdot], \quad (6.9)$$

and the initial condition $B_\mu(0, x) = A_\mu(x)$, where $A_\mu(x)$ denotes the fundamental gauge field integrated over in the QCD functional integral. Since the flow equation is of first order in the derivatives with respect to the flow time t , the gauge potentials $B_\mu(t, x)$ are uniquely determined by their initial value at $t = 0$ and are thus well-defined functions of the fundamental gauge field.

The term on the right of the eq. (6.8) is proportional to the gradient of the gauge action along the flow and for this reason the equation describes a trajectory in field space that flows towards the stationary points of the Yang-Mills action. The gradient flow has been studied in perturbation theory: in reference [14] it has been shown that the fields $B_\mu(t, x)$ at time $t > 0$ are renormalized and are connected to the renormalized boundary fields $(A_R)_\mu(x)$ in a universal way that is specified by the renormalization group equation. A

consequence is that gauge invariant quantities built from the fields $B_\mu(t, x)$ as

$$E(x) = \frac{1}{2} \text{tr} (G_{\mu\nu}(x)G_{\mu\nu}(x)) \quad (6.10)$$

do not require renormalization. Here, E is action density observable which is gauge invariant in nature.

The linearized form of the flow equation can be solved analytically (as discussed in the previous section): the solution shows explicitly that the flow is a smoothing operation on the gauge field at the boundary $t = 0$.

6.3 Wilson flow on lattice

The Wilson flow can also be studied non-perturbatively on the lattice. In [13, 29], Martin Lüscher proposed the lattice discretization of the eq. (6.8). For any given lattice gauge field $U(x, \mu)$, the first-order differential equation

$$\partial_t V_t(x, \mu) = -g_0^2 \{ \partial_{x, \mu} S_w(V_t) \} V_t(x, \mu), \quad V_t(x, \mu)|_{t=0} = U(x, \mu), \quad (6.11)$$

defines a trajectory $V_t(x, \mu)$ of fields parameterized by the “flow time” t . In the eq. (6.11), $S_w(V_t)$ denotes the Wilson gauge action of the field V_t at gauge coupling g_0 and $\partial_{x, \mu} S_w(V_t)$ its (Lie algebra valued) variation with respect to the link variable $V_t(x, \mu)$. In particular, lattice gauge fields $V_t(x, \mu)$ reside on the links (x, μ) of the lattice at Wilson flow time t and take values in the gauge group. The link differential operators acting on function $f(V)$ of the gauge field are

$$\partial_{x, \mu} f(V) = T^a \partial_{x, \mu}^a f(V) = \frac{d}{ds} f(e^{sX} V)|_{s=0},$$

where $X(y, \nu) = T^a$ if $(y, \nu) = (x, \mu)$, $X(y, \nu) = 0$ if $(y, \nu) \neq (x, \mu)$, s denotes parameter and T^a are the SU(3) generators. Note that the coupling cancels in the flow eq. (6.11).

The differential equation that describes the flow, eq. (6.11) must be discretized in order to solve it with the numerical methods. We adopt the Runge-Kutta scheme described in [13] in our numerical simulation. Then, we have to calculate an observable \mathcal{O} at flow time t as $\langle \mathcal{O} \rangle_t \equiv \langle \mathcal{O}(V_t) \rangle$.

A gauge invariant observable that can be easily computed on the lattice is the action density observable at space time point x (discretization of eq. (6.10))

$$E = 2 \sum_{p \in P_x} \text{Re tr} \{1 - V_t(p)\} \quad (6.12)$$

where $V_t(p)$ is the plaquette field built out of the fields $V_t(x, \mu)$ and P_x is the set of unoriented plaquettes at space time point x . The renormalized quantity E can be used to define the reference flow time t_0 introduced in [12, 13]

$$t^2 \langle E(x) \rangle|_{t=t_0} = 0.3 \quad (6.13)$$

where t is the Wilson flow time. On lattices with periodic boundary conditions on gauge fields, the expectation value $\langle E(x) \rangle$ is independent of x due to translation invariance. In the case of open boundary conditions (to be discussed later) on gauge fields, translation invariance in time direction is broken and $\langle E(x) \rangle$ consequently depends on x_0 (x_0 is the temporal coordinate of the lattice). Then, the reference flow time t_0 is determined through the implicit equation [30]

$$t^2 \langle \bar{E}(x_0 = T/2) \rangle|_{t=t_0} = 0.3 \quad (6.14)$$

where T is the temporal extent of the lattice and \bar{E} is the time slice average of the action

density given in Ref. [30],

$$\bar{E}(x_0) = \frac{1}{2L^3} \sum_{\vec{x}} \text{tr} (G_{\mu\nu}(x)G_{\mu\nu}(x)) \quad (6.15)$$

where L^3 is the spatial volume of the lattice. Through the eqs. (6.13) and (6.14), the reference flow time provides a reference scale to calculate the physical quantities from lattice data.

6.4 Concluding remarks

As previously remarked, the flow is some sort of smoothing operation, as is evident from eq. (6.7). From eq. (6.11) it is actually possible to see that the flow on the lattice is generated by a sequence of infinitesimal stout link smearing steps [98]. In the eqs. (6.13) and (6.14), the arbitrary choice of 0.3 is justified by the observation that this typically corresponds to a smoothing radius of ~ 0.5 fm. This distance is neither too short (cutoff effects are expected to be small) nor too large, so that finite volume effects should also be well under control, in typical lattice volumes. Here an important thing one has to mention is that the time t_0 serves as a reference scale similar to the Sommer parameter r_0 (for detail discussion see reference [13]). With respect to the latter, t_0 has the advantage that its computation does not require any fits.

CHAPTER 7

Topological susceptibility in lattice Yang-Mills theory with open boundary condition

Introduction

An open problem in numerical simulation of lattice QCD is that the spanning of gauge configurations over different topological sectors becomes more and more difficult as the continuum limit is approached. As a consequence, autocorrelation times of physical quantities grow rapidly making the calculation of expectation values time consuming and it may sometime even invalidate the results of simulation. Open boundary condition on the gauge field in the temporal direction has been recently proposed to overcome this problem [29–31]. Lattice gauge theory with such boundary conditions have no barriers between different topological sectors.

In the context of topology of gauge fields, an interesting quantity to study is the topological susceptibility (χ) in pure Yang-Mills theory which is related to the η' mass ($m_{\eta'}$) by the famous Witten-Veneziano formula [10, 56, 57]. This formula takes its simplest form in the chiral limit:

$$m_{\eta'}^2 = \frac{2N_f}{F_\pi^2} \chi$$

where N_f is the number of flavour and F_π is the pion decay constant. For recent high precision calculations of χ with periodic boundary condition see, for example, Refs. [37, 66, 67]. Ref. [66] uses Ginsparg-Wilson fermion for the topological charge density operator whereas Ref. [67] uses the algebraic definition based on field strength tensor. A proposal to overcome the problem of short distance singularity in the computation of topological susceptibility is given in Refs. [73, 99]. Ref. [37] employs a spectral-projector formula which is designed to be free from singularity and compares the result with that using the algebraic definition. The results using different approaches are in agreement with each other within statistical uncertainties.

In this chapter, we address the question whether an open boundary condition in the temporal direction can yield the expected value of the topological susceptibility in SU(3) Yang-Mills theory. We employ the algebraic definition for the topological charge density used in Ref. [37] and for a meaningful comparison with Ref. [37] Wilson flow is used to smoothen the gauge field. We also perform simulations with periodic boundary conditions. In this chapter, we also discuss that using an open boundary condition is advantageous as it allows one to sample different topological sectors by removing the barrier between them.

7.1 Open boundary conditions

The gauge and quark fields live on four-dimensional space-time manifold with Euclidean metric, time extent T and spatial extent L . Open boundary conditions [29, 30] in time does not wrap around in this direction, i.e. there are no terms in the action which couple the field variables at time $x_0 = 0$ to those at the largest time $x_0 = T - a$, while space is taken to be a three-dimensional torus, i.e. all the fields are required to satisfy periodic boundary conditions in the space directions. In a simulation program for periodic lattices, these boundary conditions can often be implemented simply by setting the time-like link

variables at the largest time to zero. In the continuum theory, they amount to imposing boundary conditions,

$$F_{0k}(x)|_{x_0=0} = F_{0k}(x)|_{x_0=T} = 0, \quad k = 1, 2, 3, \quad (7.1)$$

on the gauge field where $F_{\mu\nu}$ is the field tensor of the fundamental gauge field. Note that these conditions preserve the gauge symmetry and therefore do not constrain the gauge degrees of freedom of the field. With this choice of boundary conditions, the field space becomes connected (see section 2.2 in ref. [30]). The absence of disconnected topological sectors goes along with the fact the topological charge is not quantized. However, when choosing open instead of periodic boundary conditions in the physical time direction, the boundary between the topological sectors disappear, the space of the fields becomes connected and thus one expects to observe only moderately increasing autocorrelation times if the slowdown of the algorithm is indeed mainly caused by the separation of the sectors.

7.2 Simulation details

We have generated gauge configurations (using unimproved Wilson gauge action) in SU(3) lattice gauge theory at different lattice volumes and gauge couplings using the openQCD program [32]. With open boundary conditions, the Wilson gauge action is taken to be [30, 100, 101]

$$S_G = \frac{1}{g_0^2} \sum_p w(p) \text{tr}\{1 - U(p)\} \quad (7.2)$$

where the sum runs over all oriented plaquettes p on the lattice and $U(p)$ denotes the ordered product of the link variables around p . The weight $w(p)$ is equal to 1 except for the spatial plaquettes at time 0 and T, which have weight $\frac{1}{2}$.

Gauge configurations using periodic boundary conditions also have been generated for

Lattice	Volume	β	N_{cnfg}	N_0	τ	$a[\text{fm}]$	t_0/a^2
O_1	$24^3 \times 48$	6.21	3970	12	3	0.0667(5)	6.207(15)
O_2	$32^3 \times 64$	6.42	3028	20	4	0.0500(4)	11.228(31)
O_3	$48^3 \times 96$	6.59	2333	26	5	0.0402(3)	17.630(53)
P_1	$24^3 \times 48$	6.21	3500	12	3	0.0667(5)	6.197(15)
P_2	$32^3 \times 64$	6.42	1958	20	4	0.0500(4)	11.270(38)

Table 7.1: Simulation parameters for the HMC algorithm. N_0 is the number of integration steps, τ is the trajectory length and t_0/a^2 is the dimensionless reference Wilson flow time.

several of the same lattice parameters (necessary changes to implement periodic boundary condition in temporal direction were made in the openQCD package for pure Yang-Mills case). Details of the simulation parameters are summarized in table 7.1. In this table, O and P correspond to open and periodic boundary configurations respectively.

Topological susceptibility is measured over N_{cnfg} number of configurations with two successive ones separated by 32 thus making the total length of simulation time to be $N_{\text{cnfg}} \times 32$. The lattice spacings quoted in table 7.1 are determined using the results from Refs. [102, 103]. To smoothen the gauge configurations, Wilson flow [12–14] is used and the reference flow time t_0 is determined through the implicit eq. (6.15). An alternative to the t_0 scale is the w_0 scale proposed in Ref. [104]. We don't see any significant difference in our results using the two different scales.

7.3 Numerical results

7.3.1 Trajectory history of the topological charge

The open boundary condition has been proposed to make the barrier between different topological sectors absent. To that end we first compare the trajectory history of Q for open versus periodic boundary conditions for a reasonably small lattice spacing. In figure 7.1 we plot the fluctuation of Q versus simulation time at $\beta = 6.59$ ($a = 0.0402$) and lat-

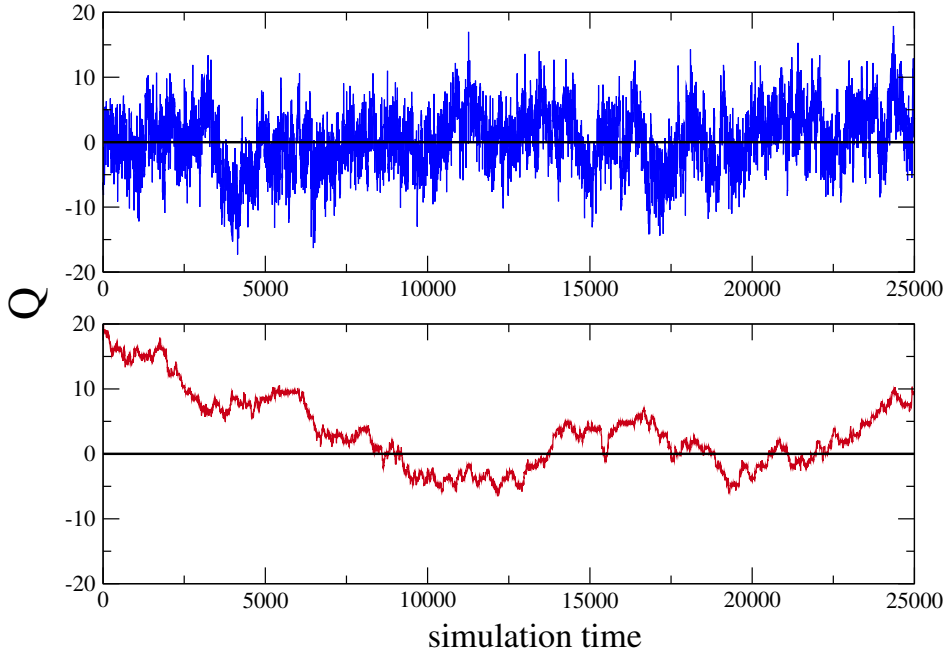


Figure 7.1: Trajectory history of topological charge (Q) versus simulation time at $\beta = 6.59$ and lattice volume $48^3 \times 96$ for open boundary condition (top) and periodic boundary condition (bottom). The data shown is at Wilson flow time $t/a^2 = 2$.

tice volume $48^3 \times 96$ for open boundary condition (top) and periodic boundary condition (bottom) both starting from random configurations. The data shown is at Wilson flow time $t/a^2 = 2$. Unless otherwise stated, all the data presented in the following are at the reference Wilson flow time (t_0). It is evident that with open boundary condition, thermalization is reached very fast whereas with periodic boundary condition it takes a long time just to reach thermalization. It is also evident that after thermalization, autocorrelation length is much larger for the periodic boundary condition compared to the open boundary condition. We have checked that the variation is not so marked for periodic boundary conditions at larger lattice spacings.

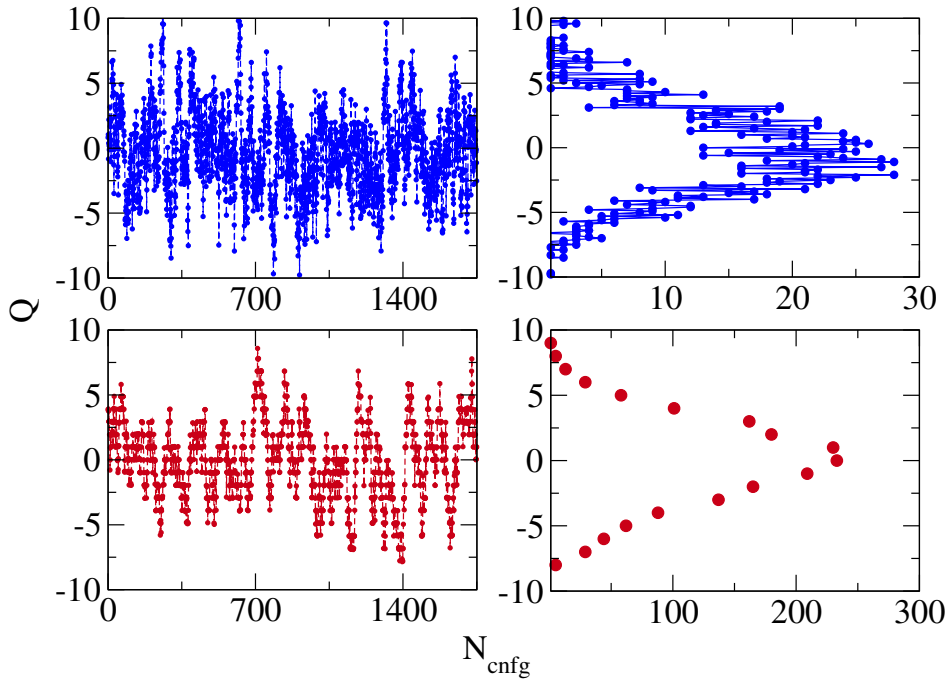


Figure 7.2: Distribution of Q versus N_{cnfg} . Top one (blue) is open boundary condition and bottom (red) is periodic boundary condition at $\beta = 6.42$ and lattice volume is $32^3 \times 64$.

7.3.2 Distribution of Q

Next we look at the distribution of Q . In figure 7.2 along with time histories, we plot the histogram obtained for Q . Top one (blue) is open boundary condition and bottom (red) is periodic boundary condition at $\beta = 6.42$ and lattice volume is $32^3 \times 64$. We note that (1) as expected from the boundary conditions, top (blue) Q is not an integer whereas for bottom (red), it is an integer and (2) even for this coupling ($\beta = 6.42$) which is lower compared to figure 7.1, taking the same number of configurations, the top one gives much better spanning than the bottom. In the plot of histograms in this figure, we have used bin sizes of 0.1 (top) and 1 (bottom).

7.3.3 Distribution of $Q(x_0)$

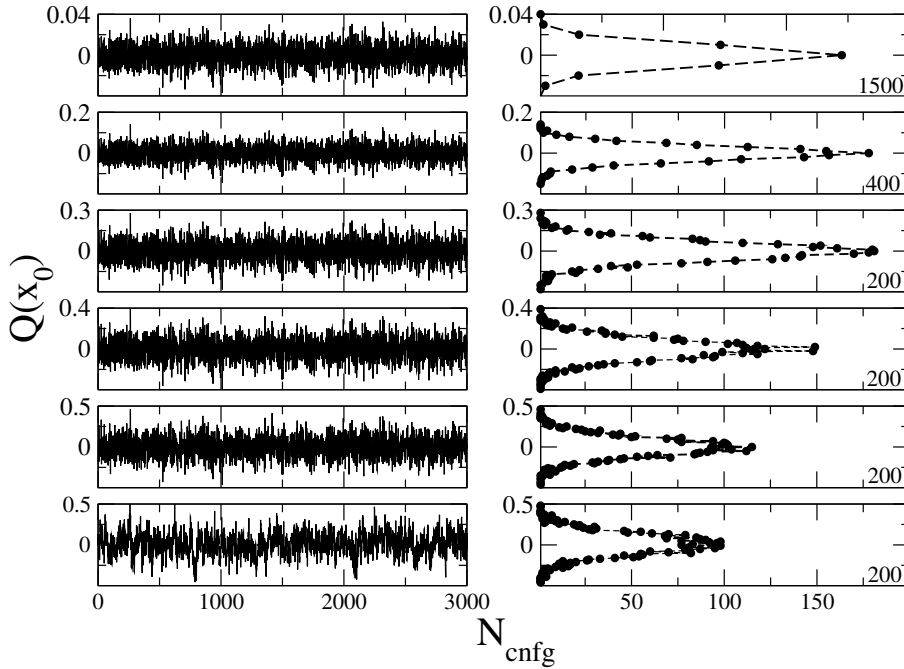


Figure 7.3: Distribution of $Q(x_0)$ versus N_{cnfg} for the ensemble O_2 where $x_0 = 0, 1, 2, 3, 4$ and 24 from top to bottom respectively at $\beta = 6.42$ and lattice volume $32^3 \times 64$.

One needs to investigate the effect of open boundary condition on topological charge density ($q(x)$). We denote $q(x)$ integrated over the spatial volume at fixed Euclidean time x_0 by $Q(x_0)$. The change in the behaviour of $Q(x_0)$ as a function of time slice x_0 reveals the effect of open boundary in the temporal direction. The distribution of $Q(x_0)$ versus N_{cnfg} is presented in figure 7.3 for the ensemble O_2 where $x_0 = 0, 1, 2, 3, 4$ and 24 from top to bottom respectively at $\beta = 6.42$ and lattice volume $32^3 \times 64$. The distribution of $Q(x_0)$ is calculated with bin size of 0.01. As we move from close to the boundary to deeper in the bulk, the spanning of $Q(x_0)$ steadily increases and finally settles down in the bulk region. The same behaviour is also observed at the other end of the temporal lattice.

7.3.4 Subvolume susceptibility

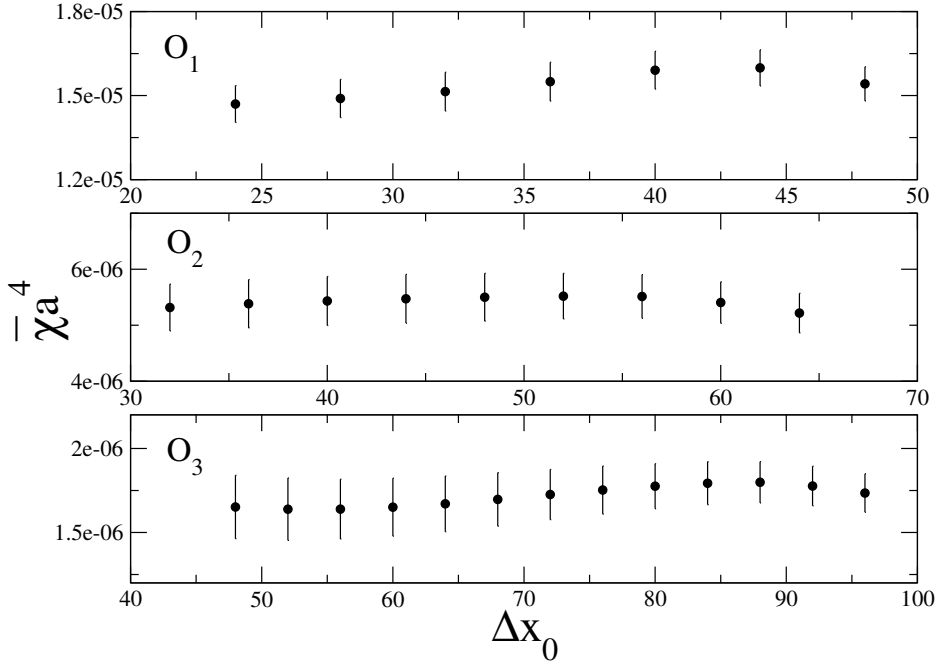


Figure 7.4: Subvolume susceptibility ($\bar{\chi}$) versus temporal length (Δx_0) for the ensembles O_1 , O_2 and O_3 .

For periodic boundary condition, the topological susceptibility is defined as

$$\chi = \frac{\langle Q^2 \rangle}{V} \quad (7.3)$$

where V is the space-time volume. With open boundary condition, due to boundary artifacts, the above eq. (7.3) is no longer valid. To investigate the effect of open boundary on susceptibility we define a subvolume susceptibility [105] as follows:

$$\bar{\chi}(\Delta x_0) = \frac{\langle \tilde{Q}^2 \rangle}{\tilde{V}} \quad (7.4)$$

where \tilde{Q} is the $q(x)$ integrated over the spatial volume and temporal length (Δx_0) which is

taken symmetrically over the mid point of the temporal direction. The subvolume \tilde{V} is the product of spatial volume and Δx_0 . In figure 7.4 we plot $\bar{\chi}$ versus Δx_0 for the ensembles O_1 , O_2 and O_3 . Due to open boundary in the temporal direction, there is slight dip close to the temporal boundary which is consistent with the behaviour of $Q(x_0)$ as shown in figure 7.3. The suppression of the susceptibility for smaller value of Δx_0 is due to finite volume effect. We find that, overall, the effect of the open boundary on the subvolume susceptibility is within the statistical uncertainties.

7.3.5 Stability of the topological susceptibility

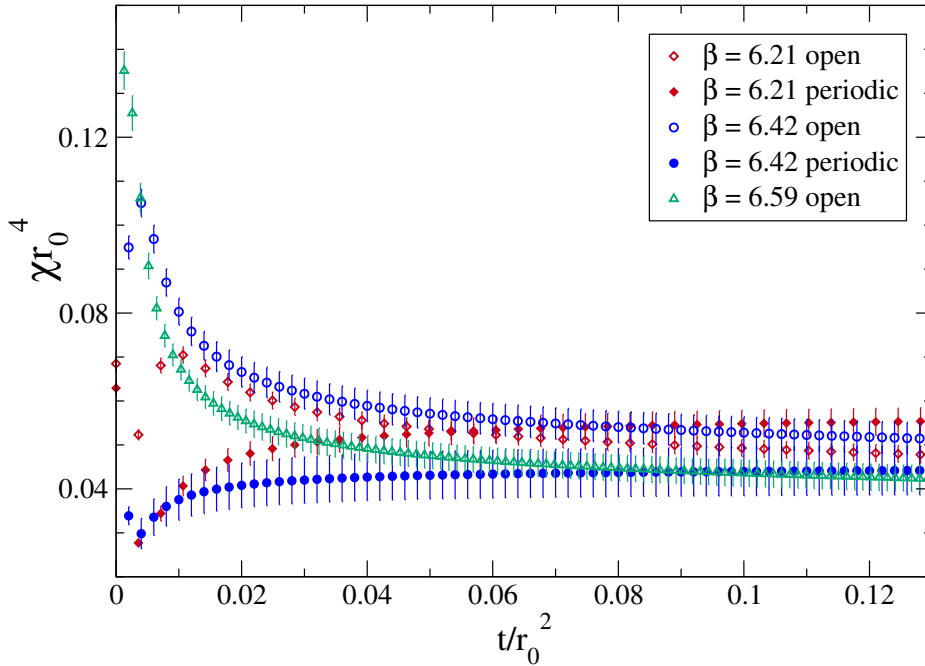


Figure 7.5: Behaviour of topological susceptibility for both open and periodic boundary condition under Wilson flow plotted versus the flow time for different lattice spacings and lattice volumes.

It is interesting to study the stability of χ with respect to Wilson flow time. In figure 7.5, we show the behaviour of χ for both open and periodic boundary condition under Wilson

flow plotted versus the flow time for different lattice spacings and lattice volumes. For very early flow times, χ shows non-monotonous behaviour for both open and periodic boundary condition. For later flow times, χ converges from above to a plateau for open boundary condition whereas it converges from below for the periodic boundary condition.

7.3.6 Extraction of the topological susceptibility and its lattice spacings dependence

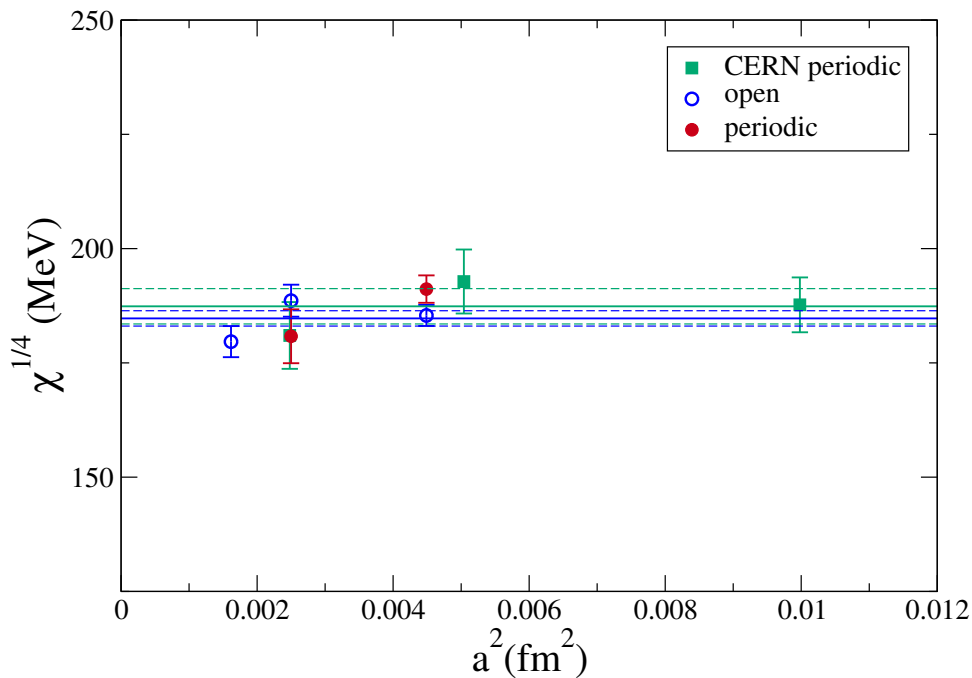


Figure 7.6: $\chi^{1/4}$ in dimensionful unit plotted versus a^2 for both open and periodic boundary condition for different lattice spacings and lattice volumes. For comparison, data from Ref. [37] for periodic boundary condition is also plotted. Also shown are the linear fits to the data Ref. [37] (green lines) and the data for open boundary condition (blue lines).

The values of susceptibility extracted at the reference flow time t_0 are given in table 7.2 and plotted in figure 7.6. In the figure 7.6, we show $\chi^{1/4}$ in dimensionful unit plotted against a^2 for both open and periodic boundary condition for different lattice spacings

Lattice	$a^4\chi/10^{-5}$	$\chi^{1/4}[\text{MeV}]$
O_1	1.5418 (610)	185.4 (2.3)
O_2	0.5217 (354)	188.6 (3.5)
O_3	0.1794 (125)	179.6 (3.4)
P_1	1.7430 (973)	191.1 (3.0)
P_2	0.4407 (554)	180.8 (5.9)

Table 7.2: Topological susceptibility.

and volumes. We find that the results for open and periodic lattices are very close to each other at a given physical volume within our statistical uncertainties which however are not small.

For comparison, data from Ref. [37] for periodic boundary condition is also plotted. Also shown are the linear fits to the data Ref. [37] (green lines) and the data for open boundary condition (blue lines). The extracted value of $\chi^{1/4}$ for the open boundary condition data is 184.7 (1.7) MeV which compares well with the result 187.4 (3.9) MeV of Ref. [37].

7.4 Conclusions

In this study we have shown that the open boundary condition in the temporal direction can yield the expected value of the topological susceptibility in lattice SU(3) Yang-Mills theory. The results agree with numerical simulations employing periodic boundary condition. We have also found that our results support the preferability of the open boundary condition over the periodic boundary condition as the former allows for computation at smaller lattice spacings needed for continuum extrapolation at a lower computational cost. The advantage of open boundary conditions over periodic boundary conditions (see, also, Ref. [106]) are illustrated in figure 7.1.

CHAPTER 8

The scalar glueball mass

8.1 Introduction

In this chapter, we discuss our exploration of open boundary condition in the context of the extraction of lowest scalar glueball mass from the temporal decay of correlators. Extraction of glueball masses compared to hadron masses is much more difficult due to the presence of large vacuum fluctuations present in the correlators of gluonic observables. Moreover the computation of low lying glueball masses which are much higher than the masses of hadronic ground states, in principle requires relatively small lattice spacings. To overcome these problems, anisotropic lattices together with improved actions and operators have been employed [107–109] successfully to obtain accurate glueball masses. On the other hand, the calculation of glueball masses with isotropic lattice has a long history (see for example, the reviews, Refs. [110, 111]). These calculations which employ periodic boundary condition in the temporal direction have been pushed to lattice scale of $a^{-1} = 3.73(6)$ GeV [112, 113]. One would like to continue these calculations to even higher lattice scale which however eventually will face the problem of efficient spanning of the space of gauge configurations. Such trapping has been already demonstrated [33]. It is interesting to investigate whether the open boundary condition can reproduce the

glueball masses extracted with periodic boundary condition at reasonably small lattice spacings achieved so far and whether the former can be extended to even smaller lattice spacings. In this chapter, our main objective is to address all these issues. An important ingredient in the extraction of masses is the smearing of gauge field which is necessary both to suppress unwanted fluctuations due to lattice artifacts and to increase the ground state overlap [114]. In chapter 6, we have already discussed the Wilson flow [12–14] which puts the technique of smearing on a solid mathematical footing. In this chapter, we present the study of the effectiveness of Wilson flow in the extraction of masses.

8.2 Calculation of the lowest scalar glueball mass

The scalar glueball mass is calculated from the correlator

$$C(t = (x_0^{sink} - x_0^{source})) = \langle \bar{E}(x_0^{sink}) \bar{E}(x_0^{source}) \rangle \underset{t \rightarrow \infty}{\sim} e^{-mt} \quad (8.1)$$

where x_0 is the temporal coordinate of the lattice and $\bar{E}(x_0)$ is the average of the action density over spatial volume at a particular time slice, given in eq. (6.15). Now, one can calculate the glueball mass from the plateau region of the effective mass

$$am_{eff}(t) = -\log \frac{C(t)}{C(t-1)} . \quad (8.2)$$

As already mentioned, to extract the scalar glueball mass, in this initial study we have used the correlator of \bar{E} . Since the action is a sum over the plaquettes, this is similar to the use of plaquette-plaquette correlators which have been used in the literature [115, 116]. As in the latter case, there is room for operator improvement. One may use simple four link plaquette (unimproved) or one may use the clover definition of the field strength in the action (improved).

Lattice	Volume	β	N_{cnfg}	N_0	τ	$a[\text{fm}]$	t_0/a^2
O_1	$24^3 \times 48$	6.21	3970	12	3	0.0667(5)	6.207(15)
O_2	$32^3 \times 64$	6.42	3028	20	4	0.0500(4)	11.228(31)
O_3	$48^3 \times 96$	6.59	2333	26	5	0.0402(3)	17.630(53)
O_4	$64^3 \times 128$	6.71	181	64	10	0.0345(4)	24.279(227)
P_1	$24^3 \times 48$	6.21	3500	12	3	0.0667(5)	6.197(15)
P_2	$32^3 \times 64$	6.42	1958	20	4	0.0500(4)	11.270(38)
P_3	$48^3 \times 96$	6.59	295	26	5	0.0402(3)	18.048(152)

Table 8.1: Simulation parameters for the HMC algorithm. N_0 is the number of integration steps, τ is the trajectory length and t_0/a^2 is the dimensionless reference Wilson flow time. O and P refer to ensembles with open and periodic boundary condition in the temporal direction.

8.3 Simulation details

Using the openQCD program [32], SU(3) gauge configurations (using unimproved Wilson gauge action) are generated with open boundary condition (denoted by O) at different lattice volumes and gauge couplings. For comparison purposes, we have also generated gauge configurations (denoted by P) for several of the same lattice parameters by implementing periodic boundary condition in temporal direction in the openQCD package. In table 8.1, we summarize details of the simulation parameters.

Correlator is measured over N_{cnfg} number of configurations. The separation by 32 is made between two successive measurements. Thus the total length of simulation time is $N_{\text{cnfg}} \times 32$. Using the results from Refs. [102, 103], we have determined the lattice spacings which are quoted in table 8.1. We have employed Wilson flow [12–14] to smooth the gauge configurations. The implicit eq. (6.14) defines a reference flow time t_0 which provides a reference scale to extract physical quantities from lattice calculations.

8.4 Numerical results

8.4.1 Effects of boundary conditions on $\langle \bar{E}(x_0) \rangle$

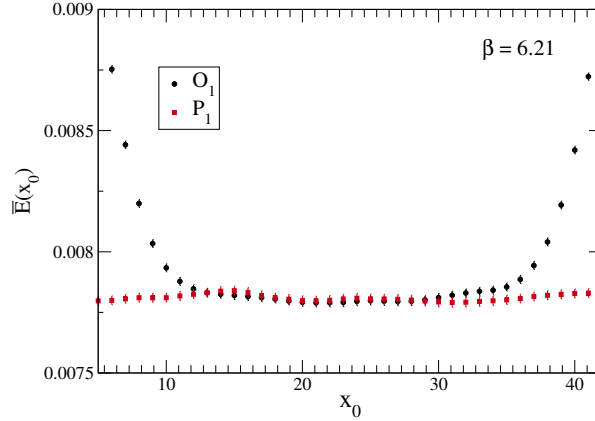


Figure 8.1: Plot of $\langle \bar{E}(x_0) \rangle$ versus x_0 at flow time $t = t_0$ at $\beta = 6.21$ and lattice volume $24^3 \times 48$ for ensemble O_1 (filled circle) and ensemble P_1 (filled square).

Since we extract the scalar glueball mass from the temporal decay of the correlator of $\bar{E}(x_0)$ where x_0 denotes the particular temporal slice, we first look at the effect of open boundary on the $\langle \bar{E}(x_0) \rangle$. In figure 8.1 we plot $\langle \bar{E}(x_0) \rangle$ versus x_0 at flow time $t = t_0$ at $\beta = 6.21$ and lattice volume $24^3 \times 48$ for ensemble O_1 . Breaking of translational invariance due to open boundary condition in the temporal direction is clearly visible in the plot. To calculate the correlator we need to pick the sink and source points from the region free from boundary artifacts, which can be identified from such plot. To facilitate the identification better, we also plot $\langle \bar{E}(x_0) \rangle$ for periodic boundary condition in the temporal direction for the same lattice volume and lattice spacing (ensemble P_1). Preservation of translation invariance is evident in this case. Clearly, for open boundary condition, source and sink points need to be chosen from the region where $\langle \bar{E}(x_0) \rangle$ is almost flat. We note that for both open and periodic cases the central region $\langle \bar{E}(x_0) \rangle$ is not perfectly flat but exhibits an oscillatory behaviour on a fine scale.

8.4.2 Behaviour of $\langle \bar{E}(x_0) \rangle$

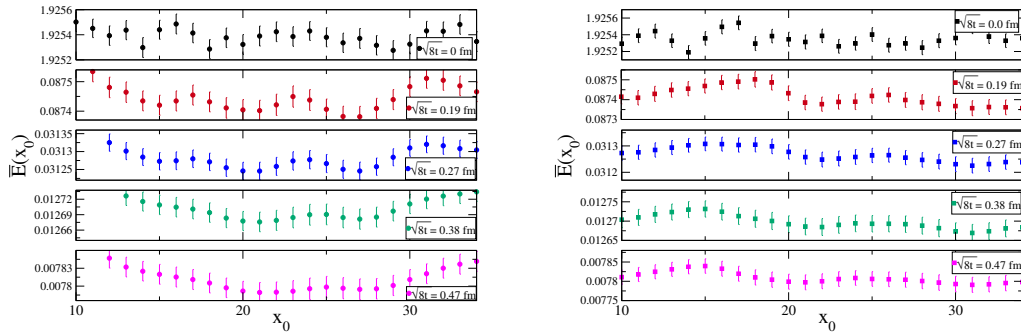


Figure 8.2: Plot of $\langle \bar{E}(x_0) \rangle$ versus x_0 at various flow times t at $\beta = 6.21$ and lattice volume $24^3 \times 48$ for ensemble O_1 (left) and for ensemble P_1 (right).

To understand the oscillatory behaviour, in figure 8.2 we plot $\langle \bar{E}(x_0) \rangle$ versus x_0 at various flow times t at $\beta = 6.21$ and lattice volume $24^3 \times 48$ for ensemble O_1 (left) and for ensemble P_1 (right). At small Wilson flow time, the fluctuations of $\langle \bar{E}(x_0) \rangle$ are very large as seen from the top panel of the plots. To reduce the fluctuation we have to increase Wilson flow time. The comparison of different panels clearly demonstrates the reduction of fluctuations with increasing flow time (note that the scale on y axis becomes finer and finer as flow time increases). However, with increasing flow time the data become more correlated and longer wavelengths appear [31]. The plots show that this smoothing behaviour is the same for both the open and periodic boundary conditions.

8.4.3 Choice of operators

Next we discuss the extraction of glueball mass. As already discussed in section 8.2, one may use the unimproved (naive plaquette) or improved (clover) version of the operator $\bar{E}(x_0)$. In general we expect improved operator to be preferable over unimproved one. However, for the extraction of masses Wilson flow is essential and this may diminish the difference between the results using them. In this work we have used Wilson flow in all

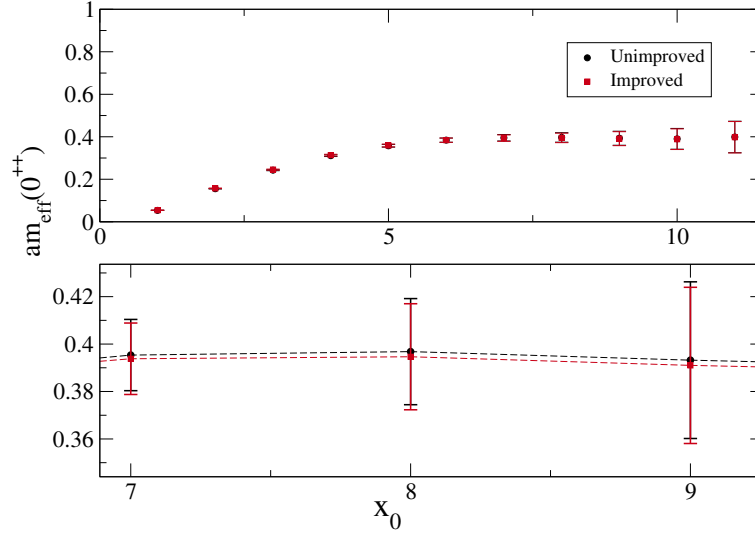


Figure 8.3: Plot of glueball effective mass $am_{eff}(0^{++})$ versus the temporal difference x_0 at Wilson flow times $\sqrt{8t} = 0.28$ fm, $\beta = 6.42$ and lattice volume $32^3 \times 64$ for ensemble P_2 for improved and unimproved choices of operators. The lower panel shows the detail of the plateau region of the upper panel.

the four directions as originally conceived. Due to the smearing in the temporal direction we should expect to get glueball mass for separation between source and sink which are larger than twice the smearing radius ($\approx 2 \times \sqrt{8t}$). However a successful extraction of glueball mass in this case requires reasonably small statistical error at such large temporal separation. In figure 8.3 we plot glueball effective mass $am_{eff}(0^{++})$ versus the temporal difference x_0 ($x_0 = x_0^{\text{source}} - x_0^{\text{sink}}$) at Wilson flow time $\sqrt{8t} = 0.28$ fm, $\beta = 6.42$ and lattice volume $32^3 \times 64$ for ensemble P_2 for improved and unimproved choices of operators (from here onwards, we denote the temporal difference by x_0). As expected the plateau appears for relatively larger temporal separation and presumably thanks to Wilson flow the statistical error is reasonably small. We have verified that the results are very similar at all other Wilson flow times under consideration. Even though we find that there is no noticeable difference between them, we employed the improved operator for the rest of the calculations in this study.

8.4.4 Glueball effective mass using periodic boundary condition with Wilson flow

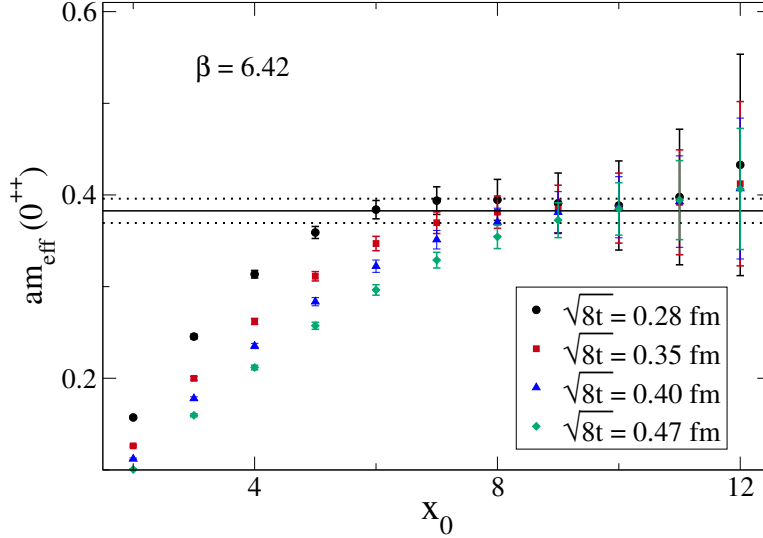


Figure 8.4: Plot of lowest glueball effective mass $am_{eff}(0^{++})$ versus x_0 at four different Wilson flow times t , $\beta = 6.42$ and lattice volume $32^3 \times 64$ for ensemble P_2 . Also shown is the fit to the plateau region of the data for $\sqrt{8t} = 0.35$ fm.

We extract the effective mass for the glueball (0^{++}) state from the temporal decay of the correlator $\langle \bar{E}(x_0^{\text{sink}}) \bar{E}(x_0^{\text{source}}) \rangle$ where x_0^{sink} and x_0^{source} are the sink and source points in the temporal direction. To improve the statistics we have averaged over the source points when we employ periodic boundary condition on the temporal direction. Further to reduce fluctuations we have performed the Wilson flow up to flow time $t = t_0$. In figure 8.4 we plot the lowest glueball effective mass $am_{eff}(0^{++})$ versus x_0 at four Wilson flow times t , $\beta = 6.42$ and lattice volume $32^3 \times 64$ for ensemble P_2 . We find that the effective mass is sensitive to Wilson flow time for initial temporal differences x_0 but becomes independent of different Wilson flow times in the plateau region within statistical error. Note that as expected, the plateau region moves to the right as Wilson flow time increases. Also shown in the figure is the fit to the plateau region of the data for $\sqrt{8t} = 0.35$ fm. The fit

nevertheless passes through the plateau regions of data sets corresponding to other Wilson flow times.

8.4.5 Glueball effective mass using periodic boundary condition with HYP smearing

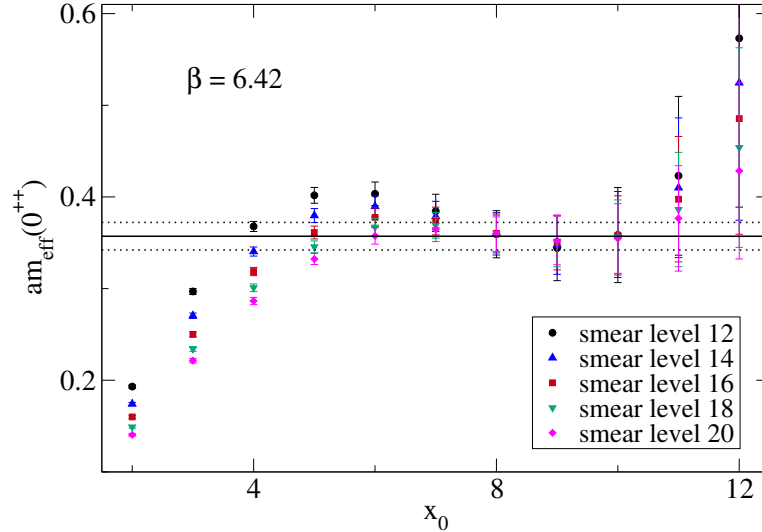


Figure 8.5: Plot of lowest glueball effective mass $am_{\text{eff}}(0^{++})$ versus x_0 at five HYP smearing levels at $\beta = 6.42$ and lattice volume $32^3 \times 64$ for ensemble P_2 . Also shown is the fit to the plateau region of the data for smear level 18.

For comparison with traditional methods to smoothen the gauge field configurations, in figure 8.5 we plot the lowest glueball effective mass $am_{\text{eff}}(0^{++})$ versus x_0 at five smearing levels for four dimensional HYP smearing [80] at $\beta = 6.42$ and lattice volume $32^3 \times 64$ for ensemble P_2 . We find that the effective mass for different smear levels converge in a very narrow window where we can identify the plateau region and extract the mass. This behaviour is to be contrasted with that in the case of Wilson flow discussed in the previous paragraph. The occurrence of a very narrow window in the case of HYP smear is probably due to the fact that the distance between source and sink is not large

enough compared to twice the smearing radius. Also shown in the figure is the fit to the plateau region of the data for smear level 18. In physical units the fitted mass is found to be 1409 (59) MeV which has a marginal overlap with the same [1510 (52) MeV] obtained with Wilson flow. We have observed from our studies with all the β values that the results obtained with HYP smearing are systematically lower than those obtained with Wilson flow. We note that the latter value is closer to the range of glueball mass quoted by other collaborations. The works presented in the rest of study employ Wilson flow to smooth the gauge fields.

8.4.6 Comparison of the lowest glueball mass using open and periodic boundary conditions

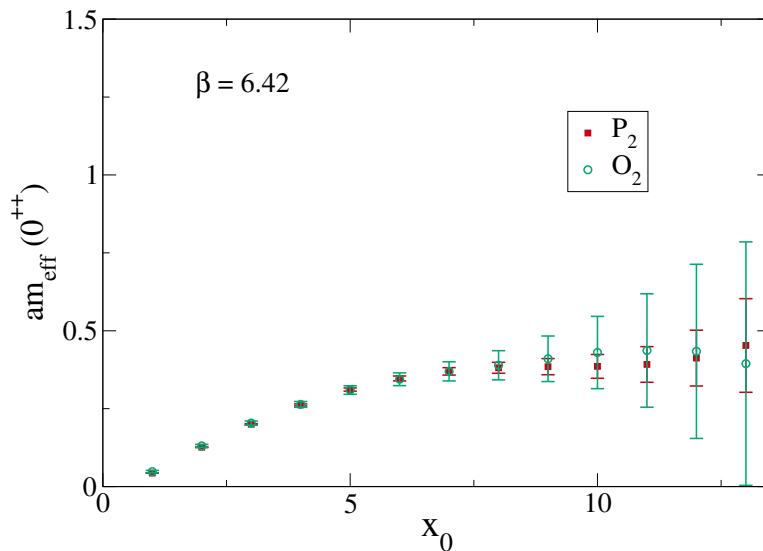


Figure 8.6: Comparison of lowest glueball mass $am_{eff}(0^{++})$ versus x_0 at Wilson flow time ($\sqrt{8t} = 0.35$ fm), $\beta = 6.42$ and lattice volume $32^3 \times 64$ for ensembles O_2 and P_2 .

With open boundary condition the translational invariance in the temporal direction is broken and hence we can not average over all the source points to improve statistical accuracy as we have done in the case of periodic boundary condition. Nevertheless, we

can average over few source points chosen far away from the boundary. In figure 8.6 we plot the lowest glueball effective mass $am_{eff}(0^{++})$ versus x_0 at Wilson flow time ($\sqrt{8t} = 0.35$ fm), $\beta = 6.42$ and lattice volume $32^3 \times 64$ for both open and periodic boundary conditions (ensembles O_2 and P_2). We find that effective mass agree for the two choices of the boundary conditions but as expected statistical error is larger for open boundary data.

8.4.7 Extraction of the lowest glueball mass and its lattice spacings dependence

Lattice	fit range	$am(0^{++})$
O_1	7-9	0.569(69)
P_1	7-9	0.520(21)
O_2	9-12	0.419(57)
P_2	8-11	0.383(13)
O_3	10-12	0.327(39)
P_3	10-12	0.313(28)
O_4	7-10	0.274(48)

Table 8.2: Lattice glueball 0^{++} mass.

In table 8.2 we have shown the fit range used to extract and the extracted lattice glueball mass for the ensembles studied in this paper. A constant is fitted to extract the mass.

To extract the continuum value of 0^{++} glueball mass, in figure 8.7 we plot $m(0^{++})$ in MeV versus a^2 for both open and periodic boundary condition for different lattice spacings and lattice volumes. For the range of reasonably small lattice spacings explored in this work, remarkably, the data does not show any deviation from scaling within the statistical error. Hence we fit a constant to the combined data as shown in the figure and extract the continuum value of 0^{++} mass, 1534(36) MeV. We note that this value compares favorably with the range of glueball mass quoted in the literature.

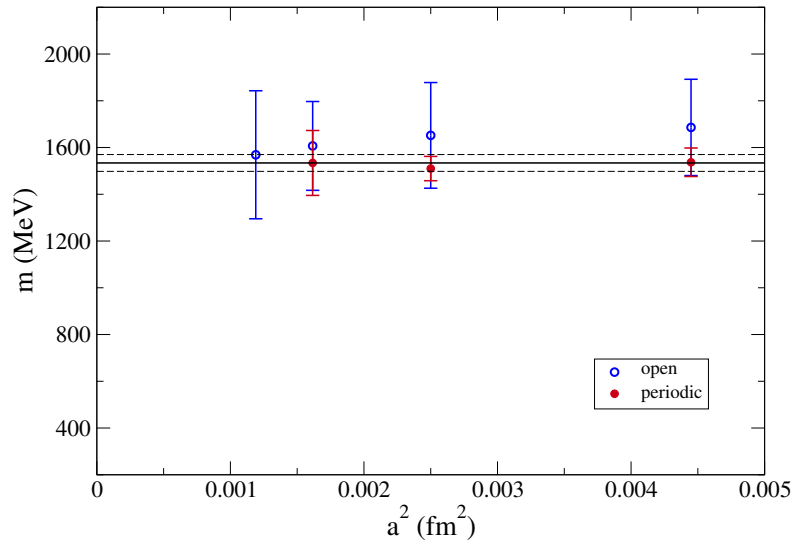


Figure 8.7: Plot of the lowest glueball mass m (0^{++}) in MeV versus a^2 for both open and periodic boundary condition for different lattice spacings and lattice volumes. Also shown is the fit to the combined data.

8.5 Conclusions and discussions

In lattice Yang-Mills theory, we have shown that the open boundary condition on the gauge fields in the temporal direction of the lattice can reproduce the lowest scalar glueball mass extracted with periodic boundary condition at reasonably large lattice scales investigated in the range $3 \text{ GeV} \leq \frac{1}{a} \leq 5 \text{ GeV}$. With open boundary condition we are able to overcome the problem of trapping and performed simulation and extract the glueball mass at even larger lattice scale $\approx 5.7 \text{ GeV}$. Compared to HYP smearing, recently proposed Wilson flow exhibits better systematics as far as the extraction of glueball mass is concerned. The extracted glueball mass shows remarkable insensitivity to the lattice spacings in the range explored in this work $3 \text{ GeV} \leq \frac{1}{a} \leq 5.7 \text{ GeV}$.

The interpolating point like fields perform very poorly as operators which generate hadronic observables that extended spatially [45, 117]. In order to get clear and strong correla-

tion signals, which allow a reliable analysis, we have to optimize the interpolating fields through some smearing techniques. Generally speaking [114] in order to compute masses, it is convenient to consider observables which are functional of the field smeared in space and not in the time in order to preserve eq. (8.1). It has been pointed out [118] that “Only spatial links participate in the averaging. Thus the transfer matrix for the smeared operators remains unaffected and is positive definite.” In our work, however, Wilson flow is carried out in all the four directions and our results show that one can indeed extract mass with relatively small statistical error at relatively large temporal separations. A critical evaluation of the strengths and weaknesses of the four-dimensional versus three-dimensional smoothening of the gauge field in the calculation of masses is beyond the scope of our present study.

CHAPTER 9

Summary

This dissertation is devoted to the study of perturbative and non perturbative aspects of LQCD. In lattice literature, to solve the fermion doubling problem, the so called Wilson term has been introduced which makes first branch physical and all other branches become infinitely massive and decouple from the theory. In perturbation theory it has been shown that the Wilson term reproduces the correct chiral anomaly. The branches other than the first one are rarely explored. In order to explore all branches, we have introduced a generalized Wilson term containing a branch selector index (i_B). We have shown that by choosing i_B one can make the fermions belonging to a particular branch physical. We have also investigated the additive fermion mass shift and chiral anomaly to $O(g^2)$ in lattice perturbation theory for all the branches. We have observed that the additive mass renormalization and the cut-off artifacts in chiral anomaly for non zero quark mass decrease monotonously as one moves from physical branch to central branch. According to the theoretical expectation, we have shown the absence of additive mass renormalization in the central branch and also found the correct value of the chiral anomaly for different branches. Since unimproved Wilson fermions are notorious due to severe additive renormalization, our finding that averaging over suitable branches reduces the cut-off artifacts may be investigated further to explore novel ways of putting fermions on the lattice. Further our findings favour the use of the central branch to study near conformal field theories

with twelve flavours of fermions.

Next we addressed some non-perturbative issues related to the unimproved Wilson fermions in LQCD. To understand the mechanism of decreasing topological susceptibility with quark mass, we have studied the behaviours of the two point Topological Charge Density Correlator (TCDC). The negativity of TCDC also helps one to realize, in a computer simulation, the consequence of reflection positivity which is a property of the Wilson action. We have shed light on these issues and also established many important properties of TCDC which lead to the conclusion that unimproved Wilson fermions is not different from the other class of fermions (such as $\mathcal{O}(a)$ improved Wilson fermions or chiral fermions).

Generated configurations in LQCD through an algorithm are not independent of each other and they are correlated with each other most severely for observables related with topology. For the precise measurement of error associated with an observable, information on its autocorrelation is mandatory. Here, we mention that apart from the ALPHA collaboration (mainly in pure SU(3) gauge theory), no systematic study has been done on autocorrelation so far. We have studied the autocorrelations of a variety of observables measured with DD-HMC algorithm in the case of unimproved Wilson fermions and established its dependencies on quark mass, lattice spacings, smearing level and the size of the observables.

Even though lattice QCD continues to make remarkable progress in confronting experimental data, one of the difficult problems is that the spanning of the gauge configurations over different topological sectors becomes progressively difficult as the continuum limit is approached due to growing autocorrelations. This may sometime even invalidate the results of the simulation. To partially overcome this problem, using open boundary conditions (instead of the usual periodic or anti-periodic ones) in the temporal direction of the lattice has been proposed recently in the literature and to smooth out gauge configurations Martin Luscher has proposed a solid mathematical technique, known as Wilson flow (Gra-

dient flow). To understand the advantages of using open boundary conditions over periodic boundary conditions and the usefulness of the Wilson flow, we have generated gauge configurations (using unimproved Wilson gauge action) in SU(3) lattice gauge theory at different lattice volumes and gauge couplings and to smooth out gauge configurations we have used Wilson flow technique. We have calculated the topological susceptibility and the scalar glueball mass using open and periodic boundary conditions ensembles. We have shown that the open boundary condition on the gauge fields in the temporal direction of the lattice can reproduce the expected value of the topological susceptibility and the lowest scalar glueball mass as with periodic boundary condition at reasonably large lattice scales. With open boundary condition we are able to overcome, to a large extent, the problem of trapping and performed simulation and extracted the topological susceptibility and the glueball mass at even larger lattice scale than what has been achieved so far in the literature. As further avenues of investigation, to extract lowest glueball mass, we have done a comparison study between Wilson flow and HYP (conventional smearing technique). Compared to HYP smearing, Wilson flow exhibits better systematics as far as the extraction of glueball mass is concerned. To summarize, we can conclude that our results support the preferability of the open boundary condition over the periodic boundary condition as the former allows for computation at smaller lattice spacings needed for continuum extrapolation at a lower computational cost.

Bibliography

- [1] K. G. Wilson, *Confinement of Quarks*, Phys.Rev. **D10** (1974) 2445–2459.
- [2] K. G. Wilson, *Quarks and Strings on a Lattice*, New Phenomena in Subnuclear Physics. Part A. Proceedings of the First Half of the 1975 International School of Subnuclear Physics, Erice, Sicily, Jul 11-August 1, 1975, ed. A. Zichichi, Plenum Press, New York, 1977, p. 69, CLNS-321.
- [3] K. Jansen, C. Liu, M. Luscher, H. Simma, S. Sint, et al., *Nonperturbative renormalization of lattice QCD at all scales*, Phys.Lett. **B372** (1996) 275–282, [[hep-lat/9512009](#)].
- [4] R. Edwards, U. M. Heller, and T. Klassen, *The Effectiveness of nonperturbative $O(a)$ improvement in lattice QCD*, Phys.Rev.Lett. **80** (1998) 3448–3451, [[hep-lat/9711052](#)].
- [5] **SESAM T χ L** Collaboration, G. S. Bali et al., *Quark mass effects on the topological susceptibility in QCD*, Phys.Rev. **D64** (2001) 054502, [[hep-lat/0102002](#)].
- [6] B. Orth, T. Lippert, and K. Schilling, *Finite-size effects in lattice QCD with dynamical Wilson fermions*, Phys.Rev. **D72** (2005) 014503, [[hep-lat/0503016](#)].
- [7] A. K. De, A. Harindranath, and S. Mondal, *Chiral Anomaly in Lattice QCD with Twisted Mass Wilson Fermion*, Phys.Lett. **B682** (2009) 150–154, [[arXiv:0910.5611](#)].
- [8] A. Chowdhury, A. K. De, S. De Sarkar, A. Harindranath, J. Maiti, S. Mondal, and A. Sarkar, *Pion and nucleon in two flavour QCD with unimproved Wilson fermions*, Nucl.Phys. **B871** (2013) 82–97, [[arXiv:1212.0717](#)].
- [9] A. Chowdhury, A. K. De, S. De Sarkar, A. Harindranath, S. Mondal, A. Sarkar, and J. Maiti, *Topological susceptibility in Lattice QCD with unimproved Wilson fermions*, Phys.Lett. **B707** (2012) 228–232, [[arXiv:1110.6013](#)].
- [10] E. Seiler, *Some more remarks on the Witten-Veneziano formula for the eta-prime mass*, Phys.Lett. **B525** (2002) 355–359, [[hep-th/0111125](#)].
- [11] E. Seiler and I. Stamatescu, *Some remarks on the Witten-Veneziano formula for the eta-prime mass*, MPI-PAE/PTh 10/87 (1987).

- [12] M. Luscher, *Trivializing maps, the Wilson flow and the HMC algorithm*, Commun.Math.Phys. **293** (2010) 899–919, [[arXiv:0907.5491](#)].
- [13] M. Luscher, *Properties and uses of the Wilson flow in lattice QCD*, JHEP **1008** (2010) 071, [[arXiv:1006.4518](#)].
- [14] M. Luscher and P. Weisz, *Perturbative analysis of the gradient flow in non-abelian gauge theories*, JHEP **1102** (2011) 051, [[arXiv:1101.0963](#)].
- [15] A. Chowdhury, A. K. De, A. Harindranath, J. Maiti, and S. Mondal, *Topological charge density correlator in Lattice QCD with two flavours of unimproved Wilson fermions*, JHEP **1211** (2012) 029, [[arXiv:1208.4235](#)].
- [16] H. Leutwyler and A. V. Smilga, *Spectrum of Dirac operator and role of winding number in QCD*, Phys.Rev. **D46** (1992) 5607–5632.
- [17] S. Durr, *Topological susceptibility in full QCD: Lattice results versus the prediction from the QCD partition function with granularity*, Nucl.Phys. **B611** (2001) 281–310, [[hep-lat/0103011](#)].
- [18] ALPHA Collaboration, S. Schaefer, R. Sommer, and F. Virota, *Critical slowing down and error analysis in lattice QCD simulations*, Nucl.Phys. **B845** (2011) 93–119, [[arXiv:1009.5228](#)].
- [19] A. Chowdhury, A. K. De, S. De Sarkar, A. Harindranath, J. Maiti, S. Mondal, and A. Sarkar, *Exploring autocorrelations in two-flavour Wilson Lattice QCD using DD-HMC algorithm*, Comput.Phys.Commun. **184** (2013) 1439–1445, [[arXiv:1209.3915](#)].
- [20] G. Colangelo, S. Durr, A. Juttner, L. Lellouch, H. Leutwyler, et al., *Review of lattice results concerning low energy particle physics*, Eur.Phys.J. **C71** (2011) 1695, [[arXiv:1011.4408](#)].
- [21] M. Creutz, T. Kimura, and T. Misumi, *Aoki Phases in the Lattice Gross-Neveu Model with Flavored Mass terms*, Phys.Rev. **D83** (2011) 094506, [[arXiv:1101.4239](#)].
- [22] T. Kimura, S. Komatsu, T. Misumi, T. Noumi, S. Torii, et al., *Revisiting symmetries of lattice fermions via spin-flavor representation*, JHEP **1201** (2012) 048, [[arXiv:1111.0402](#)].
- [23] T. Misumi, *New fermion discretizations and their applications*, PoS **LATTICE2012** (2012) 005, [[arXiv:1211.6999](#)].
- [24] L. Del Debbio, *The conformal window on the lattice*, PoS **LATTICE2010** (2010) 004, [[arXiv:1102.4066](#)].
- [25] A. Chowdhury, A. Harindranath, J. Maiti, and S. Mondal, *Many avatars of the Wilson fermion: A perturbative analysis*, JHEP **1302** (2013) 037, [[arXiv:1301.0675](#)].

- [26] S. Aoki, *New Phase Structure for Lattice QCD with Wilson Fermions*, Phys.Rev. **D30** (1984) 2653.
- [27] F. David and H. W. Hamber, *Chiral Condensate With Wilson Fermions*, Nucl.Phys. **B248** (1984) 381.
- [28] R. Frezzotti and G. Rossi, *Chirally improving Wilson fermions. I. $O(a)$ improvement*, JHEP **0408** (2004) 007, [[hep-lat/0306014](#)].
- [29] M. Luscher, *Topology, the Wilson flow and the HMC algorithm*, PoS **LATTICE2010** (2010) 015, [[arXiv:1009.5877](#)].
- [30] M. Luscher and S. Schaefer, *Lattice QCD without topology barriers*, JHEP **1107** (2011) 036, [[arXiv:1105.4749](#)].
- [31] M. Luscher and S. Schaefer, *Lattice QCD with open boundary conditions and twisted-mass reweighting*, Comput.Phys.Commun. **184** (2013) 519–528, [[arXiv:1206.2809](#)].
- [32] <http://luscher.web.cern.ch/luscher/openqcd/index.html>.
- [33] A. Chowdhury, A. Harindranath, J. Maiti, and P. Majumdar, *Topological susceptibility in lattice Yang-Mills theory with open boundary condition*, JHEP **1402** (2014) 045, [[arXiv:1311.6599](#)].
- [34] N. Shibata and C. Hotta, *Boundary effects in the density-matrix renormalization group calculation*, Phys.Rev. **B84** (2011) 115116.
- [35] A. Chowdhury, A. Harindranath, and J. Maiti, *Open Boundary Condition, Wilson Flow and the Scalar Glueball Mass*, JHEP **1406** (2014) 067, [[arXiv:1402.7138](#)].
- [36] A. Chowdhury, A. K. De, S. De Sarkar, A. Harindranath, S. Mondal, A. Sarkar, and J. Maiti, *Spanning of Topological sectors, charge and susceptibility with naive Wilson fermions*, PoS **LATTICE2011** (2011) 099, [[arXiv:1111.1812](#)].
- [37] M. Luscher and F. Palombi, *Universality of the topological susceptibility in the $SU(3)$ gauge theory*, JHEP **1009** (2010) 110, [[arXiv:1008.0732](#)].
- [38] A. M. Polyakov, *Compact Gauge Fields and the Infrared Catastrophe*, Phys.Lett. **B59** (1975) 82–84.
- [39] K. Wilson, *Future directions in particle theory*, Lepton and Photon Interactions At High Energies, Ithaca 1983, 812–834.
- [40] K. G. Wilson, *The Origins of lattice gauge theory*, Nucl.Phys.Proc.Suppl. **140** (2005) 3–19, [[hep-lat/0412043](#)].
- [41] H. Rothe, *Lattice gauge theories: An Introduction*, World Sci.Lect.Notes Phys. **43** (1992) 1–381.

- [42] I. Montvay and G. Munster, *Quantum fields on a lattice*, Cambridge University Press (1994).
- [43] J. Smit, *Introduction to quantum fields on a lattice: A robust mate*, Cambridge Lect.Notes Phys. **15** (2002) 1–271.
- [44] T. DeGrand and C. E. Detar, *Lattice methods for quantum chromodynamics*, World Scientific (2006).
- [45] C. Gattringer and C. B. Lang, *Quantum chromodynamics on the lattice*, Lect.Notes Phys. **788** (2010) 1–343.
- [46] H. B. Nielsen and M. Ninomiya, *No Go Theorem for Regularizing Chiral Fermions*, Phys.Lett. **B105** (1981) 219.
- [47] H. B. Nielsen and M. Ninomiya, *Absence of Neutrinos on a Lattice. 1. Proof by Homotopy Theory*, Nucl.Phys. **B185** (1981) 20.
- [48] H. B. Nielsen and M. Ninomiya, *Absence of Neutrinos on a Lattice. 2. Intuitive Topological Proof*, Nucl.Phys. **B193** (1981) 173.
- [49] L. H. Karsten and J. Smit, *Lattice Fermions: Species Doubling, Chiral Invariance, and the Triangle Anomaly*, Nucl.Phys. **B183** (1981) 103.
- [50] W. Kerler, *Axial Vector Anomaly in Lattice Gauge Theory*, Phys.Rev. **D23** (1981) 2384.
- [51] H. J. Rothe and N. Sadooghi, *A New look at the axial anomaly in lattice QED with Wilson fermions*, Phys.Rev. **D58** (1998) 074502, [[hep-lat/9803026](#)].
- [52] Y. Iwasaki, *Conformal Window and Correlation Functions in Lattice Conformal QCD**, [arXiv:1212.4343](#).
- [53] J. Giedt, *Lattice gauge theory and physics beyond the standard model*, PoS **LATTICE2012** (2012) 006.
- [54] E. T. Neil, *Exploring Models for New Physics on the Lattice*, PoS **LATTICE2011** (2011) 009, [[arXiv:1205.4706](#)].
- [55] A. K. De, A. Harindranath, and S. Mondal, *Effect of r averaging on Chiral Anomaly in Lattice QCD with Wilson Fermion: Finite volume and cutoff effects*, JHEP **1107** (2011) 117, [[arXiv:1105.0762](#)].
- [56] E. Witten, *Current Algebra Theorems for the $U(1)$ Goldstone Boson*, Nucl.Phys. **B156** (1979) 269.
- [57] G. Veneziano, *$U(1)$ Without Instantons*, Nucl.Phys. **B159** (1979) 213–224.
- [58] I. Horvath, S. Dong, T. Draper, F. Lee, K. Liu, et al., *Low dimensional long range topological structure in the QCD vacuum*, Nucl.Phys.Proc.Suppl. **129** (2004) 677–679, [[hep-lat/0308029](#)].

- [59] M. Aguado and E. Seiler, *The Clash of positivities in topological density correlators*, Phys.Rev. **D72** (2005) 094502, [[hep-lat/0503015](#)].
- [60] R. Crewther, *Chirality Selection Rules and the U(1) Problem*, Phys.Lett. **B70** (1977) 349.
- [61] S. Duane, A. Kennedy, B. Pendleton, and D. Roweth, *Hybrid Monte Carlo*, Phys.Lett. **B195** (1987) 216–222.
- [62] M. Luscher, *Solution of the Dirac equation in lattice QCD using a domain decomposition method*, Comput.Phys.Commun. **156** (2004) 209–220, [[hep-lat/0310048](#)].
- [63] M. Luscher, *Schwarz-preconditioned HMC algorithm for two-flavour lattice QCD*, Comput.Phys.Commun. **165** (2005) 199–220, [[hep-lat/0409106](#)].
- [64] <http://luscher.web.cern.ch/luscher/dd-hmc/index.html>.
- [65] M. Grady, *Connecting phase transitions between the 3-d O(4) Heisenberg model and 4-d SU(2) lattice gauge theory*, [arXiv:1104.3331](#).
- [66] L. Del Debbio, L. Giusti, and C. Pica, *Topological susceptibility in the SU(3) gauge theory*, Phys.Rev.Lett. **94** (2005) 032003, [[hep-th/0407052](#)].
- [67] S. Durr, Z. Fodor, C. Hoelbling, and T. Kurth, *Precision study of the SU(3) topological susceptibility in the continuum*, JHEP **0704** (2007) 055, [[hep-lat/0612021](#)].
- [68] R. Feynman, *Space-time approach to nonrelativistic quantum mechanics*, Rev.Mod.Phys. **20** (1948) 367–387.
- [69] H. Sharatchandra, *The Continuum Limit of Lattice Gauge Theories in the Context of Renormalized Perturbation Theory*, Phys.Rev. **D18** (1978) 2042.
- [70] S. Capitani, *Lattice perturbation theory*, Phys.Rept. **382** (2003) 113–302, [[hep-lat/0211036](#)].
- [71] L. Giusti, G. Rossi, and M. Testa, *Topological susceptibility in full QCD with Ginsparg-Wilson fermions*, Phys.Lett. **B587** (2004) 157–166, [[hep-lat/0402027](#)].
- [72] L. Giusti, G. Rossi, M. Testa, and G. Veneziano, *The U(A)(1) problem on the lattice with Ginsparg-Wilson fermions*, Nucl.Phys. **B628** (2002) 234–252, [[hep-lat/0108009](#)].
- [73] M. Luscher, *Topological effects in QCD and the problem of short distance singularities*, Phys.Lett. **B593** (2004) 296–301, [[hep-th/0404034](#)].
- [74] I. Horvath, A. Alexandru, J. Zhang, Y. Chen, S. Dong, et al., *The Negativity of the overlap-based topological charge density correlator in pure-gluon QCD and the non-integrable nature of its contact part*, Phys.Lett. **B617** (2005) 49–59, [[hep-lat/0504005](#)].

- [75] F. Bruckmann, F. Gruber, N. Cundy, A. Schafer, and T. Lippert, *Topology of dynamical lattice configurations including results from dynamical overlap fermions*, Phys.Lett. **B707** (2012) 278–285, [[arXiv:1107.0897](#)].
- [76] K. G. Wilson, *Nonlagrangian models of current algebra*, Phys.Rev. **179** (1969) 1499–1512.
- [77] T. A. DeGrand, A. Hasenfratz, and T. G. Kovacs, *Topological structure in the $SU(2)$ vacuum*, Nucl.Phys.Proc.Suppl. **63** (1998) 528–530, [[hep-lat/9709095](#)].
- [78] A. Hasenfratz and C. Nieter, *Instanton content of the $SU(3)$ vacuum*, Phys.Lett. **B439** (1998) 366–372, [[hep-lat/9806026](#)].
- [79] <http://physics.indiana.edu/sg/milc.html>.
- [80] A. Hasenfratz and F. Knechtli, *Flavor symmetry and the static potential with hypercubic blocking*, Phys.Rev. **D64** (2001) 034504, [[hep-lat/0103029](#)].
- [81] A. Chowdhury, A. Harindranath, and J. Maiti, *Correlation and localization properties of topological charge density and the pseudoscalar glueball mass in lattice Yang-Mills theory*, [arXiv:1409.6459](#).
- [82] MILC Collaboration, A. Bazavov et al., *Topological susceptibility with the asqtad action*, Phys.Rev. **D81** (2010) 114501, [[arXiv:1003.5695](#)].
- [83] ALPHA Collaboration, M. Bruno, S. Schaefer, and R. Sommer, *Topological susceptibility and the sampling of field space in $N_f = 2$ lattice QCD simulations*, JHEP **1408** (2014) 150, [[arXiv:1406.5363](#)].
- [84] N. Madras and A. D. Sokal, *The Pivot algorithm: a highly efficient Monte Carlo method for selfavoiding walk*, J.Statist.Phys. **50** (1988) 109–186.
- [85] T. W. Anderson, *The Statistical Analysis of Time Series*, Wiley-Interscience (1994).
- [86] M. B. Priestley, *Spectral Analysis and Time Series*, Academic Press (1983).
- [87] ALPHA Collaboration, U. Wolff, *Monte Carlo errors with less errors*, Comput.Phys.Commun. **156** (2004) 143–153, [[hep-lat/0306017](#)].
- [88] S. Basak and A. K. De, *Kramers equation algorithm with Kogut-Susskind fermions on lattice*, Phys.Lett. **B430** (1998) 320–325, [[hep-lat/9801001](#)].
- [89] D. Becirevic, B. Blossier, P. Boucaud, V. Gimenez, V. Lubicz, et al., *Non-perturbatively renormalised light quark masses from a lattice simulation with $N(f) = 2$* , Nucl.Phys. **B734** (2006) 138–155, [[hep-lat/0510014](#)].
- [90] R. Sommer, *A New way to set the energy scale in lattice gauge theories and its applications to the static force and alpha-s in $SU(2)$ Yang-Mills theory*, Nucl.Phys. **B411** (1994) 839–854, [[hep-lat/9310022](#)].

- [91] T. Lippert, G. Bali, N. Eicker, L. Giusti, U. Glassner, et al., *SESAM and T-chi-L results for Wilson action: A Status report*, Nucl.Phys.Proc.Suppl. **60A** (1998) 311–334, [[hep-lat/9707004](#)].
- [92] M. Marinkovic, S. Schaefer, R. Sommer, and F. Viotto, *Strange quark mass and Lambda parameter by the ALPHA collaboration*, PoS **LATTICE2011** (2011) 232, [[arXiv:1112.4163](#)].
- [93] **APE** Collaboration, M. Albanese et al., *Glueball Masses and String Tension in Lattice QCD*, Phys.Lett. **B192** (1987) 163–169.
- [94] C. Morningstar and M. J. Peardon, *Analytic smearing of SU(3) link variables in lattice QCD*, Phys.Rev. **D69** (2004) 054501, [[hep-lat/0311018](#)].
- [95] R. Narayanan and H. Neuberger, *Infinite N phase transitions in continuum Wilson loop operators*, JHEP **0603** (2006) 064, [[hep-th/0601210](#)].
- [96] M. F. Atiyah and R. Bott, *The Yang-Mills Equations over Riemann Surfaces*, in *Philosophical Transactions of the Royal Society of London, series A, Mathematical and Physical Sciences* **308** (1983) 523.
- [97] M. Nakahara, *Geometry, Topology and Physics*, Taylor and Francis (2003).
- [98] S. K. Donaldson and P. B. Kronheimer, *The Geometry of Four-Manifolds*, Oxford University Press (1997).
- [99] L. Giusti and M. Luscher, *Chiral symmetry breaking and the Banks-Casher relation in lattice QCD with Wilson quarks*, JHEP **0903** (2009) 013, [[arXiv:0812.3638](#)].
- [100] M. Luscher, R. Narayanan, P. Weisz, and U. Wolff, *The Schrodinger functional: A Renormalizable probe for nonAbelian gauge theories*, Nucl.Phys. **B384** (1992) 168–228, [[hep-lat/9207009](#)].
- [101] S. Sint, *On the Schrodinger functional in QCD*, Nucl.Phys. **B421** (1994) 135–158, [[hep-lat/9312079](#)].
- [102] **ALPHA** Collaboration, M. Guagnelli, R. Sommer, and H. Wittig, *Precision computation of a low-energy reference scale in quenched lattice QCD*, Nucl.Phys. **B535** (1998) 389–402, [[hep-lat/9806005](#)].
- [103] S. Necco and R. Sommer, *The $N(f) = 0$ heavy quark potential from short to intermediate distances*, Nucl.Phys. **B622** (2002) 328–346, [[hep-lat/0108008](#)].
- [104] S. Borsanyi, S. Durr, Z. Fodor, C. Hoelbling, S. D. Katz, et al., *High-precision scale setting in lattice QCD*, JHEP **1209** (2012) 010, [[arXiv:1203.4469](#)].
- [105] P. de Forcrand, M. Garcia Perez, J. Hetrick, E. Laermann, J. Lagae, et al., *Local topological and chiral properties of QCD*, Nucl.Phys.Proc.Suppl. **73** (1999) 578–580, [[hep-lat/9810033](#)].

- [106] G. McGlynn and R. D. Mawhinney, *Diffusion of topological charge in lattice QCD simulations*, Phys.Rev. **D90** (2014) 074502, [[arXiv:1406.4551](#)].
- [107] C. J. Morningstar and M. J. Peardon, *Efficient glueball simulations on anisotropic lattices*, Phys.Rev. **D56** (1997) 4043–4061, [[hep-lat/9704011](#)].
- [108] C. J. Morningstar and M. J. Peardon, *The Glueball spectrum from an anisotropic lattice study*, Phys.Rev. **D60** (1999) 034509, [[hep-lat/9901004](#)].
- [109] Y. Chen, A. Alexandru, S. Dong, T. Draper, I. Horvath, et al., *Glueball spectrum and matrix elements on anisotropic lattices*, Phys.Rev. **D73** (2006) 014516, [[hep-lat/0510074](#)].
- [110] M. J. Teper, *Glueball masses and other physical properties of $SU(N)$ gauge theories in $D = (3+1)$: A Review of lattice results for theorists*, OUTP-98-88-P (Dec, 1998) [[hep-th/9812187](#)].
- [111] G. S. Bali, ‘*Glueballs*’: *Results and perspectives from the lattice*, C01-09-02.1 (2001) 249–262, [[hep-ph/0110254](#)].
- [112] UKQCD Collaboration, G. Bali et al., *A Comprehensive lattice study of $SU(3)$ glueballs*, Phys.Lett. **B309** (1993) 378–384, [[hep-lat/9304012](#)].
- [113] A. Vaccarino and D. Weingarten, *Glueball mass predictions of the valence approximation to lattice QCD*, Phys.Rev. **D60** (1999) 114501, [[hep-lat/9910007](#)].
- [114] G. Parisi, *Prolegomena to any future computer evaluation of the QCD mass spectrum*, LNF-84-4-P, C83-09-01 (1984).
- [115] B. Berg, *Plaquette-plaquette Correlations in the $SU(2)$ Lattice Gauge Theory*, Phys.Lett. **B97** (1980) 401.
- [116] B. Berg and A. Billoire, *Glueball Spectroscopy in Four-dimensional $SU(3)$ Lattice Gauge Theory. 2.*, Nucl.Phys. **B226** (1983) 405.
- [117] T. A. DeGrand and R. D. Loft, *Gaussian shell model trial wave functions for lattice QCD spectroscopy*, .
- [118] R. Gupta, A. Patel, C. F. Baillie, G. W. Kilcup, and S. R. Sharpe, *Exploring glueball wave functions on the lattice*, Phys.Rev. **D43** (1991) 2301–2313.